Acetone Planar Laser-Induced Fluorescence and Phosphorescence for Mixing Studies of Multiphase Flows at High Pressure and Temperature

A Dissertation
Presented to
The Academic Faculty

by

Thao T. Tran

In Partial Fulfillment
of the Requirements for the Degree
Doctor of Philosophy in Aerospace Engineering

Georgia Institute of Technology

August 2008

Acetone Planar Laser-Induced Fluorescence and Phosphorescence for Mixing Studies of Multiphase Flows at High Pressure and Temperature

Approved by:

Prof. Jerry M. Seitzman, Advisor
School of Aerospace Engineering
Georgia Institute of Technology

Dr. Timothy C. Lieuwen
School of Aerospace Engineering
Georgia Institute of Technology

Prof. Jechiel J. Jagoda
School of Aerospace Engineering
Georgia Institute of Technology

Dr. David Tan
School of Earth and Atmospheric Science
Georgia Institute of Technology

Prof. Suresh Menon
School of Aerospace Engineering
Georgia Institute of Technology

Date Approved: May 9, 2008

ACKNOWLEDGEMENTS

I would like to thank everyone who made this thesis possible. First, I would like to thank my advisor, Professor Jerry Seitzman for his infinite patience and guidance on the path towards my PhD. His mentoring and motivation have allowed me to reach a higher level of understanding of my research and the world and have helped me through many obstacles along the way. Second, I would like to thank Prof. Seitzman as well as Dr. Brian Ritchie for introducing me into the world of PLIF, laser, and optics and the research skills that I needed for this work and future works.

Next, I would like to thanks the professors, research engineers, graduate students and undergraduate students at the Ben Zinn Combustion Lab. They have helped me through critical times that all PhD students have to go through such as qualifiers, proposals, research stagnation, and personal crisis times as well. There are a few that I have to personally thank: Muruganandam, Mohan, Rajesh, Yash, Santosh Sr. and Jr., Nori, Jp, Priya, Yogish, Shai, Sai. They made my life less stressful and have been with me through many of my crises during my stay at Georgia Tech. In addition to the people at the Combustion Lab I would like to thank my roommates, Joy, Stephanie, Hanh and Nanna, for putting up with me and tolerating my ups and downs during their stays with me.

Last, would like to thank my family for believing in me, providing me a base of operations that I know will always be there whenever I needed it. I can go forth in the world and know that I will always have their full support in any of my endeavors.

TABLE OF CONTENTS

LIST OF TABLES

LIST OF FIGURES

SUMMARY

An extension of the current acetone Planar Laser-Induced Fluorescence (PLIF) was formulated for mixing studies of fluids at subcritical and supercritical conditions. The new technique, called Planar Laser-Induced Fluorescence and Phosphorescence (PLIFP), employs the difference in the mass diffusivity of the denser (liquid) to the less dense (vapor/supercritical fluid) to delineate the interface where a phase change occurs. The vapor/supercritical acetone fluorescence emission signal is utilized to measure of the acetone vapor density, the mixture fractions and liquid acetone phosphorescence emission signal to determine the location of the phase interface.

The application of the technique requires the photophysical properties of vapor and liquid acetone to be known. Therefore a series of controlled experiments were done to determine their photophysics. The vapor fluorescence yield results were shown to be similar to the predicted values from the model. For a given pressure, the vapor fluorescence yield decreases with increasing temperature. For the temperature range tested, T/T_C from 0.5 to 1.2 or $\Delta T = 300$ K, there was a 33% decrease in the fluorescence yield. The corresponding fluorescence signal decrease by 24%. For a given temperature the fluorescence yield increases with increasing pressure. The fluorescence yield plateaus to twice its value at 1 atm for a given temperature and reaches the vale at approximately 30 atm. After p = 30 atm, or p/p_C of 0.625 for our case, change in the fluorescence yield is minimal. The liquid fluorescence signal is constant for pressures and temperatures range of p/p_C from 0.02 to 1.25 and T/T_C from 0.57 to 0.8. The liquid phosphorescence signal is invariant with pressure but decline exponentially with temperature. However,

the signal was still visible to be used for the interface location at high temperature. The phosphorescence spectra for two different wavelengths show very little red-shifting compare to their florescence emission spectra. Thus, the two signals cannot be discriminate through the spectra, but through time delay in the image acquisition.

The demonstration of the techniques shows it was able to provide quantitative measurements of acetone number density and the overall mixture fraction within the test chamber. Also, the size and mass of droplets that have broken off from the main jet were determined as well, though the ability is limited to small droplets (d~100 μm). In addition, the technique was able to delineate the low diffusivity (subcritical)/high diffusivity (supercritical) interface very well. At subcritical conditions, it was able to determine the vapor/liquid interface to within a few image pixels, which was caused by the optical resolution of the system. At supercritical conditions, the technique shows the interface moving into the as more of the liquid transition to supercritical fluid.

CHAPTER 1

1.1 INTRODUCTION AND MOTIVATION

In many practical combustion devices, such as liquid rockets or aircraft engines, fuel (or propellant) is injected into the combustion chambers in a condensed phase. It undergoes conversion to a gas and subsequently mixes with an oxidizer (or another propellant) prior to burning. In order to improve combustor design, there needs to be a better understanding of this process. In particular the evaporation and mixing process is of great interest for aeropropulsion engines because of the desire to minimize combustor (and thus engine) length.

1.1.1. Supercritical Fluids

The temperature and pressure within a combustion chamber can be very high. Typical conditions range from 20 atm and 2000 K for aircraft engines during takeoff to 100 atm and 4000 K for liquid rocket engines.[1] In many cases, these conditions correspond to transcritical or supercritical states of the fuel and/or oxidizer. A fluid becomes supercritical when it has exceeded its thermodynamic critical point as depicted in Figure 1.1. Supercritical fluids can behave like gases in some ways and are combination of both the vapor and the liquids in others; for example a supercritical fluid can have a density similar to standard liquid but the high diffusivity typical of gases. Thus, it is able to dissolve materials like a liquid and diffuse through solids like a gas.

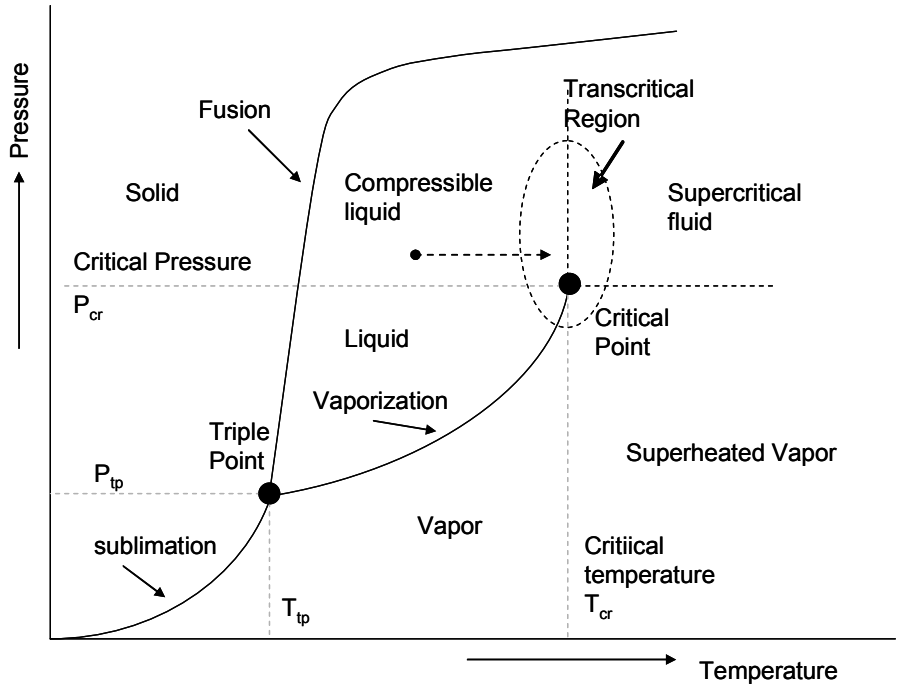

Figure 1.1: P-T diagram showing the different phases of a substance. Circled region shows the transcritical region of the substance, the region of interest of this study.

For example, Figure 1.2 displays images of CO_2 at various conditions.[2] In subcritical conditions, there is a sharp delineation between the liquid and gas phases, seen clearly in Figure 1.2a. As the temperature and pressure increase, that delineation becomes less clear, and it is no longer visible in the supercritical regime (Figure 1.2c), where the CO_2 is now uniform in density, but has a much higher density than is typical for a gas, i.e., 500 kg/m^3 at 150 atm and 300 K compared to 26 kg/m^3 for gaseous CO_2 at 10 atm and 300 K.

Thus, when a fluid is near the transcritical or supercritical region, how the fluid undergoes state changes is altered. At supercritical pressures, heating a "condensed-phase" (high density) propellant does not produce a distinct phase change from liquid to gas. In the subcritical regime, the phase change from liquid to gas is usually seen with

bubbles forming within the liquid or droplets forming from jets (Figure 1.2a). The delineation between the gas and liquid is there, is seen to move downward as more of the liquid becomes vapor, and disappears when the last of the liquid has evaporated. However, for critical fluids, the delineation is vague and disappears altogether when supercritical condition are reached. In addition, there are no bubbles forming from the fluid, with nearly zero latent heat of vaporization in the critical region (Figure 1.2b). In the case of a supercritical jet, instead of droplet formation and evaporation, the mixing and fluid breakup involves formation of finger-like ligaments at the edge of the jet that mix with the surrounding fluids in a fashion similar to a dense gas mixing with a lighter gas.[3-5]

a) b) c)

Figure 1.2: Subcritical to supercritical CO_2: a) subcritical, b) transcritical, c) supercritical (from Ref. 2)

Of particular interest is the sub-supercritical transition process itself. In the critical region, the fluid properties are very sensitive to small change in pressure and temperature. For example at 129 K, the density of nitrogen increases by 21% per degree Kelvin. Similarly, the specific heat increases by an order of magnitude to its maximum at

the supercritical temperature of 129.5 K and decreases just as quickly.[1] Thus, it is seen that a minute change in temperature at transcritical conditions can profoundly alter fluid properties. Also, the surface tension decreases to zero as conditions change from subcritical to critical. The reduction in the surface tension causes a high increase in the diffusivity of the fluid; this can greatly increase mixing rates, for example between a high density fluid injected as a jet into surrounding gas. In the transcritical region, other transport properties go through major changes, including thermal conductivity and momentum transport. Thus, the variations in fluid properties due to subcritical to supercritical transition can significantly affect jet breakup and mixing processes, and consequently combustion in high pressure applications.

Many aspects of mixing of a jet in transcritical-supercritical conditions have been studied. Research studies have included a subcritical jet entering a supercritical test section or a supercritical jet entering a subcritical test section,[6,7] as a single or coaxial jet entering a quiescence atmosphere. Wu *et al*. combined schlieren and shadowgraph techniques to visualize a supercritical ethylene jet injected into a subcritical nitrogen atmosphere ($P_{chamber} < P_{crit,}$, $T_{chamber} > T_{crit}$).[6] The back pressure was sufficiently low to choke (or nearly choke) the jet nozzle. For some back pressures, they noticed shock structures in the jet, similar to the shocks seen in underexpanded jets, demonstrating that a supercritical jet can act very much like a gaseous jet. The location of the shock disks were also close to the values predicted using real gas assumptions.

Oschwald *et al.*[1] investigated both single jet and coaxial jets under sub and supercritical conditions. They used shadowgraphy and spontaneous Raman scattering to determine the spreading rate and the density profile of the jet as a function of distance

from the exit. They found that the jet eventually reaches a self-similar shape downstream. Fractal analysis revealed that the atomization and mixing process of the supercritical jet resemble a turbulent dense gas jet mixing with a light surrounding gas, as opposed to the normal behavior of liquid sprays seen at subcritical conditions.[1]

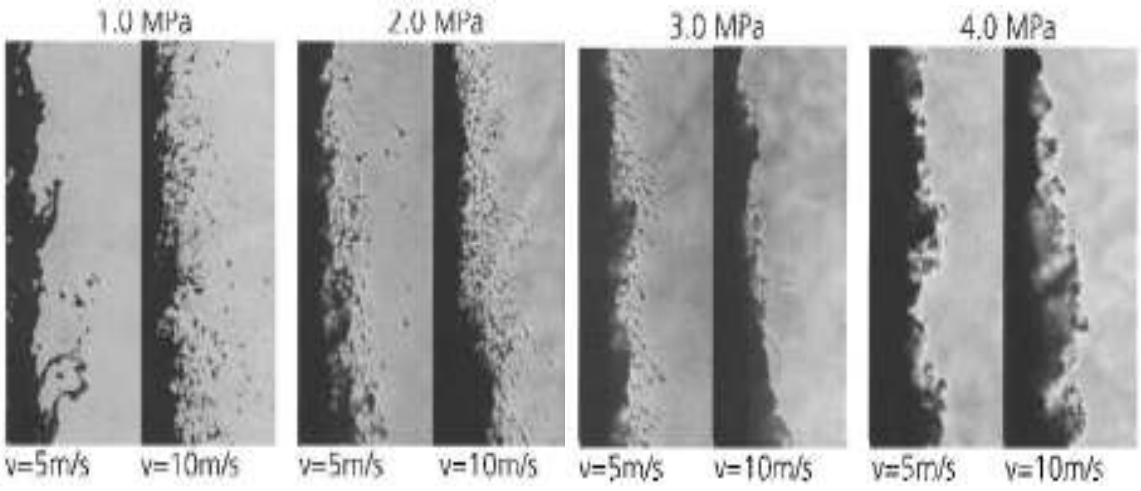

Figure 1.3: Shadowgraph images of liquid nitrogen injecting into subcritical and supercritical nitrogen environment.[4] Jet diameter - 1.9 mm, images size – 3.1×7.7 mm, 8 mm downstream of jet exit.

Chehroudi *et al.*[8] employed back-lit shadowgraph as well as Raman scattering to visualize imaging jet mixing of LN_2 injected into gaseous N_2. The signal from the Raman scattering images were used to determine the edge of the jet as a function of distance downstream, and the solutions found were close to the shadowgraph values. The calculated growth rate at supercritical conditions from the shadowgraph images followed the theoretical values for incompressible, variable-density mixing layers and previous experimental results for an incompressible, variable-density turbulent mixing layer. Prior research showed that the mixing layer is well approximated by the initial mixing region

of the axisymmetric jets where the liquid core is still intact.[3] Thus, the jet is seen to be more vapor-like rather than liquid.

Mayer *et al*.[4,5,9] also employed shadowgraph imaging and Raman scattering to provide length scale measurements and jet spread angles. The images also provide a good visual demonstration of the difference between subcritical/supercritical jet mixing (Figure 1.3). Theoretical Kolmogrov, Taylor and Integral length scales calculated from the k-ε equation is compared to the measured visible length scales. The measured values were calculated from the shadowgraph images using a two-point correlation function. The results are relatively constant and close to the predicted Taylor length scale. In addition, they found that the eddies within the jet are initially elliptical close to the jet exit but quickly approach a more circular shape suggesting rapid energy dissipation in the region, which would lead to the self-similar shape found by Oschwald *et al*.

Computational efforts have also been conducted to study the physics of fluids in supercritical conditions.[7,8,10,11] However, the computational modeling of these processes is extremely complicated due to the many changing properties of the fluids and the interactions between fluids in the flowfield. Thus, there is a need to acquire relevant data to validate the computational models.[12-14] Important properties that would be helpful in these efforts include profiles of density and mixture fraction, and jet core length and spread angle.

1.1.2 Diagnostic Techniques

The measurement approaches in many of the previous studies were shadowgraphy, schlieren, and Raman scattering. These optical approaches have been preferred, as they

are non-intrusive and do not alter the mixing processes. There are additional merits to each of these techniques, but there are also certain drawbacks. In its most quantitative form, Raman scattering is employed as a point measurement, with multiple species concentrations detectable at a single point. It can be used to provide two-dimensional images of the flowfield; however, only one species can be measured with a single camera and the low laser fluence associated with spreading a laser beam into a sheet results in low signals and thus poor signal-to-noise ratio measurements. Shadowgraphy can provide high quality images of the flowfield, however the result is spatially integrated along the line of sight. While this is acceptable for measurements in axisymmetric flows, the instantaneous flowfield of a turbulent jet is not axisymmetric. Therefore, it would be helpful to apply an imaging technique that can be used to determine the length scales, core length, spreading angle, location of the transition from subcritical-like to supercritical behavior and other mixing conditions with both spatial and temporal resolution. Planar Laser-Induced Fluorescence (PLIF) is such a technique.

PLIF is a non-invasive measurement technique that can provide qualitative as well as quantitative flowfield information.[15] In addition, it can provide temporal and spatial resolution of the number density as well as temperature, pressure, and velocity of the fluorescing molecules. As a resonant technique, PLIF requires a laser of a specific wavelength to excite a chosen specie, either naturally occurring or seeded, within the flowfield. Once excited to a high lying energy state, the molecule can emit a photon, creating the fluorescence signal. Unlike Raman scattering, signal levels can be quite high even with use of a laser sheet; as a resonant technique, PLIF cross-sections can be six orders of magnitude greater than for Raman scattering. Raman scattering also has

interference problem associated with the scattering and fluorescence from gases and surfaces, thus further reducing its signal to background ratio.[16]

The tracer can be added in small amounts to the fluid of interest or the fluid can be completely substituted with the tracer. An example of seeding approach is Planar Laser Induced Exciplex Fluorescence (PLIEF), where a small concentration of the tracer is added to the injecting fluid. The molecule exhibits a different emission spectrum depending on whether the tracer is in the liquid solution or vaporized.[17] However, the tracer becomes highly diluted as it mixes with the ambient fluid and the low tracer concentration leads to a low signal-to-noise ratio making the concentration measurements less accurate. The alternate approach there the fluid is substitute with a tracer as seen in studies of liquid dispersion,. Here, acetone has been used to substitute for a liquid fuel, thereby increasing the signal intensity, even in region of high mixing, and also reducing the numbers of species within the system.[18] This allows for the measurements of multi-species mixing without overcomplicating the flowfield.

PLIF of acetone has been demonstrated to be a powerful approach for jet mixing studies in (subcritical) gas jet mixing, providing qualitative and quantitative information within the flowfield.[19-22] Vapor acetone has been well researched and fluorescence yield models for acetone vapor have been developed.[23,24] However, it has not been extended towards the high pressure and temperature range that is near the critical region or above. For example, the experimental measurements of fluorescence yield by Braeuer, *et al*. were made to only 20 atm and 690 K.[24] Figure 1.4 shows the location of where the models have been validated on a P-T diagram. The region where the model is validated is very far from the supercritical region of acetone, especially the region where the liquid or

gas transition to supercritical fluid. Determining whether the model works in the transcritical to supercritical regime would greatly increased the versatility of acetone PLIF technique in higher pressure and temperature conditions.

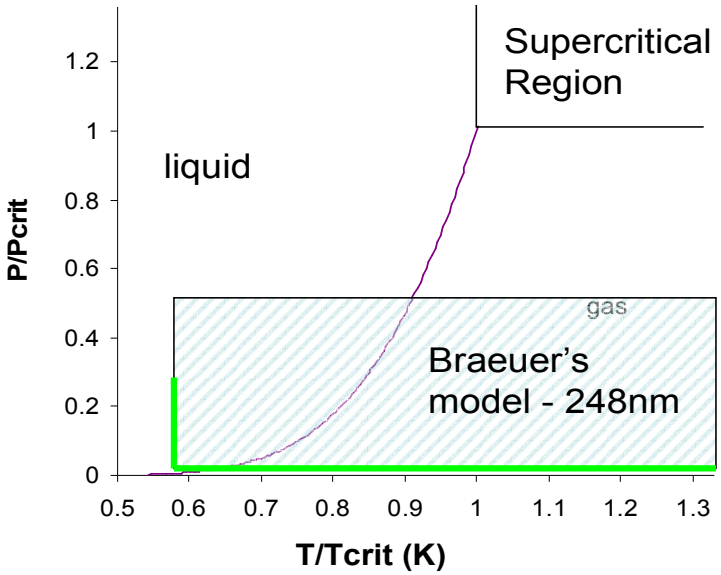

Figure 1.4: Regions where the acetone vapor fluorescence yield model has been validated. Green line - Thurber's model. Rectangle - Braeuer's model.

Additionally, the technique itself has not been applied in any flowfield with pressure higher than ~12 atm. In addition, little attention has been given to laser-induced radiation from liquid acetone. Therefore, there are questions that need to be addressed before acetone PLIF can be applied as a diagnostic technique to multi-phase flowfields or to high temperature and pressure conditions. Thus, to extend the diagnostic technique to these other conditions, it is important to understand the photophysics of the liquid phase and also the near-critical to supercritical phase of acetone.

1.2 OBJECTIVES

The main goal of this work is to develop a technique that is able to: 1) provide flowfield imaging of jet breakup of a high density fluid during the critical process as the injected propellant transitions to a supercritical fluid, and 2) provide quantitative information on mixing between the jet fluid and the surrounding flow. The optical technique developed in this thesis is called acetone Planar Laser Induced Fluorescence and Phosphorescence (PLIFP). This technique employs emission signal of vapor/supercritical acetone fluorescence and both the fluorescence and phosphorescence from liquid acetone. These goals can be further separated into two main tasks.

The first task is to characterize acetone photophysics at elevated pressure and temperatures in order to extend the current acetone PLIF technique to those conditions. This will includes the vapor, liquid and supercritical phase of acetone. Therefore, the variation of the photophysical parameters, i.e., absorption cross section, fluorescence yield, and collisional energy transfer, with temperature and pressure needs to be determined. The vapor acetone fluorescence yield models developed have only been verified at subcritical conditions.[23,24] So it is also helpful to ascertain whether the models are useful over a larger range of conditions, or do they need to be revised?

The information from the acetone photophysics is used to develop a methodology for delineating the critical interface, i.e., the region where the fluid stops behaving like a subcritical liquid and has transport properties more like a gas. The interface is well-defined in the subcritical regime (e.g., by the large density change), but is less well-defined at supercritical pressures. Defining this interface is helpful to understand jet breakup and mixing, as well as useful for comparison to computational models.

The last task of this work is to demonstrate the technique within a subcritical and transcritical/supercritical flowfield to determine it ability to measure the density of the acetone, the mixture fraction within the system, etc. Also, its effectiveness in demarcating the subcritical/supercritical interface needed to be verified as well. In addition to determining the mixture fraction or density within the flowfield, the concentration, mass within a droplet at subcritical conditions can also be found. The liquid acetone photophysics can provide a quantitative analysis of the liquid droplets broken off from the main jet. However, this technique is limited to small droplets due to the short optical depth of acetone for the excitation wavelength used in the study. For acetone, the laser energy will reduce by 1/e, or 36%, after 30 μm and by $1/e^3$, or 5%, after 85 μm. Thus it is only possible to determine the total mass for small droplets of the similar size as the optical depth or smaller.

1.3 THESIS OUTLINE

The rest of this thesis is organized as follow. The first section of Chapter 2 provides a more detailed review of supercritical fluids and their properties. The next portion provides a background to acetone and acetone PLIF, including models for the acetone vapor fluorescence yield. Lastly, the techniques used to determine the low diffusivities/high diffusivities interface is described. Chapter 3 provides details of the experimental setup and the data analysis methods. Chapter 4 details the results for the experiments to determine the photophysical properties of both vapor and liquid acetone over temperatures and pressures ranging from sub to supercritical. Chapter 5 presents the quantitative results for the application of PLIFP to determine the mixture fraction and the

low diffusivities/high diffusivities interface within a high pressure and temperature combustor. In addition, results of quantitative liquid acetone PLIF of droplets is shown and the assumptions made in quantifying the results are discussed. Chapter 6 includes the conclusions and the suggestion for future work in this area.

CHAPTER 2

BACKGROUND

This chapter provides a brief background of the subjects covered in this thesis. The first section describes the variation in physical properties of supercritical fluids in comparison to subcritical fluids. The second section provides background on the measurement approach, divided into a general introduction to PLIF and details specific to acetone. The last section details the technique used to determine the subcritical/supercritical interface.

2.1 SUPERCRITICAL FLUIDS

A supercritical fluid is defined as any substance whose temperature and pressure is above its thermodynamic critical point. Below this critical point, there is the possibility of the coexistence of two or more phases. For example, the liquid and vapor phase of a substance are at equilibrium with each other and can be visualized through the vapor pressure curve of the substance. The vapor pressure curve ends at the critical point and above this point, only one phase exists. Clifford[25] has suggested that there is only one phase at and above this point due to the increase in internal energy, and thus the relative speed of the molecules. For high relative kinetic energy between molecules, their attractive force is not strong enough for the two approaching molecules to become bonded within their brief interaction time, therefore preventing condensation (i.e., liquid formation).

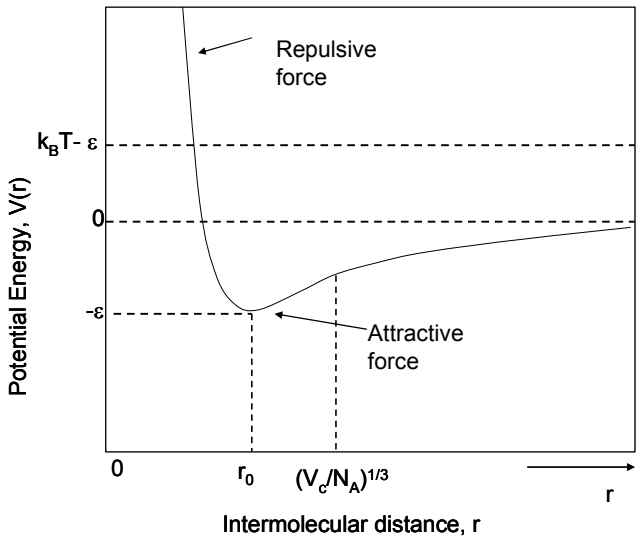

Figure 2.1: Image of intermolecular pair potential function.[25] The minimum distance $(V_c/N_A)^{1/3}$ is larger than distance needed for two molecules to bond, r_0.

This is illustrated in the energy potential diagram shown in Figure 2.1. The intermolecular potential force is plotted against intermolecular distance. As the molecules move towards each other, there is an attractive force pulling them even closer, until they reach a separation distance r_0, corresponding to the maximum attractive potential energy, $-\varepsilon$. For smaller separations, the net force between the molecules is repulsive, causing the molecules to move apart. The attractive potential energy is compared to the thermal energy, which is illustrated for the critical temperature as the dashed line at $k_BT - \varepsilon$. This value is higher than zero, so at and above the critical temperature the kinetic energy of the molecules is too high to allow for the intermolecular interactions required to condense. Also included in the figure is a characteristic spacing between supercritical fluid molecules, given by the cube root of the fluid's specific volume at the critical point divided by Avogadro's number $(V_c/N_A)^{1/3}$. This value is higher than the average minimum distance one expects to find if the two molecules were to form an

intermolecular bond. Thus the molecules are unable to reach the minimum distance required to condense, regardless of the density of the fluid.[25]

At the critical point, certain properties of the fluid resemble that of a liquid while others are more vapor-like. Figure 2.2 shows some of the properties of a substance as a function of temperature pressure ranging from subcritical to supercritical. In the first two plots, the blue curve is subcritical, red is near critical, and green is supercritical. [26] At the subcritical pressure, there is a sharp distinction (discontinuity) in the properties between the liquid and vapor (with a transition at ~300 K). For example, there is a large and sudden drop in density (as temperature is raised) for the subcritical case. The density decrease starts to become gradual near the critical condition, though there is still a large density change as the temperature exceeds the critical point. Even with the decrease, however, the supercritical density is an order of magnitude higher than that for the subcritical vapor. For the specific heat, there is a small but sudden drop in its value between the vapor and liquid at subcritical conditions. But as the pressure increases to near critical values and beyond, the specific heat matches the overall increasing trend seen for the subcritical liquid. There is a large local increase near (or slightly above) the critical temperature, similar to the infinite change one would observe at subcritical conditions if the phase change enthalpy was included in the specific heat. At higher pressures, this peak is reduced. The behavior of the mass diffusivity is similar to that of the density, as shown in Figure 2.2c for CO_2.[27] The diffusivities of typical solutes into liquid are also shown, and the values are one to two orders of magnitude smaller than for the diffusivity of supercritical CO_2. The diffusivity for supercritical CO_2 is similar to its subcritical vapor, and an order of magnitude greater than subcritical liquid. Therefore it is

observed that when a liquid transition from subcritical to critical or critical, its ability to diffuse or allow other species to diffuse into it increases significantly.

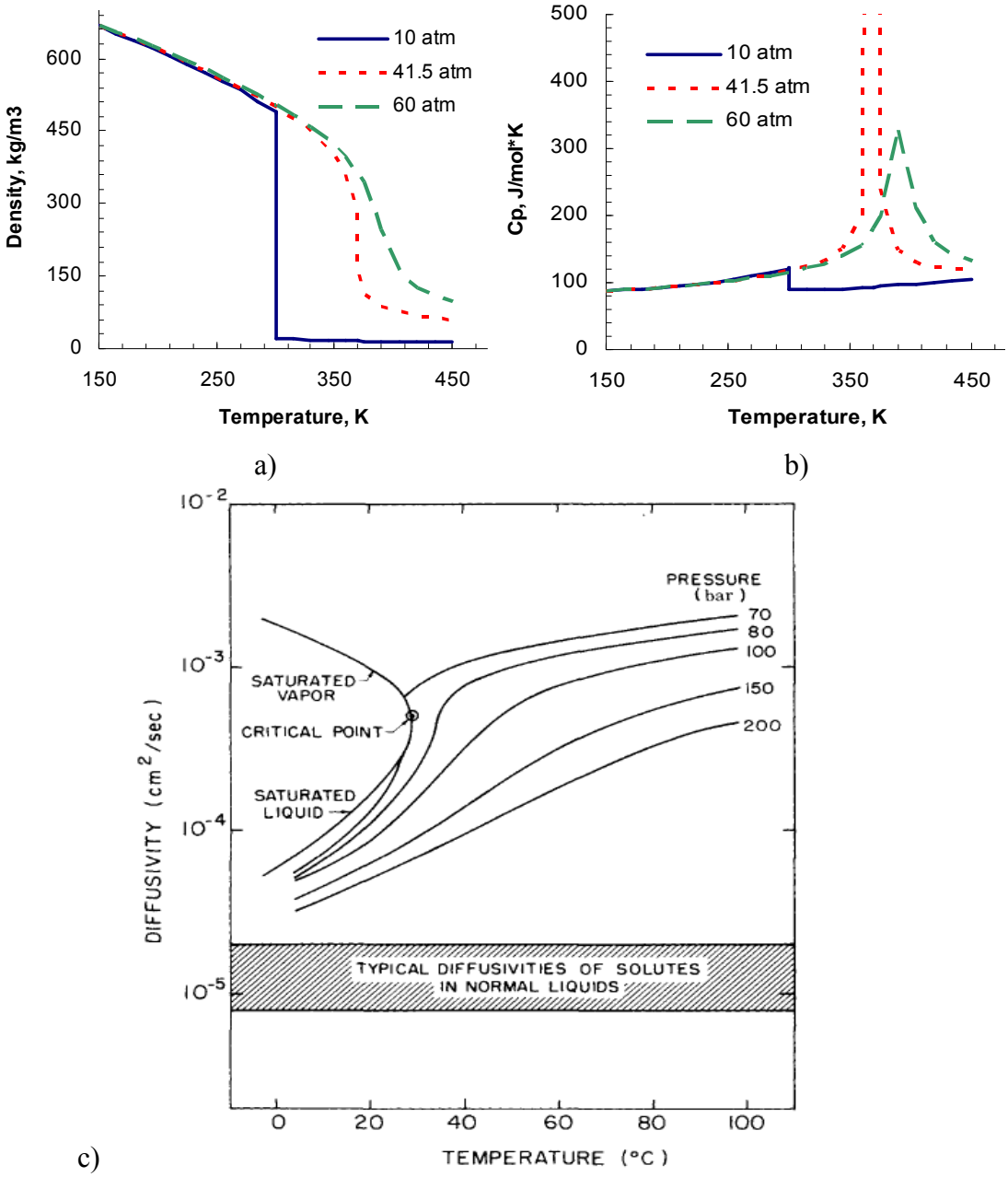

Figure 2.2: Fluid properties from subcritical to supercritical conditions: a) and b) density and specific heat for propane as a function of temperatures at three pressures;[26] c) binary diffusivity for CO_2 (with itself or a similar size molecule).[27]

2.2. DIFFUSION OF GAS INTO LIQUID

The diffusion rate between vapors is extremely high; however, the diffusion rate of a vapor into a liquid is much slower as seen in the mass diffusivity plot shown in Figure 2.2. The diffusion of a substance, the solute, into another substance, the solvent, is described using Fick's second law of diffusion, Eqn 2.1. Here ϕ is the concentration of the solvent acetone in mol/L and D is the diffusion coefficient.

$$\frac{\partial \phi}{\partial t} = D \frac{\partial^2 \phi}{\partial r^2} \qquad \text{Eqn 2.1}$$

The diffusion coefficient for a solute into a solvent can be calculated using the equation developed by Wilke and Chang, Eqn 2.2.[28] Here, T is the temperature in Kelvin, $M_{solvent}$ is the molecular weight of the solvent in g/mole, V_{solute} is the molar volume of solute in cm^3/gmole and η is the viscosity of the solvent in centipoises and the diffusion coefficient result is given in cm^2/s. $\psi_{solvent}$ is an "association" parameter for the solvent.

$$D_{AB} = 7.4 \times 10^{-8} \frac{T(\psi_{solvent} M_{solvent})^{1/2}}{V_{solute}^{0.6} \eta} \qquad \text{Eqn 2.2}$$

Using these relations an example of a solute, oxygen in this case, diffusing into a nonevaporating, laminar liquid jet, acetone for example, injected into quiescent air at 300 K, 1 atm is shown in Figure 2.3. Here the jet diameter is 300 μm and the jet velocity is 1 m/s. Result are shown for various residence times; thus a 10 ms time corresponds to a downstream distance of 10 mm (or ~33 jet diameters). After 10 ms, the oxygen concentration is 1×10^{-5} mol/L at a depth of 33 μm into the liquid jet; the corresponding

value at 50 ms the distance is 70 μm for the same concentration. The aerated (saturated) concentration of oxygen in liquid acetone is 1.5×10^{-3} M (mol/L).[29]

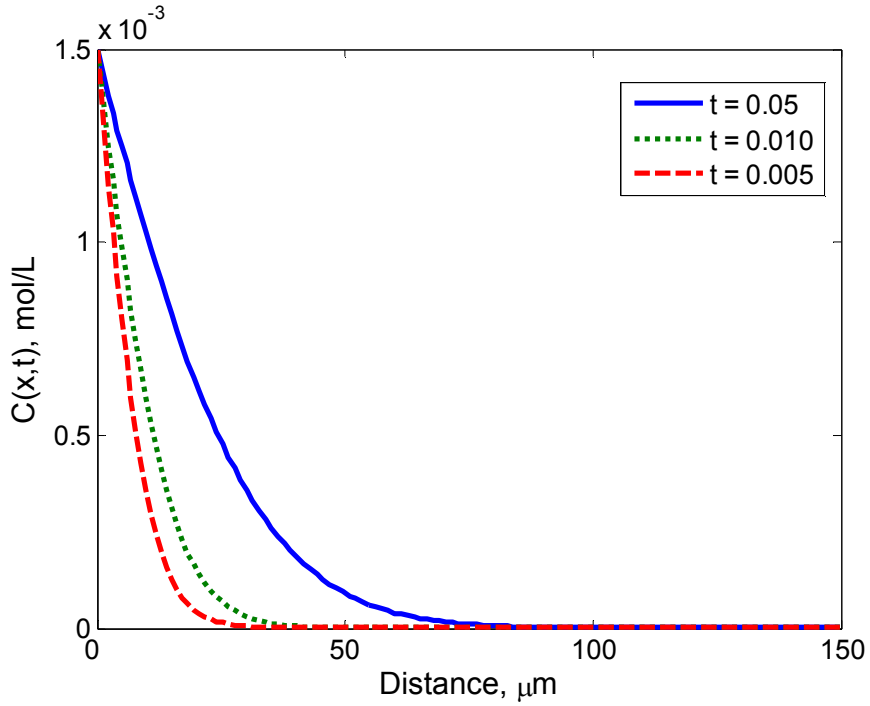

Figure 2.3: Concentration of oxygen as a function of radial distance into the jet for various residence times; jet radius=150 μm, V_{jet} =1 m/s.

The diffusion of vapor into a jet at transcritical and supercritical conditions will be different compare to subcritical diffusion. At transcritical to supercritical conditions, the diffusivity of fluid will increase thus allowing other molecules to diffuse faster into fluid than when it is liquid. However, when the fluid transitions to supercritical its density is decreasing. This causes the fluid to expand and it will push other fluids within the region away from the jet vicinity also. This process can be explained using Stefan flow. Stefan flow is generated by the removal or addition of a species at an interface, causing a mean

velocity with the fluid as the fluid next to the interface is being removed or added by the processes occurring at the interface. Examples of processes that could generate Stefan flow are evaporation, condensation, chemical reactions, etc. The expansion will push the surrounding molecules away from the jet. The thermal expansion process due to the decrease in density of the fluid will cause other fluid in the system, in this case air, to be removed in the vicinity of the jet. However, this will cause a concentration gradient in the opposite direction, thus this will cause the surrounding molecules to diffuse back into the vicinity of the jet through mass diffusion.

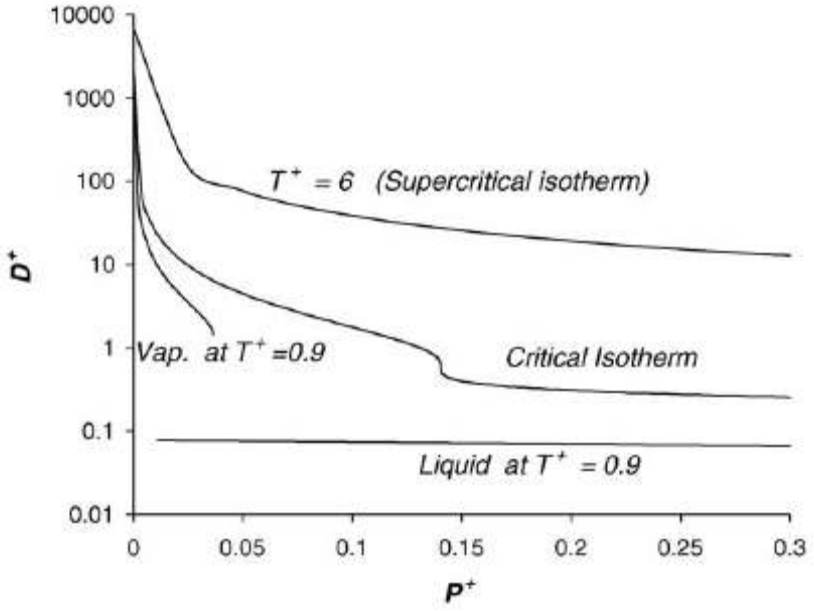

Figure 2.4: Self-diffusion coefficient, D^+ for Lennard-Jones Fluids as a function of pressure P^+ at varying T^+ values. Figure from Ref. 32.

Typically, the diffusivities of gas are about 3 to 4 orders of magnitude higher than the diffusivities of liquid.[30] Comparing between the supercritical fluids of carbon dioxide and water and its liquid counterpart, the supercritical fluids diffusivities are two orders of

magnitude higher.[30,31] Zabaloy, et al. was able to model the self-diffusion of different molecules using the Lennard-Jones analytical relationship.[32] They were able to estimate the self-diffusion coefficient relatively close to the experimental values. From their results, an approximation for the self diffusivities of acetone in liquid, vapor, and supercritical fluid state are determined. (see Figure 2.4).

The thermal expansion process of transcritical and supercritical fluids was well explained by Arias-Zugasti, et al.[33] At low supercritical pressure with high temperature surrounding the substance, as the fluid heats up, Stefan flow will induce a convective flow that push the "vaporized", heated fluid, away from the main jet. This convective flow is equal but opposite in direction to the conductive heat flow. The two competing processes will create an interface that will recede into the liquid as more of the fluid is heated. The thermal expansion process is fast near the critical point due to the high thermal expansion coefficient, which maximized at the critical point. As the pressure increases, however, the thermal expansion coefficient decreases and broaden, thus reducing the thermal convection process until it becomes negligible compare to the conduction process at very high pressure. This convection process will be significant near the critical point, but as the test condition moves away from the critical point, the fluid behave more like a vapor and the convection of other fluids away from the jet will be minimal. This will allow more oxygen to diffuse into the jet at rates close to the vapor-vapor diffusion rate.

Using the continuity equation, the energy conservation equation and definition for the thermal expansion coefficient, Aris-Zugasti, et al. derived the equation for the thermal expansion induced velocity field. Here the divergence of the conductive heat flow

produced by the temperature gradient acts as a source term for the thermal expansion velocity field.

$$\vec{\nabla} \cdot \vec{v} = \frac{\beta}{\rho c_p} \vec{\nabla} \cdot (\kappa \vec{\nabla} T) \qquad \text{Eqn 2.3}$$

where

$$\frac{\beta}{\rho c_p} = \frac{1}{P_c}\left(1 - \frac{1}{\gamma}\right)\frac{V^2}{\Pi V^2 + 3} \qquad \text{Eqn 2.4}$$

Here V and Π are the reduced volume and the reduce pressure, respectively, β is the thermal expansion coefficient, γ is the specific heat ratio. Since κ, the thermal conductivity, is only a function of temperature, it can be added to the constant, $\frac{\beta\kappa}{\rho c_p}$. For a system with the same temperature gradient, the thermal expansion rate will be dependent on the constant.

2.3 ACETONE PLIF AND PHOTOPHYSICS

2.3.1 PLIF Overview

In PLIF measurements, a laser beam is used to excite molecules of a chosen species, which can either be injected into the system as tracers or be naturally occurring within the flowfield. The molecules are excited from a low energy state to a higher lying state from which they can return to a lower state by spontaneous emission, i.e., fluorescence.[34] In some cases, the excited molecules can also de-excite though another emission process, phosphorescence which has a much longer lifetime than fluorescence. The fluorescence intensity is related to the concentration of the species in the low energy state, which is

also proportional to the concentration of the molecule within the flowfield. Thus PLIF can be used to determine the mixture fraction within a flowfield. The good spatial and temporal resolution as well as the large range of operating conditions provided by PLIF makes it an important tool for researchers.

Different types of naturally occurring species have been used for PLIF measurements. PLIF of OH, NO, CO, and CH, which are intermediate reaction species naturally found within reacting hydrocarbon flowfields, have been used to characterize various aspects of the combustion process in a combustor.[35,36] For example, OH and CH PLIF can be used to locate the flame zone in a combustor, as well as determine the gas temperature.[36,37] The advantage of using species naturally found in the system is that it is simpler to operate since it does not need a system to mix and inject a tracer into the fuel and flow. Also, the species are naturally occurring, it will not alter the properties of the fluids in the combustor and thus the flowfield. However, most of the accessible species are created during combustion; thus they are unable to provide information of the flowfield before the combustion process, e.g., fuel/oxidizer mixing. The majority of fuels and oxidizers themselves are not well-suited for fluorescence measurements.[43]

Thus to obtain information on mixing, one can add fluorescence tracers to the fuel or the oxidizer. Many tracers that have been used in PLIF diagnostics, such as SO_2, benzene, acetone, pentanone, biacetyl, and acetaldehyde.[38,39,40,42] Determining which tracer is best depends on the experiments to be done. For example, it is advantageous to choose a tracer with similar properties as the component to which it is added. In addition, the tracer's spectral properties should be compatible with available laser and camera technology Also, it should survive and provide information at the temperature and

pressure conditions desired. Furthermore, the tracer should be easily accessible, inexpensive, and not hazardous when used.[38]

2.3.2 Acetone and Its Photophysics

Acetone (C_3H_6O)is a ketone with one carbonyl group and two methyl groups (Figure 2.5), and it has a molecular weight of 58.08 kg/kmol. It is the simplest molecule in the ketone group and is the most often used in PLIF measurements. It is volatile, with a melting point at 178 K, a boiling point at 329 K, and and autoignition temperature of 738 K at atmospheric pressure. Acetone has a high vapor pressure at room temperature (around 0.3 atm at 25ºC). The high concentration allows excellent signal levels to be achieved. Acetone's critical point is 48 (± 4) atm and 508 (± 2) K, which is similar to the critical point of kerosene, a standard fuel in aeropropulsion engines.

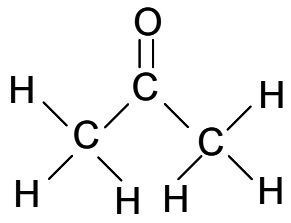

Figure 2.5: Chemical configuration of acetone.

Acetone PLIF has been used extensively for gaseous mixing measurements because of the linear relationship between the fluorescence intensity, acetone concentration, and laser power in isobaric and isothermal environments.[34] Thus the concentration can be

easily calculated from the images acquired. In addition, acetone has a low toxicity,* compare to other tracers, such as benzene, SO_2, or acetaldehyde, inexpensive, and easily acquired thus making it even more attractive as a fuel substitute.

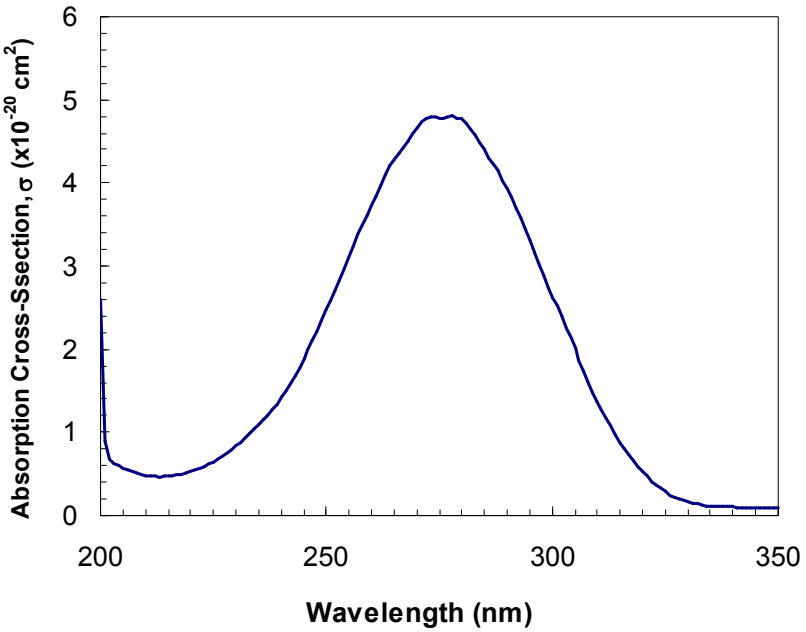

Figure 2.6: Acetone absorption cross-section as a function of wavelength at 298 K.[40]

The vapor acetone absorption cross-section was measured by Lozano (Figure 2.6).[40] Acetone absorbs light primarily in the range 220–320 nm, with the maximum absorption at ~275 nm. The spectrum shows no distinctive individual vibrational bands, rather all the vibrational energy levels are merged into one single band. The broad spectrum is an advantage for acetone, allowing it to be easily accessible by many lasers, e.g., at 266 nm through the 4th harmonic of a ND:YAG laser, at the 248 nm output of a KrF excimer laser, and at the 308 nm output of a XeCl excimer laser. The absorption cross-section is

* However, care should still be taken not to be exposed to acetone for a long time or at high concentration.

seen to increase with temperature across the absorption spectrum. The absorption cross-section as a function of temperature was measured by Thurber at a few wavelengths.[41] The absorption cross-section variation with temperature for 266 nm, the laser wavelength used in this work, is shown in Figure 2.7. The cross-section has a nearly linear rise with increasing temperature over the shown temperature range. In fact, the linear fit shown in the figure deviates from the measured data by less than 5%, and excluding the 300K point, the deviation is less than 2%.

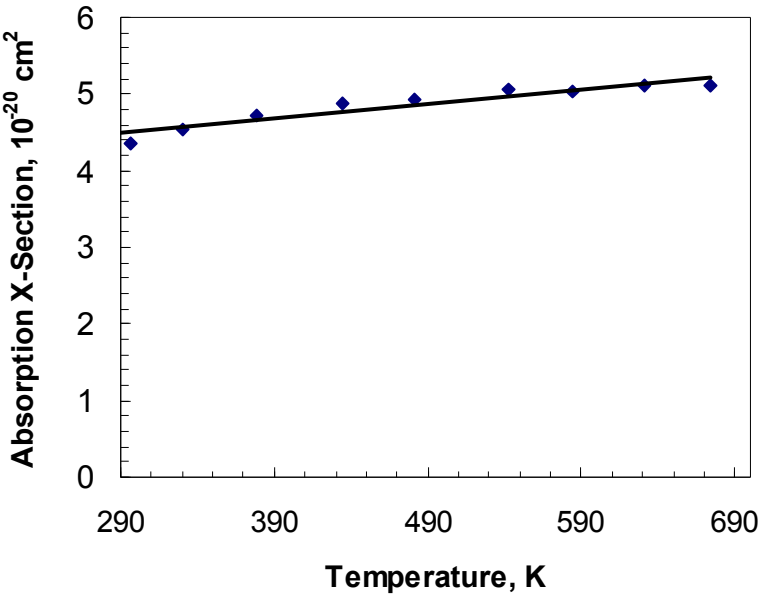

Figure 2.7: Absorption cross section as a function of temperature for 266 nm excitation. Black line is a least-square linear fit.

Acetone fluoresces in the range 350–550 nm with a maximum near 405 nm. Acetone can also phosphoresce, with a spectrum that is slightly red-shifted from the fluorescence spectrum, in the range (~350–600 nm). Figure 2.8 shows a simplified model of the acetone excitation and de-excitation process. Laser excitation at a wavelength within the

absorption band of acetone can excite a molecule from its ground singlet state (S_0) to a higher electronic singlet state. From the excited singlet state, the acetone molecules can be de-excited from its singlet state via either radiative or non-radiative processes. The "allowed" radiative process from the excited singlet back to the ground singlet state is called fluorescence. The fluorescence is characterized by a short lifetime of a few nanoseconds. If the acetone crosses over to the excited triplet state (T_1), the "dipole unallowed" radiation from the triplet to singlet configuration is known as phosphorescence, which is characterized by a weak transition probability and therefore a much longer lifetime compared to the fluorescence.

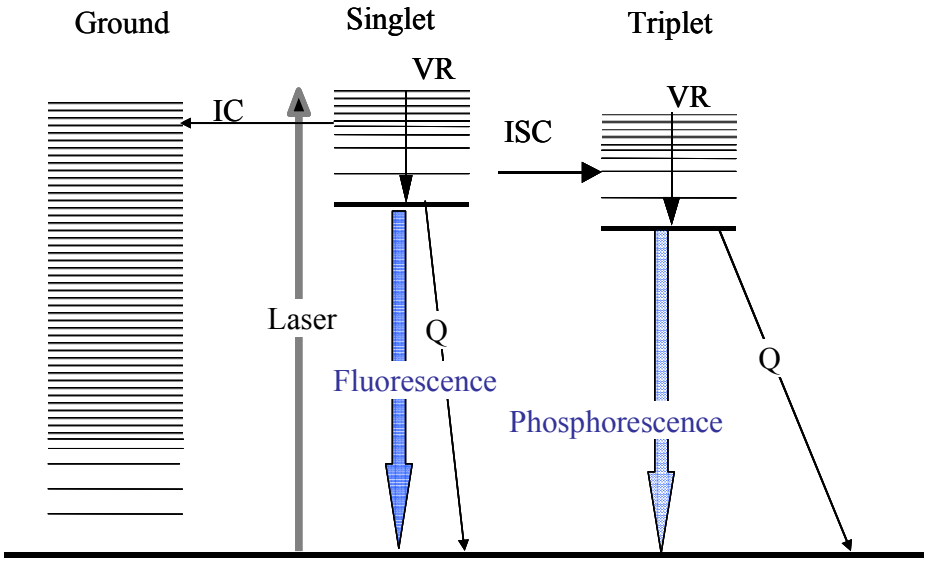

Figure 2.8: Simplified model for acetone PLIF

The relevant, non-radiative energy transfer processes include internal conversion, intersystem crossing, vibrational relaxation, and collisional quenching. Internal conversion is very slow de-excitation process due to the high energy difference between the singlet state and the ground state and is typically neglected since it is much slower

compare to other processes. Intersystem crossing involves transfer of energy from the first excited singlet state to the first excited triplet state (T_1). Vibrational relaxation is the reduction in the vibrational energy of the molecules due to collisions with other acetone molecules. Collisional quenching occurs when the excited acetone molecules are de-excited to the ground electronic state due to collision with other molecules, with oxygen being especially able to quench the acetone triplet state.

In general the fluorescence and phosphorescence signal can be represented by Eqn 2.5:

$$S = \eta_{optic}\left(\frac{E}{hc/\lambda}\right) dV_c n_{acetone}(P,T)\sigma(\lambda,T)\phi(\lambda,T,P,[O_2]) \qquad \text{Eqn 2.5}$$

where η_{optic} is the collection optics efficiency, E is the energy fluence of the laser, hc/λ is the energy per photon of the exciting laser, dV_c is the collection volume, $n_{acetone}$ is the number density of acetone, σ is the absorption cross-section of acetone, and ϕ is the fluorescence or phosphorescence yield. η_{optic}, E, hc/λ and dV_c are experimental setup variables and thus not a function of flow conditions. The absorption cross-section and fluorescence yield have been measured by Lozano[38,40] at room temperature and pressure and later by Thurber[42] at slightly higher temperature and pressure conditions.

The fluorescence yield can be written as the ratio of the fluorescence rate to the summation of all the competing rates, as shown in Eqn 2.6.

$$\phi_f = \frac{k_f}{k_f + k_{ISC} + k_{IC} + k_Q} \qquad \text{Eqn 2.6}$$

Here, the k_f is the fluorescence rate, k_{ISC} is the intersystem crossing rate, k_{IC} is the internal conversion rate and k_Q is the singlet quenching rate, where all the rates are effective rates for the complete vibrational manifold of the excited singlet state.[43]

From previous acetone vapor studies, k_{IC} is generally observed to be small compared to other rates and can therefore be neglected.[43] The actual intersystem crossing rate varies with the vibrational energy level of the molecules; the higher the S_1 vibrational energy level, the faster the intersystem crossing rate. Vibrational relaxation, which is an intermolecular process, moves molecules to lower vibrational energy levels. So k_{ISC} is inversely dependent on the collisional vibrational relaxation rate, k_{coll}, of the molecules. For the vapor phase, k_{coll} increases with pressure. For subcritical liquid acetone, however, k_{coll} should not vary significantly with pressure, since the liquid density, and thus the intermolecular collision rate, is nearly pressure independent. The behavior of k_{coll} at supercritical conditions would likely be bounded by these two limiting cases.

The effect of temperature and pressure changes on the fluorescence yield depends on the relative change in k_{ISC} and k_Q. For low densities, k_{ISC} can dominate the collisional singlet quenching rate k_Q, in which case the dependence of k_Q can be neglected. Otherwise k_Q would be expected to generally increase with density, and therefore pressure if the fluid is not nearly incompressible. k_{ISC} can also change with temperature, because the initially excited vibrational energy depends on the Boltzmann distribution of the ground electronic level and because k_{coll} is also temperature dependent. For example, the molecules will be excited to a higher vibrational energy level as temperature is increased. For previous acetone vapor studies, the net result was a decrease in the fluorescence yield with temperature.[41,43] While quenching of fluorescence has been

shown to be negligible for low pressure vapor acetone, increasing oxygen concentration can alter the fluorescence yield at higher pressures due to oxygen-assisted intersystem crossing.[23,43]

Similarly, a higher k_{ISC} allows more molecules to be deposited in the triplet state, increasing the probability that the molecules will phosphoresce and thus the phosphorescence yield. However, the increase in phosphorescence yield could be opposed by enhanced triplet state quenching. Acetone phosphorescence has been shown to be highly sensitive to collisional quenching by oxygen; its lifetime and signal are reduced dramatically even in the presence of minute quantities of oxygen.

The fluorescence lifetime is dependent upon the fluorescence rate, k_f, and the rate of the other relaxation processes. Based on the simple three-level model shown in Figure 2.8 (ground singlet, excited singlet and excited triplet, neglecting vibrational and rotational sublevels), the de-excitation rate of the excited molecules is given by:

$$-\frac{d}{dt}\left[M_{excited}\right] = (k_f + k_{ISC} + k_{IC} + k_Q) \times [M_{excited}] \qquad \text{Eqn 2.7a}$$

Integrating this, we get:

$$\left[M_{excited}\right] = [M_{excited}]_0 \times e^{-(k_f + k_{ISC} + k_{IC} + k_Q)t} \qquad \text{Eqn 2.7b}$$

The time, t_f, when the concentration has decreased by 1/e, i.e., the fluorescence lifetime is given by Eqn 2.8. The intersystem crossing rate is generally much faster compared to the other processes. Thus, the fluorescence lifetime is nearly equal to the inverse of the intersystem crossing rate.

$$t_f = \frac{1}{k_f + k_{ISC} + k_{IC} + k_Q} \Rightarrow \frac{1}{k_{ISC}} \qquad \text{Eqn 2.8}$$

The phosphorescence lifetime under the same assumptions is given by a similar relation, except the rate of relaxation of triplet acetone is dependent upon all the relaxation processes available to it. Integrating the equation and solving for the time required for the triplet acetone concentration to reduce to 1/e, the phosphorescence lifetime is given by:

$$t_{phos} = \frac{1}{k_{phos} + k_{Q_p} + k_{other}} \qquad \text{Eqn 2.9}$$

where k_{Q_p} is the quenching rate for the triplet state and k_{other} represent any other relaxation processes that could be important for triplet acetone, e.g., predissociation. The quenching rate is dependent on the concentration of the quenchers, with oxygen typically being the dominant quencher, though acetone self-quenching could be important for undiluted conditions.

The Stern-Volmer equation, Eqn 2.10, can be used to estimate the effect of the quenchers along the jet. [46,47] The equation states that the ratio of the intensity, I, at any point to the intensity close to the jet exit (I_o) can be determine from the phosphorescence lifetime without the quencher, t_0, the quenching rate constant, r_Q, [*L*/(mol s)], and the quencher concentration, c_Q, [mol/L].

$$\frac{I_0}{I} = 1 + r_Q t_0 c_Q \qquad \text{Eqn 2.10}$$

$$r_Q = \frac{8RT}{3000\eta} \qquad \text{Eqn 2.11}$$

In conditions where the quenching rate is limited by the diffusion of the quenchers into the medium, as seen for quenchers diffusing into liquid, the quenching rate is assumed to equal the diffusion rate of the quenchers into liquid. This diffusion rate can be calculated from the Debye equation, Eqn 2.11.[44-47] The Debye equation gives an approximate diffusion rate constant of a dilute solute, the quenchers, within a solvent as a function of the temperature of the solution, the gas constant, and the viscosity of the solvent, η. It is able to calculate the quenching rate constant of oxygen within 5 percent of the calculated values from the work of Bortolus *et al*.[45]

Research efforts have concentrated mainly on the vapor phase of the acetone PLIF, and thus the photophysics of vapor acetone PLIF is relatively well understood. A model proposed by Thurber describes the fluorescence process and predict the fluorescence yield of vapor acetone.[22,23,41] The model constants were adjusted to match experimental data from the same investigation at temperatures up to 1000 K and pressuress up to 10 atm. This model was later modified by Braeuer *et al.*[24] to match their experimental data at pressures up to 20 atm. Their results suggested that the original model constants resulted in over-predictions of the fluorescence yield and thus the overall fluorescence signal for pressure higher than 10 atm. The modified model used a different virial equation of state instead of the perfect gas equation to determine the density of the bath gas at elevated temperature and pressure. A polarity parameter is added to the Lennard-Jones collision rate calculated to take into account the collisions between the polar acetone molecules

and nonpolar bath gases (e.g., N_2, O_2, and CO_2). Both of these modifications alter the collision rates, and thus the vibrational relaxation rates of the molecules. In addition, they also modified the equation for the intersystem crossing rate, to match their data, since higher vibrational energy levels were excited with their shorter wavelength KrF excimer laser (248 nm).

The general model proposed for the fluorescence yield by Thurber is shown in Eqn 2.12.

$$\phi_{fl} = \frac{k_f}{k_f + k_{coll} + k_{NR,1}} + \sum_{i=2}^{N-1}\left(\frac{k_f}{k_f + k_{coll} + k_{NR,i}} \prod_{j=1}^{i-1}\left[\frac{k_{coll}}{k_f + k_{coll} + k_{NR,j}} \right] \right) + \frac{k_f}{k_f + k_{NR,N}} \prod_{j=1}^{N-1}\left[\frac{k_{coll}}{k_f + k_{coll} + k_{NR,j}} \right] \quad \text{Eqn 2.12}$$

Eqn 2.12 shows the fluorescence yield as the summation of the fluorescence yields from each of the vibrational energy levels in the first excited singlet state. In the equation, k_f is the fluorescence rate and k_{coll} is the collision rate, both of which are assumed to be independent of the vibrational level. (The collision rate is used to determine the vibrational relaxation rate.) On the other hand, k_{NR}, which is the intersystem crossing rate, is a function of vibrational energy level. The first term of the equation represents the fluorescence yield of the initially excited vibration level. The second term is the fluorescence yield for the vibrational energy levels between the initially excited vibration level and the thermalized level. The thermalized level is chosen to have an energy that represents the average energy of the Boltzmann distribution at the given temperature. The model assumes that once the molecule has relaxed to this level it can not relax to lower vibration levels. Thus the second term is the product of the probability that the molecule

will fluoresce and the probability that the molecules will vibrationally decay to that level before undergoing intersystem crossing to the first excited triplet state. The last term is the fluorescence yield for the thermalized level.

In the model, the fluorescence rate is assumed to be constant, which Lee and Lewis have suggested to be true for most carbonyl compounds.[41] The collision rate is modeled with a Lennard-Jones collision frequency equation given by:

$$Z_{coll} = \pi\sigma_{A-M}^2 \sqrt{8RT/\pi\mu_{A-M}}\,\Omega_{A-M} \qquad \text{Eqn 2.13}$$

where

$$\Omega_{A-M} = \left[0.636 + 0.567\log(kT/\varepsilon_{A-M})\right]^{-1} \qquad \text{Eqn 2.14}$$

Here σ_{A-M} is the collision diameter, μ_{A_M} is the reduced mass of the acetone and the other molecule, $\Omega_{A\text{-}M}$ is sthe collision integral, and $\varepsilon_{A\text{-}M}$ is the Lennard-Jones energy potential.

The intersystem crossing rate is modeled with a double exponential expression that is dependent upon the energy of the vibrational levels, E.

$$k_{NR} = -3.82\times10^9 + 8.82\times10^5 \exp\left(E/1650\right) + 4.08\times10^9 \exp\left(E/77300\right) \qquad \text{Eqn 2.15}$$

The expression is an empirical fit of the intersystem crossing rate calculated from low-pressures fluorescence lifetime data using Eqn 2.8. Here it is assumed that for low pressure where the collision rates is small compare to the intersystem crossing rate, there will be little to no vibration relaxation within the lifetime of the fluorescence. Thus the intersystem crossing rate is from the averaged initially-pumped level in the excited singlet

state that the acetone molecule can reach. The model does not directly address acetone vapor phosphorescence, since it is quickly quenched when mixed with air.

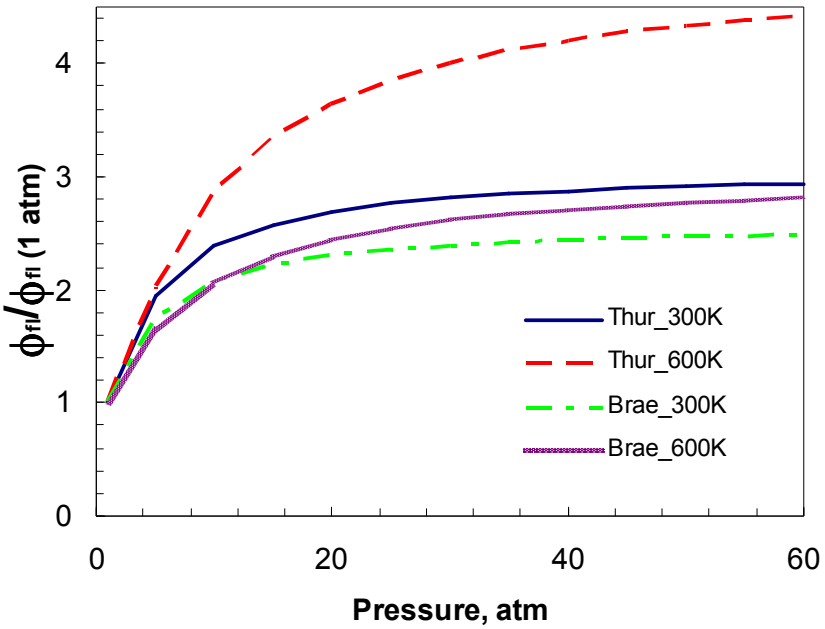

Figure 2.9: Fluorescence yield model results as a function of pressure at 248 nm excitation wavelength for both models at two temperatures.

The model created by Thurber assumes that the acetone concentration is low compared to the other molecules present, i.e., no acetone-acetone "collisional" interactions are included. Also, the model is simplified so that an average molecule rather than a density distribution of molecules is used in the model. The collision process is simplified into a downward cascade of energy through which the molecules moves downward in vibrational energy with each collision. Thus, the collisions between molecules that maintain the energy distribution through the downward and upward transitions between the vibrational energy levels are not exactly modeled.

Example results for the two fluorescence yield models are shown in Figure 2.9 for 248 nm excitation and in Figure 2.10 for 308 nm excitation. The fluorescence yield is normalized to the fluorescence yield at 1 atm for the given temperature, in order to better demonstrate the differences between the two models. At 248 nm, the original Thurber model exhibits a much higher pressure dependence compare to Braeuer model, especially at higher temperatures. For example, the normalized fluorescence yield at 600 K and 60 atm for Thurber model is almost double that of the Braeuer model. The Thurber model has a lower effective intersystem crossing rate for hot vibrational energy levels, thus less molecules transition to the triplet state and the fluorescence increases. Higher pressure exacerbates this difference, since at elevated pressure the vibrational relaxation rates is faster which allows more molecules to reach lower vibrational energy levels, thus reducing intersystem crossing rate. At longer excitation wavelengths, the difference between the two models decreases, as seen in Figure 2.10. The changes made to the intersystem crossing rate only affect it at high vibrational energy levels, which longer excitation wavelengths cannot produce. Thus the two models are essentially the same at longer excitation wavelengths.

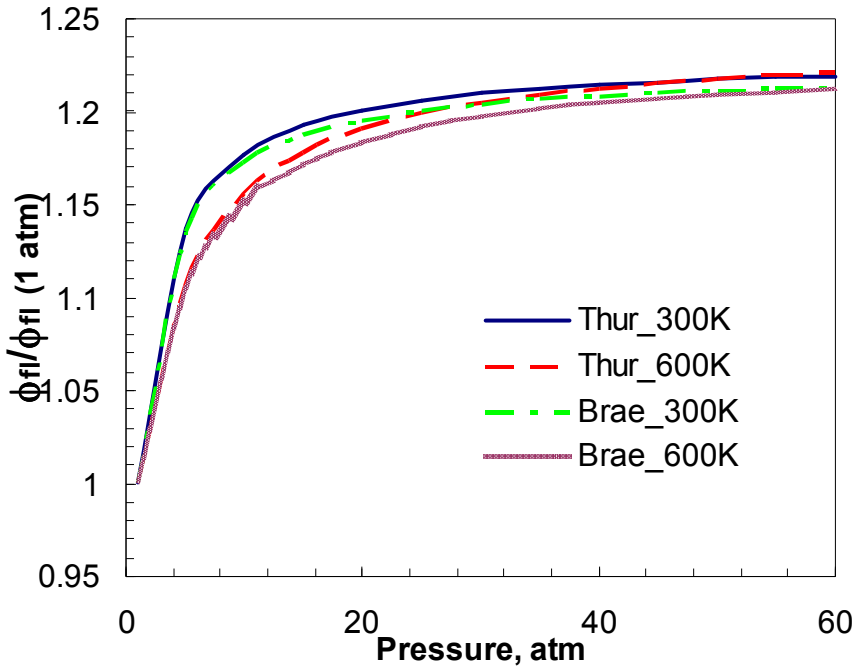

Figure 2.10: Fluorescence yield model as a function of pressure for 308 nm excitation wavelength for both models at two temperatures.

The fractional deviation in fluorescence yield between the two models is shown in Figure 2.11 for different excitation wavelengths and temperatures as a function of pressure. The deviation between the two models is highest for the combination of short excitation wavelength, low pressure and high temperature. For longer wavelengths, the difference between the models is greatly reduced, for example, to less than one percent at 308 nm for all temperatures and pressures. The change in the collision rate through modification of the polarity parameter and the density of the bath gas is minimal, less than 5% at high pressure and temperature. Thus thee primary difference between the two models is the intersystem crossing rates. The Thurber model for the intersystem crossing rate was based on experimental rate for vibrational energies up to 8000 cm^{-1}. Thus it was not able to better predict the intersystem crossing rate for higher energy levels, which are

accessible for laser excitation at 248 nm. For the wavelength used in the current study (266 nm), the difference between the models is: 1) only 2-3% for pressures above 30 atm, and 2) independent of temperature.

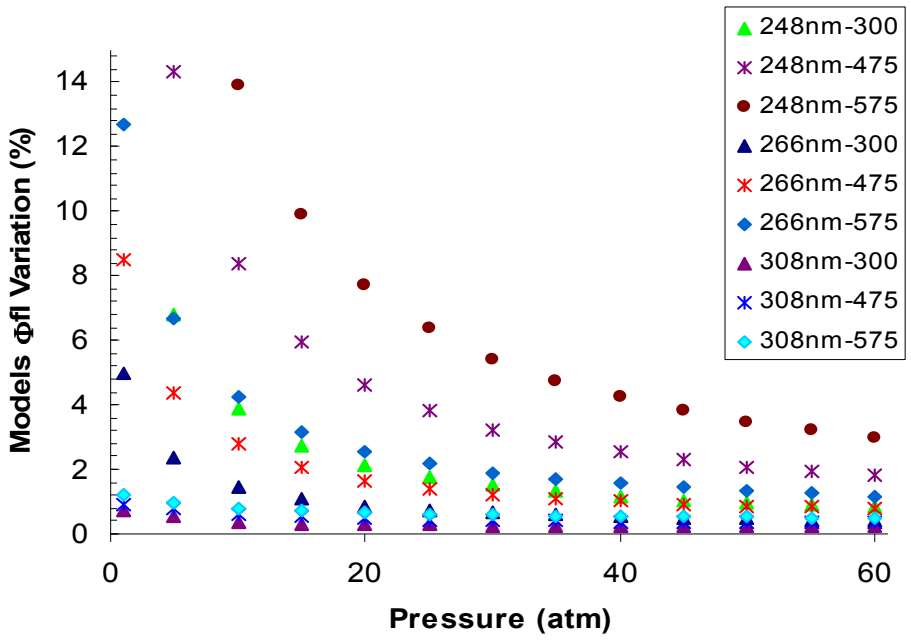

Figure 2.11: Fractional variation in ϕ_{fl} between the Thurber and Braeuer models for three excitation wavelengths and three temperatures for varying pressures.

2.4. INTERFACE MEASUREMENTS TECHNIQUE

The ability to detect the location of the interface of supercritical/liquid is of considerable importance in one aspect of determining the effect of supercritical fluids on the mixing process in supercritical system. Thus, a technique is needed that will provide the mixing characteristic of fluids in a supercritical environment as well as determine the location of the subcritical/supercritical interface. The method proposed here uses the phosphorescence emission from liquid acetone to determine the location of the interface.

Phosphorescence emission of vapor acetone is known to be quenched in the presence of even minute concentration oxygen. However, for liquid acetone, the effect of oxygen on the phosphorescence is diffusion limited. The rate of oxygen molecules diffusing into the liquid is much smaller than the rate of it diffusing into another vapor. Therefore, it takes a longer time for the oxygen to fully quench the phosphorescence signal in liquid. So for a high density (liquid) acetone jet being injected into a hotter gas containing even small amounts of O_2, the "gaseous" acetone phosphorescence will be quenched, while emission from the liquid acetone (without oxygen) will not. As the "liquid" acetone change from subcritical to transcritical/supercritical conditions, its diffusivity will increase. This allows the oxygen to rapidly diffuse into the liquid jet from the surrounding fluid, as compared to the "liquid" is at subcritical condition. Thus, the oxygen concentration will be higher in the supercritical fluid regions of the jet than within the subcritical region. Therefore, the location where the phosphorescence signal is quenched will mark the more diffusive, supercritical fluid and the location with phosphorescence signal will be that of the less diffusion, subcritical fluid. As a result of this diffusion-limited phenomenon, the interface can be discerned from the liquid phosphorescence emission.

This method is visualized in Figure 2.12. The first image of the first row shows the fluorescence signal of both the vapor and liquid acetone in an oxygenated environment. The fluorescence signal from the acetone vapor is used to determine the mixture fraction within flow facility. The fluorescence from the liquid can be used to determine the mass of any droplets that broke off from the main jet. The first image in the second row shows the resulting phosphorescence intensity in the same subcritical environment. Here, the vapor phosphorescence is not visible while the liquid jet and droplets breaking off from

the jet is visible, since the oxygen diffusion is so slow. The second set of image on the second column shows what happen when a subcritical jet (supercritical pressure, subcritical temperature) is injected into a supercritical environment. The supercritical fluorescence image is similar to the subcritical image, while the phosphorescence image is different compare to the subcritical image. The phosphorescence image does not show the droplets as did before. In addition, the area where there is phosphorescence signal in the liquid jet is smaller. This is due to the oxygen diffusing into the regions of the jet raise its temperature high enough to transition into supercritical fluid. Thus, no signal is seen in those regions and we see a smaller size jet. The edge of the phosphorescence signal is considered to be the location of the subcritical/supercritical interface.

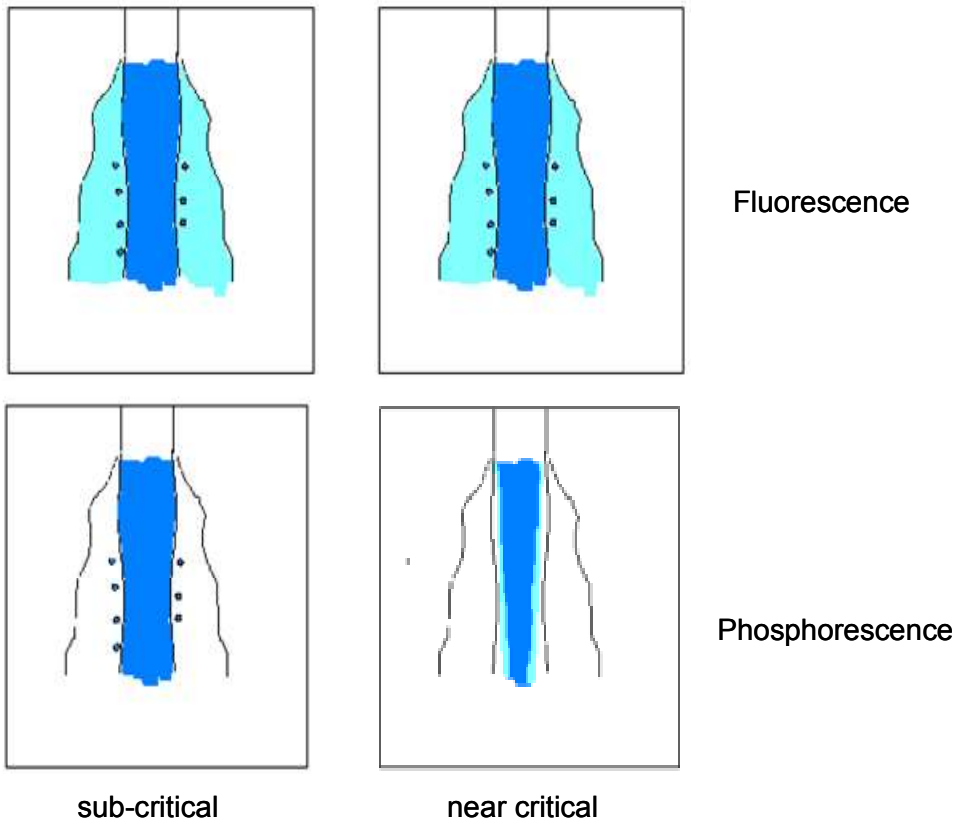

Figure 2.12: Schematic of experimental technique to determine the interface.

The phosphorescence and fluorescence emissions begin simultaneously, however the phosphorescence has a longer lifetime. Thus a time shift in the starting of the image is a possible method to differentiate between the two signals. Another method is to use the difference in the spectra. As mention earlier in the chapter the phosphorescence signal as a slightly red-shifted spectrum compare to fluorescence. It is possible that the intensity of the red-shifting will increase with change in excitation wavelengths, thus the two emission signal can be discerned via their emission spectra. Therefore, further investigation should be done to determine which method will capture the higher phosphorescence signal.

CHAPTER 3

EXPERIMENTAL TECHNIQUE AND SETUP

This chapter details the experimental approaches used to determine acetone's photophysical properties under a wide range of conditions and to demonstrate acetone PLIFP for mixing and transition interface measurements in a jet flow. It includes the experimental setup, instrumentation, and facilities used. The acetone photophysics experiments were performed in a facility in the Ben T. Zinn Combustion Laboratory at Georgia Tech, while the demonstration experiments employed a separate facility located at the University of Florida. The first two sections of this chapter describe the different flow facilities. The third section describes the common optical instrumentation used in both setups. The chapter concludes with descriptions of experimental procedures, and image processing and data analysis methods.

3.1 ACETONE PHOTOPHYSICS SETUP

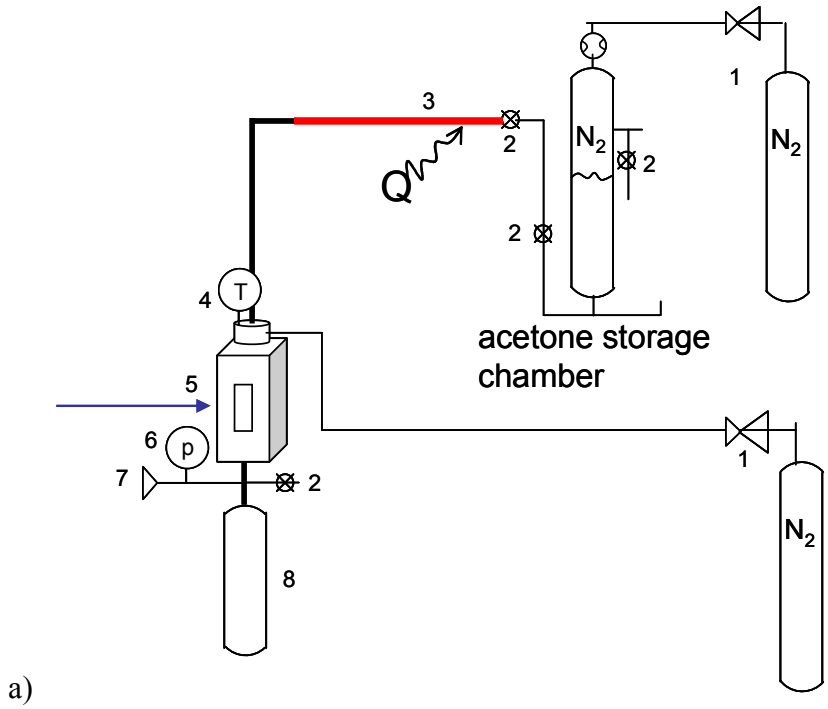

a)

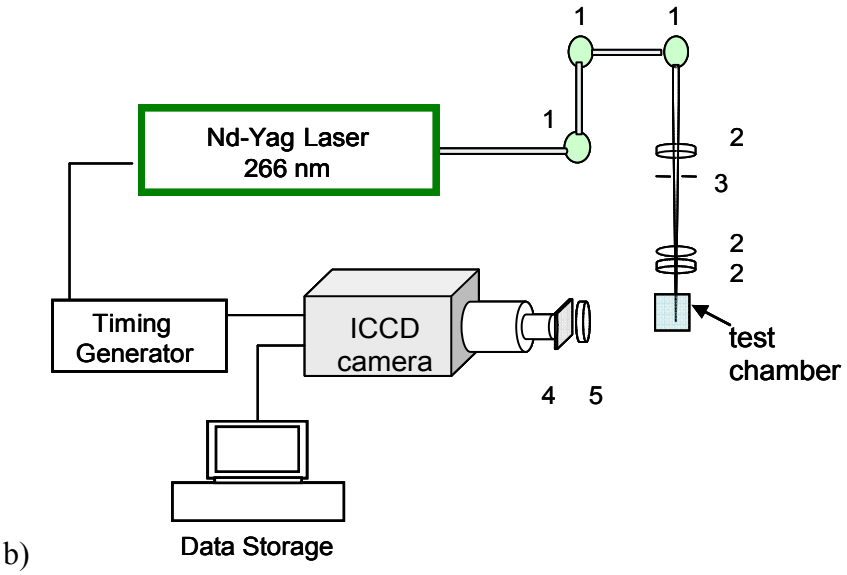

b)

Figure 3.1: Experimental setup for acquiring vapor and liquid acetone PLIFP imaging. a) supply system. 1 – pressure regulator, 2 – needle valve, 3 – heating elements, 4 – thermocouple, 5 – test section, 6 – pressure gauge, 7 – relief valve, 8 – excess liquid settling chamber. b) imaging system. 1 – 266 nm dichroic mirror, 2 – cylindrical lense, 3 – knife edge, 4 – WG 305 filter, 5 – 532 nm filter

The photophysics setup is used to measure the fluorescence and phosphorescence properties of acetone at various temperatures and pressures (see Figure 3.1). The setup has three variations. The first variation is for measurement of acetone vapor and supercritical fluid. It consists of a pressurized cylinder in which a gas is bubbled through acetone to create a diluted vapor acetone stream. The stream can be heated before entering the high-pressure test chamber. The second variation is for liquid photophysics measurements at elevated pressures and temperature. This variation is similar to the vapor system except without the bubbler system, but with the pressurized liquid fed to the heater and test chamber. Room temperature and pressure photophysics is measured using the third variation of the setup. This variation is used for measurements of the emission spectrum of both the vapor and liquid, with higher attention to the liquid phosphorescence emission. In this setup the liquid is not heated and it exits into ambient atmosphere instead of a pressurized chamber. In all three cases, the camera is placed at right angles to the direction of the laser propagation. Any remnant of the laser's energy after it exits the test chamber or liquid jet enters a beam dump to minimize reflections. The subsequent subsections describe different parts of the setup, and further detail the difference between the different setups.

3.1.1 Storage Chamber

Liquid acetone is held in a stainless steel storage chamber with top and bottom openings. The chamber holds up to four liters of fluid. The system is set up so the chambers can be pressurized by nitrogen from either the top or bottom opening. For the liquid studies, the acetone is pressurized from the top opening and exits through the

bottom opening. For the vapor/supercritical setup, nitrogen enters from the bottom to create the acetone-nitrogen mixture, which exits through the top opening. Multiple ball valves between the storage chamber and the stainless steel tube leading to the test chamber assure the correct mixture enters the test chamber at the conditions required and as a safety mechanism to prevent over-pressurization of the test chamber.

3.1.2 Heater Unit

This subsystem heats the liquid acetone or vapor acetone-nitrogen mixture before injection into the test chamber. It consists of four Omega ultra-high temperature heating tapes and a Proportional Integral and Derivative (PID) controller (WATLOW SD series). The heating tapes are insulated and rated up to 1000 K, which is higher than the temperature needed in these experiments. The four heating elements are electrically connected in series and placed sequentially with the capability to provide 624 W. Neglecting losses, this would permit heating the liquid acetone to about 650 K for the flow rates considered. The elements are coiled around a 0.95 cm diameter stainless steel tube, extending ~1 m in length. The heating elements are wrapped in alumina silica ceramic fiber insulation to reduce the heat losses. The controller uses feedback from a thermocouple placed at the top of the test section. The thermocouple is located 4.0 and 2.5 cm from the jet exit for the vapor and the liquid setups, respectively. These distances are short enough to reduce the feedback time for the controller, but long enough for the jet to stabilize before exiting. The controller is able to adjust the total power as well as the rate of the power output, and thus it can perform a quick or slow temperature ramp up.

When it reaches the operating temperature, it is able to provide a constant temperature to within ± 0.3 K.

3.1.3 Laser Excitation Source

Acetone is primarily excited with a Continuum Powerlite 8000 frequency-quadrupled Nd:YAG laser (266 nm) with a 7mm circular exit beam. The unfocused laser beam passes through three dichroic mirrors (see Figure 3.1) to reduce the residual 532 nm (frequency-doubled) light reaching the chamber. After the mirrors, the beam goes through a set of collimating optics to create a collimated beam of variable width, which is adjusted depending on the experimental requirements. For the vapor/supercritical setup, the laser beam goes through two cylindrical lenses with the focal length of 350 mm and 750 mm creating a 7×14 mm^2 beam. The beam then passes through a slit to produce the final beam, ~2.4 mm wide by 14 mm tall. For the liquid setup, the laser beam goes through three cylindrical lenses with focal lengths 40, 350 and 750 cm. The result is a laser sheet 3.8 cm tall and 200 μm thick at the focus of the optics. Before the beam reaches the second lenses, it first passes through a 5×5 mm^2 slit to reduce the excess 532 nm light and to remove the edges of the laser beam in order to create an output more uniform in intensity. The laser pulses at 10 Hz and is triggered by a DG-325 pulse generator. The laser output power used ranges from approximately 7 to 25 mJ per pulse, which is measured directly before the laser enters the test chamber.

For certain studies, a Lambda Physik tunable dye laser system is also used as an excitation source. The dye laser is pumped by the second harmonic output (532 nm) of a Spectra Physics Quanta-Ray Pro-250 Nd:YAG laser. The ~570 nm output of the dye laser

is frequency-doubled with a harmonic generator (Inrad Autotracker) to produce an output wavelength of 285 nm. The output beam passes through three dichroic mirrors to reduce the residual 570 nm light before reaching the collimating cylindrical lenses used to produce the same size beams as in the 266 nm case. The maximum power used in these experiments does not exceed 8 mJ/pulse (with the maximum power limited by the capability of the laser system).

3.1.4 Collection Optics

In the vapor/supercritical setup, the fluorescence signal is collected with a Nikon Micro 55 mm focal length camera lens with a Nikon 35 mm spacer and a Nikon 2X teleconverter. The signal is then imaged onto an electronically cooled ICCD camera (Princeton Instruments PIMAX with Gen III intensifier and 512×512 pixels). With the lenses employed here, the overall magnification is nearly two, resulting in a camera resolution of 48 to 52 μm/pixel. A long-pass Schott glass filter and a holographic notch filter placed in front of the lens minimize light with wavelengths shorter than ~305 nm and from the residual 532 nm laser light. Images are taken with a 150 ns gate starting 50 ns ahead of the laser pulse, so the effective gate time is 100 ns. The camera is synchronized to the laser pulse using the same DG-325 signal used to trigger the laser. At each data point, two sets of images are acquired. The first set consists of three accumulated images, with each the sum of 100 instantaneous images. The second set has consists of 300 instantaneous images (stored in three files). The accumulated images provide an average result while minimizing computer storage memory requirements,

while the instantaneous images are used to determine the shot-to-shot fluctuations in the signal.

For the liquid setup, the fluorescence and phosphorescence signals are collected by a UV-Nikkor (105 mm) lens and imaged onto an electronically cooled ICCD (Princeton Instruments PIMAX with Gen II intensifier and 256×1024 pixels). The imaging system produces a resolution of 30 μm/pixel. Images are recorded using only a portion of the CCD chip, the center 256×400 pixels. This reduces irising effects associated with the slower gating Gen II intensifier, which has a 50 ns delay between the time the center and edge of the intensifier respond to the gate control pulse. Similar to the vapor setup, Schott glass and holographic notch filters are placed in front of the lens, and the same DG 535 is used to synchronize the laser and camera. Images are acquired with exposure times ranging from 200 ns to 600 μs and with time delays of 50 ns before the laser pulse for the fluorescence data to 300 ns afterward for the phosphorescence data. Accumulated images (over 100 laser shots) are recorded to reduce influence of shot-to-shot variations in laser energy and scattering background. The tests were repeated at different times and days to test consistency and repeatability of the experimental conditions. This system was also used for the free jet measurements. In addition, in order to cross-calibrate the two cameras used in the liquid and vapor setups, another vapor data set was taken with the same vapor optics and camera lens, but with the camera from the liquid system instead.

For the emission spectrum studies, the PIMAX 256×1024 ICCD was connected to the exit of an Acton SP-300i spectrometer operating with a 300 grooves/mm grating. Four bundles of optical fibers provide the input at the entrance slit of the spectrometer. Two of the fiber bundles were used to acquire the laser-induced emission signal from the acetone

jet. The entrance slit was set to approximately 500 μm, which was found to be sufficiently large to provide ample signal but small enough to provide suitable spectral resolution. The spectrometer has three selectable grating; the grating with a 250 nm range was employed here, with the grating rotated to produce a 425±125 nm spectrum. The same Schott glass filter employed in the other experiments was placed in front of the optical fiber to reduce the ultraviolet laser light scattering signals. Excess light from scattered 532 nm residual laser light is subtracted from the emission spectrum during post processing. The spectrum taken at each test condition is an accumulation of 300 laser shots. Since the whole intensifier chip was used to measure the spectrum, the minimum intensifier gate width used was 300 ns due to the slow time response (~100 ns) of the 25mm Gen II intensifier.

3.1.5 Test Chamber

The majority of the photophysics measurements for the acetone laser-induced fluorescence and phosphorescence are performed in the high pressure (and temperature) chamber shown in Figure 3.2. The chamber is made of a 5×5×20 cm^3 stainless steel block with a hollow cylindrical chamber 3.8 cm in diameter and 20 cm in length. Each side of the chamber has a 1.25×5 cm^2 opening in which a quart window can be placed for optical access. The quartz windows are made of high quality UV grade quartz that can transmit 96% of the laser power for wavelength down to 200 nm. The windows are 1.6 cm thick to be able to withstand the pressure and temperature necessary for the experiments. The test chamber was hydraulically tested at room temperature for pressures up to 150 atm, twice the maximum required operating pressure.

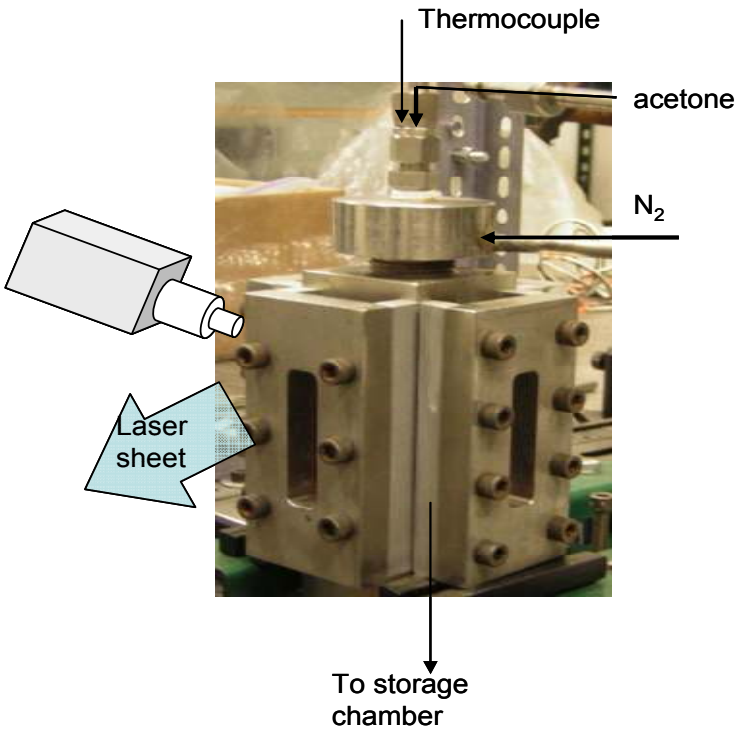

Figure 3.2: Photograph of high pressure test chamber.

The top of the chamber has three openings, two near the center and one to the side. Nitrogen is injected into the side opening to pressurize the chamber. A thermocouple enters through one of the top entrances is inserted to 5 cm from the test location to measure the temperature of the fluid before entering the test cell. The test fluid (liquid or vapor/supercritical mixture) is injected in the second central opening, which is turned at 90°, to flow through the test chamber. The pressurization N_2 and test fluid exit through the bottom of the chamber (see Figure 3.2).

At the bottom exit of the chamber, the diameter reduces from 3.8 to 1.6 cm. The fluid exiting the bottom of the test chamber can exit two ways. The first path is directly downward to a high pressure settling chamber. The settling chamber is the same four liter stainless steel container used as a liquid acetone supply container and which is described

above. A ball valve attached to the bottom of the container allows collected liquid acetone to be drained at the end of each test run. The second path is at a right angle to the flow, and it leads to an electronically controlled needle valve that regulates the flow and thus pressure within the test chamber. Another right angle connection leads to a pressure gauge that monitors the chamber pressure. Ahead of the pressure gauge is a spring lock relief valve used to prevent over-pressurization of the test chamber. On two sides of the chamber, externally plexiglass shields are placed to protect against flying debris in the event of a window rupture. The test chamber can be modified to operate with vapor or liquid acetone. The next two subsections describe changes in the system for the vapor and liquid setups.

3.1.6 Vapor Photophysics Setup

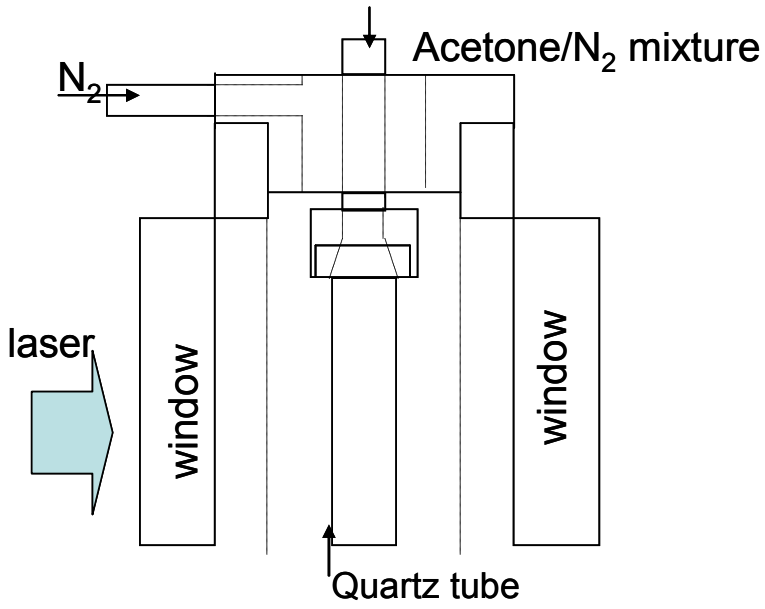

Figure 3.3: Vapor/supercritical fluid photophysics setup details.

In the vapor/supercritical case, the injected fluid is a mixture of gaseous acetone and nitrogen. The mixture enters the chamber through a.5 mm inner diameter stainless steel tube. The tube expands to 9 mm, with the expanded section of the tube attached to one end of a stainless steel bracket. The other end of the bracket is used to hold a quartz tube, which is has 8×8 mm^2 square cross-section with a 1.5 mm thickness. The square tube is attached to a 1.5 cm circular flange that is used to hold the quartz tube to the bracket. There are two reasons why the injected fluid enters through the quartz tube instead of letting it flow directly into the test chamber. The first purpose is to maintain a uniform, constant concentration within the test region. The second purpose is to minimize the temperature variation within the test region. Quartz is a poor conductor, thus conduction of thermal energy from the acetone within the quartz tube to the cooler gas mixture outside is minimal. This should also allow the temperature measured upstream of the test section, approximately 4 cm, to be nearly equal to the actual temperature in the test region.

To test this assumption, an atmospheric pressure test was conducted to determine the temperature variation from the top to the bottom of the test cell. In the test, an additional thermocouple was placed at the exit of the test cell. Measurements were performed with and without nitrogen co-flow, since the co-flow is not heated, and over a period of two days for repeatability. Figure 3.4 shows the results of the experiment. The temperature difference between the top and exit of the test cell is minimal. The few data points showing a significant deviation occur when one of the thermocouple touched the chamber wall (data within circle 1 for top thermocouple and data within circle 2 for bottom thermocouple), thus causing the higher temperature difference. Excluding these points,

the highest temperature difference seen in the test case was 8° C, occurring in the 250-300 °C range. This is quite small, ~1% of the absolute temperature. In addition the exit temperature measurements are 12.7 cm from the top thermocouple normally used to monitor the acetone temperature, while the fluorescence measurements occur 9 cm downstream of that thermocouple. Thus the temperature error in the photophysics study should be even less. Therefore, the assumption that the temperature is constant within the quartz tube is reasonable.

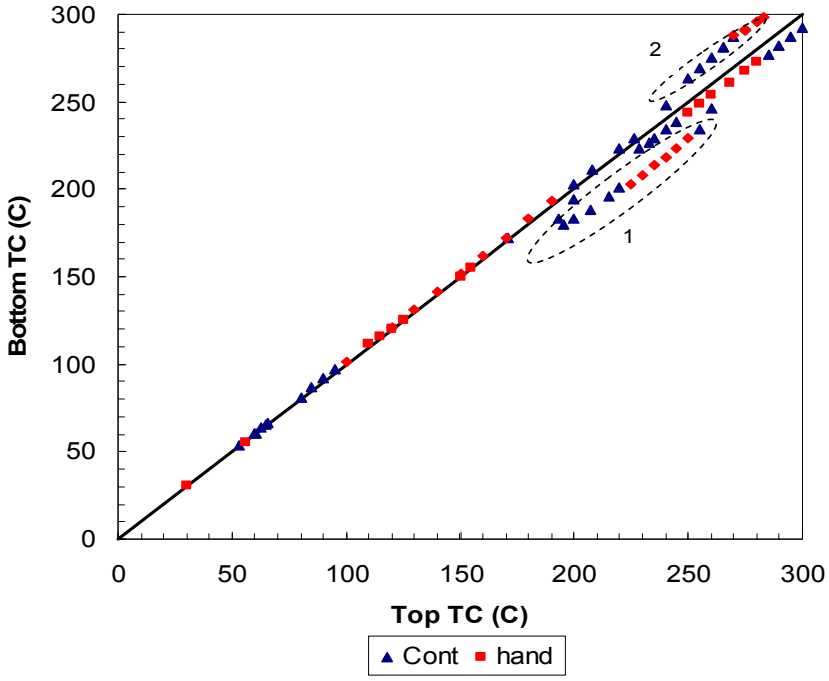

Figure 3.4: Temperature difference between the top of the test cell and the exit of the test cell, approximately 15 cm apart. Straight line represents the 1:1 ratio, and results are shown with two different thermocouple readers (one in the temperature controller and the other hand held).

The acetone vapor mixture is created by placing a bubbling system within the storage chamber. Nitrogen gas injected through small holes produce multiples bubbles that

disperse within the liquid acetone. As the bubbles travel upward, acetone evaporates and slowly builds up within the N_2 bubbles. By the time they reach the top of the steel chamber, the acetone concentration within these bubbles should approach the saturation vapor pressure for the fluid at the storage chamber temperature. The bubble generation system is made of a 0.635 cm diameter stainless steel tube. A stainless steel sintered plate with 40 μm holes is placed at the end of the steel tube creates the nitrogen bubbles. In addition to the sintered plate, two 0.3125 mm holes are drilled 180° apart at 2.54 cm and at 3.75 cm above the end of the tube (see Figure 3.5). The combination of the sintered plate and holes ensures enough bubbles are created to produce saturated conditions at room temperature ($p_{acetone}$~ 0.3 atm) and for the flow rates needed,.

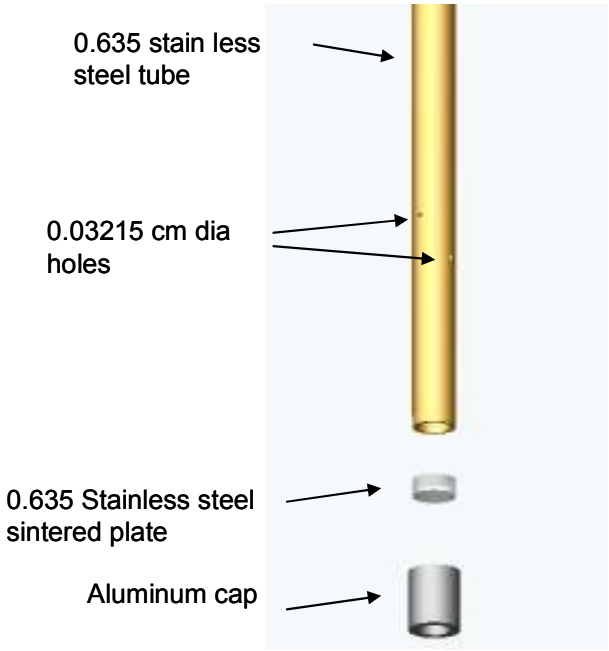

Figure 3.5: Bubbler system.

3.1.7 Liquid Photophysics Setup

In the liquid injection setup, the bubbler is removed from the storage chamber since there is no need to create an acetone-nitrogen vapor mixture. The liquid acetone goes through multiples nitrogen pressurization-depressurization cycles to reduce the oxygen concentration within the liquid acetone. This is done by injecting the nitrogen through the bottom opening of the storage chamber. The high pressure nitrogen displaces oxygen dissolved in the acetone, and when the pressure is reduced a portion of the dissolved gases is released. Repeating this process increases its effectiveness in reducing the dissolved oxygen concentration. This pressurization-depressurization process usually is performed for at least 24 hours.

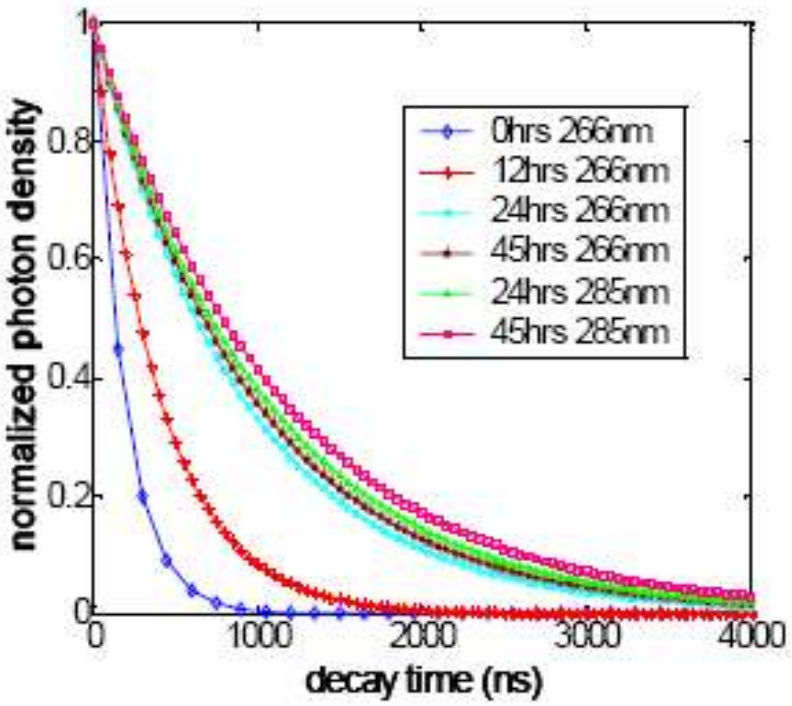

Figure 3.6: Normalized phosphorescence signal versus time for various nitrogen pressurization-depressurization time and wavelength.

A test was conducted to determine how long should the process be done for most of the oxygen to be extracted from the liquid acetone. For each test conditions, a minimum of 4 pressurization-depressurization cycles are done within the time frame. Figure 3.6 shows the normalized phosphorescence signal versus time for acetone that has undergone numerous nitrogen pressurization-depressurization cycles for various length of time. From the figure, it can be seen that the majority of the oxygen escaped from the liquid acetone after 24 hrs of pressurization and depressurization and continuing the process will not increase the phosphorescence signal.

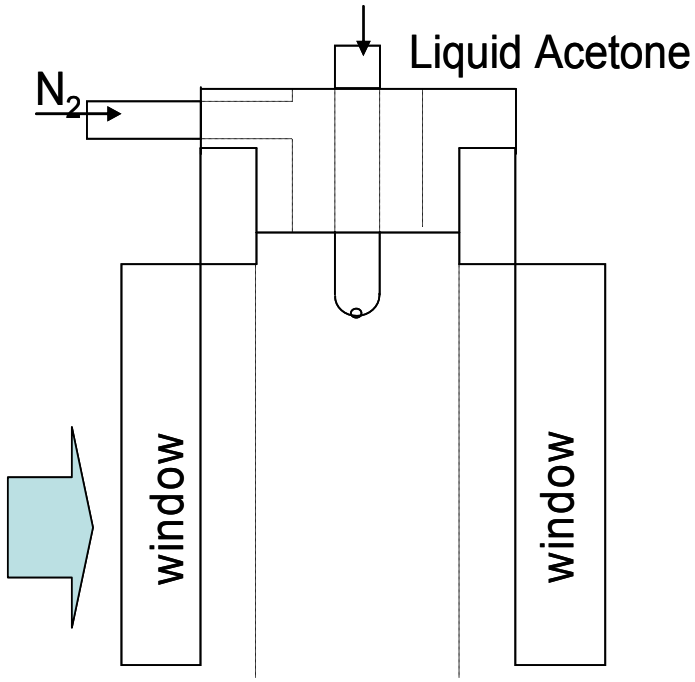

Figure 3.7: Liquid injection setup

The liquid acetone is heated and then enters the test chamber through the same entrance as the acetone-nitrogen vapor mixture. The acetone is injected through a 0.625 cm diameter stainless steel tube with a 300 μm hole at the end. Typically, the liquid

acetone velocity is very slow, approximately 1 m/s or less, in order to create a laminar flow. A laminar jet was seen to provide a more consistent, repeatable test condition compared to a turbulent flow. A nitrogen co-flow is used to reduce the acetone vapor within the test chamber, minimizing absorption of the laser energy between the entrance window and the acetone jet. Two electronic needle valves, one before the heater and one after the test chamber, are used to regulate both the vapor and liquid flow rate within the system. As noted previously, the jet exits the test chamber and enters into a storage chamber where the liquid can be drained at a later time.

3.1.8 Liquid Free Jet Setup

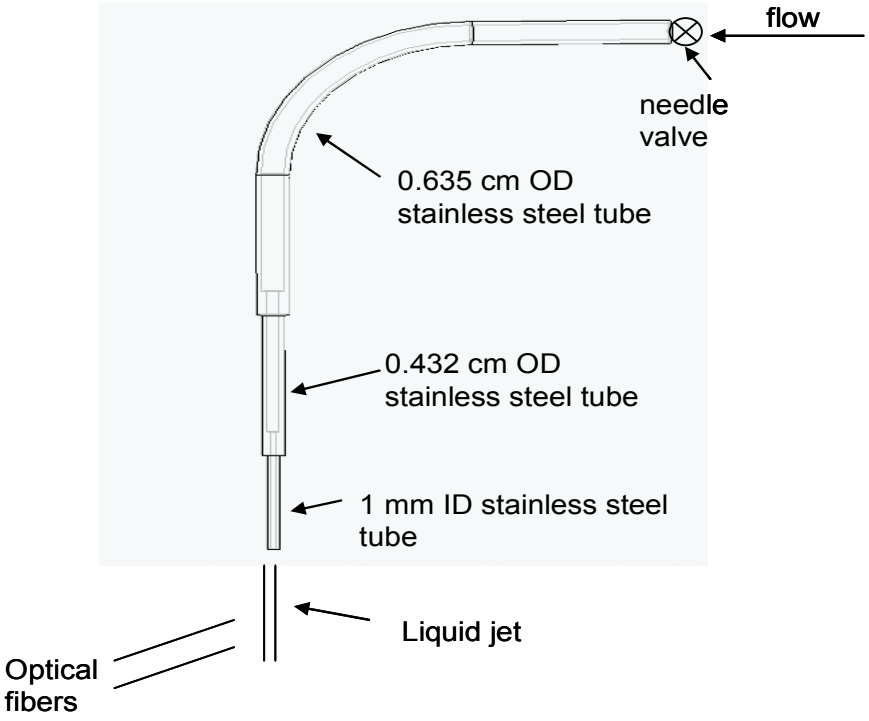

Figure 3.8: Setup to capture the fluorescence and phosphorescence emission spectrum of acetone vapor and liquid.

This setup, which is used to examine the fluorescence and phosphorescence spectra and their variation with time and excitation wavelength, is used at room temperature and pressure. Thus the liquid jet is allowed to exit into the ambient atmosphere. The liquid goes through oxygen purging cycles as described above. After the liquid exits the storage chamber, it enters a 0.635 cm OD tube that is reduced to a 0.432 cm OD tube and then further reduced to a 1 mm ID tube (Figure 3.8). The 1 mm tube is approximately 3 cm long to stabilize the jet and keep it laminar as it exits. A needle valve is used to regulate the flow. Two optical fibers connected to the spectrometer are placed so as to collect light from the same location along the jet.

3.2 UNIVERSITY OF FLORIDA SETUP

The flow facility is a high pressure and temperature chamber created from a 8.13 cm square brass block that is 25 cm long and has a 4.6 cm square inner cross section with rounded corners, and is located at the University of Florida combustion facility (Figure 3.9).[48] The chamber was designed to sustain pressures up to 100 atm and temperature up to 700 K. Four quartz windows, made from the same material as the Georgia Tech facility windows, are placed on the four walls for optical access. The windows are 1.91 cm wide by 8.64 cm long and 2.16 cm thick. The acetone jet exits from a 1 mm orifice that is placed at the central axis of the test cell. Near one of the corners of the test section is an opening for nitrogen or air to enter to pressurize the test cell. Liquid is allowed to exit through a small hole at the end of the test section into a one liter storage container. During the experiments, a gas exhaust system regulates the pressure change and reduces vapor build up within the chamber.

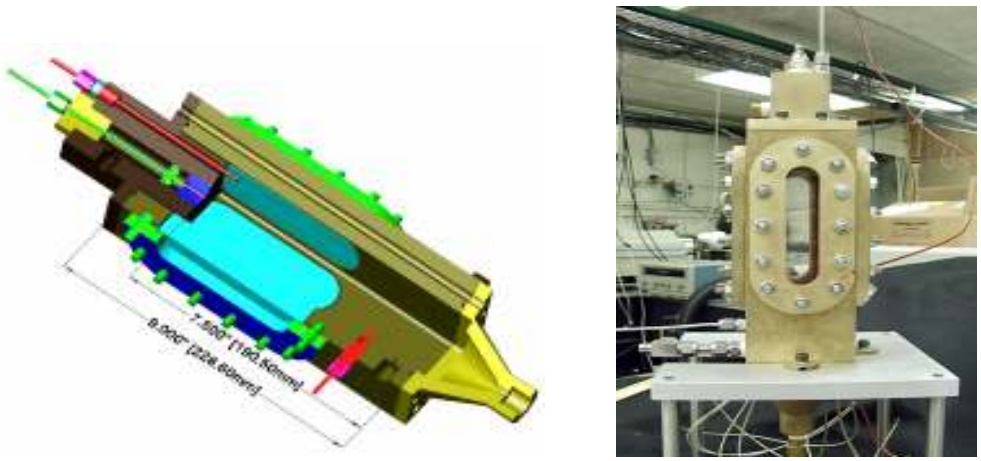

a) b)

Figure 3.9: Univerisity of Florida test chamber. a) Test chamber schematic; b) the assembled overall view.

A schematic of the setup is shown in Figure 3.10. The liquid acetone goes through the same deoxygenation process used in the previous experiments. The storage chamber used is the same employed in the Georgia Tech facility. The pressurization gas, either nitrogen or air, is provided from pressurized tanks. The mass flow rate of both the liquid and gas are controlled by several needle valves and measured by flow meters. After the fluids pass through the flow meters, they enter electric heaters, with both liquid and gas heated. Pressure transducers and thermocouples are placed upstream and within the chamber to keep track of the pressure and temperature.

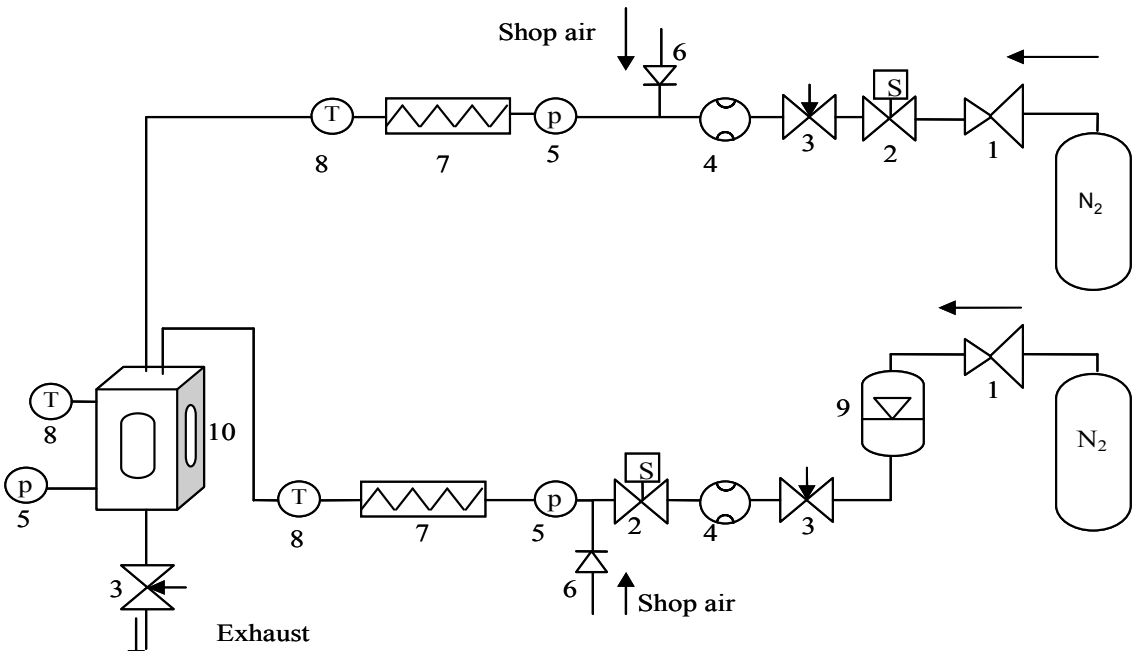

Figure 3.10: Gas/liquid supply system. 1 – pressure regulators, 2 – solenoid valves, 3 – needle valves, 4 – flow meters, 5 – pressure transducers, 6 – check valves, 7 – electrical heaters, 8 – thermocouples, 9 – fuel tank, 10 – high pressure chamber**.**

The excitation source is the frequency quadrupled (266 nm) output of a Quanta-Ray Lab 150-10 laser. The laser passes through the three cylindrical lenses of focal lengths of 40, 350 and 1000 mm to create a laser sheet 45 mm high and 300 μm thick. The average pulse energy used in these experiments is 30 mJ. The acquisition system is changed to include both ICCD cameras described previously. The cameras have identical Nikon Micro 55 mm lenses, with 35 mm spacers and 2X teleconverters. The resulting resolution is 28 μm/pixel for both cameras, close to 1:1 magnification. The two cameras image the same region of the test chamber through a beam splitter. Emission at a right angle to the laser path strikes the beam splitter, which directs 45% of the light to the fluorescence camera and 55% to the phosphorescence camera. A WG 305 glass filter and a holographic notch filter are placed in front of the fluorescence camera to reject scattering

of the ultraviolet and residual green laser light. The gate width for the fluorescence camera is set to 40 ns, with the gate beginning simultaneous to the laser pulse. For each condition there are 100 images taken, with 300 ms between images. The phosphorescence gate width is set to 20 μs with a 200 ns delay after the laser pulse to exclude the fluorescence signal. No filters are required for the phosphorescence camera since the signal is measured after the laser pulse.

3.3 IMAGE PROCESSING AND SIGNAL CORRECTION

The images of the acetone fluorescence and phosphorescence, as well as the spectra, need to be corrected in order to produce quantitative results. First, background signals need to be subtracted from the images. This includes the dark background associated with the camera electronics, the ambient light from the room, and scattered light from the laser. The total signal in each image is a summation of the background signal and the fluorescence signal, as seen in Eqn 3. 1

$$S_{tot}(x,y,t) = S_{fl}(x,y,t) + S_{bg}(x,y,t) \qquad \text{Eqn 3. 1}$$

Background images are acquired at the beginning and the end of each experimental set to test for consistency of the background. Generally, the average of the two backgrounds is used.

Second, the energy variations in the laser sheet profile needs to be corrected. Also, the variation in the quantum efficiency of each pixel has to be considered. The sheet energy variations are corrected by obtaining images of a uniform (and low) concentration of acetone vapor within the test chamber. For low concentrations, the energy absorption

across the field of view is minimal, and the intensity can be correlated to the laser profile. Figure 3.11 shows the energy profile for the laser sheet. At the edges of the beam, there is a sharp decrease in the intensity. In most of the experiments, only a portion of the beam, 40% (boxed region in Figure 3.11), is used. This region near the center of the sheet has the least energy variation.

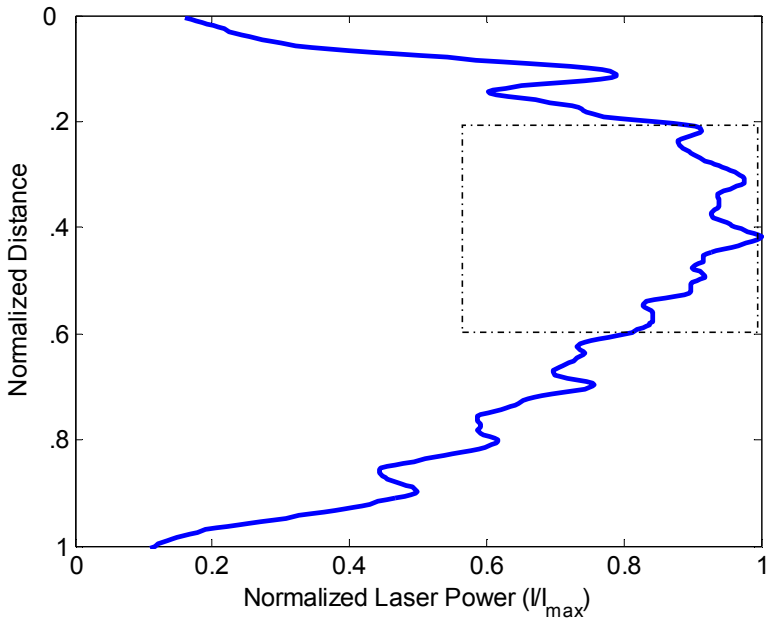

Figure 3.11: Laser energy profile of laser beam. The square depicts the location used for the quantitative calculations.

For the fluorescence yield experiments, the fluorescence yield related to the measured signal according to:

$$\phi_{fl}(T,P) = \frac{S_{tot.fl}(T,P)}{\left(\frac{E_{ave}}{hc/\lambda}\right) * dV * \eta_{optic} * \sigma(T) * n_{ace}} \Rightarrow \frac{S_{tot.fl}(T,P)}{Const_{\exp} * E_{ave} * \sigma(T) * n_{ace}} \qquad \text{Eqn 3.2}$$

Since the laser wavelength, laser volume, and optical collection and detection efficiencies are all experimental parameters, they can be grouped together into one constant in the equation. In order to calculate the fluorescence yield, the total fluorescence signal within a given number of pixels, $S_{tot.fl}(T, P)$, the average laser energy per unit area, E_{ave}, the absorption cross-section, $\sigma(T)$, and the acetone concentration needs to be determined. For all of the vapor fluorescence case, $S_{tot.fl}(T, P)$ is the total fluorescence signal within a 60×100 pixel region, corresponding to a 3×4.95×2.4 mm^3 volume (see Figure 3.12). The area chosen is located at the center of the quartz tube to minimize the effect of the wall reflection and the variation in density near the wall. It is also located at the center of the laser profile to reduce the variation in the laser profile.

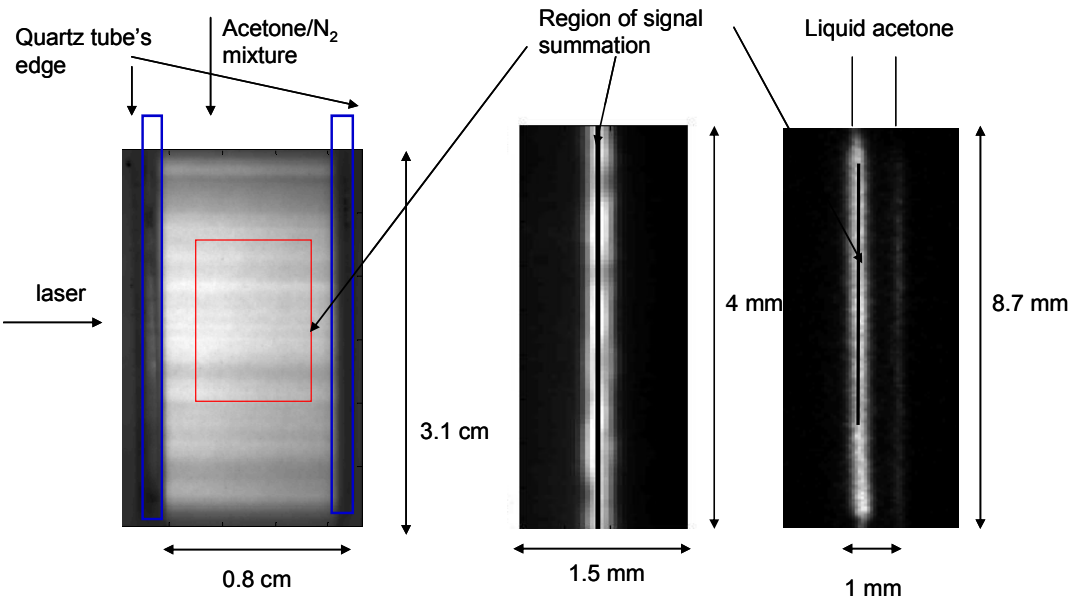

Figure 3.12: Images of a) typical vapor fluorescence and b) liquid fluorescence signal. The region within the red rectangle in a) and the black line in b) correspond to the region of fluorescence signal summation. Liquid phosphorescence signal is summed at the same location.

For the liquid fluorescence and phosphorescence study, the measurement region was a 2×91 pixel, or 0.086×4×0.2 mm^3, with the beginning of the region starting at 2 mm from the jet exit. This is valid for the liquid test cell experiments as well as the atmospheric experiments.

The average laser energy per unit area within the summation region is determined by dividing the total laser energy by the laser cross section area (2.43×14 mm^2 for the vapor experiments and 0.2×38 mm^2 for the liquid experiments). The total laser energy is measured before and after each test run with an Ophir L30A-EX energy meter to obtain the average laser pulse energy. Next, the average laser energy is multiplied by the normalized laser profile to find the laser energy per unit area at each pixel. Lastly, the laser energy per unit area within the summation region is averaged to determine the E_{ave}, i.e.,

$$E/A = \frac{E_{tot}}{A_{laser}} * E_{norm.profile} \qquad \text{Eqn 3.3a}$$

$$E_{ave} = \frac{\sum_{number.of.pixel} \left(E/A\right)}{number.of.pixels} \qquad \text{Eqn 3.3b}$$

The absorption cross-section as a function of temperature for vapor acetone has been previously determined[40] and is plotted in Figure 2.4. In this experiment, it is assumed that the acetone vapor concentration is constant through out the test cell. The acetone concentration is calculated from the absorbed laser energy. Beer's Law relates the laser intensity I at some distance x to its initial value I_o,

$$I(x) = I_o * e^{-n_{ace}*\sigma*x} \quad \text{Eqn 3.4}$$

Manipulating Eqn 3.2 to solve for the laser energy, E_{ave}, and substituting it into Eqn 3.4

$$\frac{S_{fl}(x,T,P)}{C*\phi(T,P)*\sigma(T)*n_{ace}} = \frac{S_{fl}(x_o,T,P)}{C*\phi(T,P)*\sigma(T)*n_{ace}} * e^{-n_{ace}*\sigma*L} \quad \text{Eqn 3.5a}$$

or

$$\ln\left(\frac{S_{fl}(x,T,P)}{S_{fl}(x_o,T,P)}\right) = -n_{ace}*\sigma*L \quad \text{Eqn 3.5b}$$

Plotting the natural log of the fluorescence signal versus distance, *x*, and calculating the best linear fit to the signal, the slope of the linear fit is equal to $n_{ace}\,\sigma$. The location used to determine the slope is the same location used to determine the total signal, except with a longer *x* distance, 100 pixels increased from 60. Slopes from different sections within that location are calculated and averaged. Dividing the slope by the known absorption cross-section will results in the acetone number density. After the acetone number density is known, it can be substituted back into the fluorescence yield equation to calculate the fluorescence yield at the test pressure and temperature. (Note from Eqn 3.5, all that is really required to calculate the fluorescence yield is the product $n_{ace}\sigma$. So any errors in the model for σ are unimportant in the determination of ϕ_{fl}.)

For the liquid acetone experiments, the same method is used to calculate the fluorescence yield and phosphorescence signal, except for a few differences. One, the acetone number density is assumed to be constant and equal to the number density at

room temperature and pressure, 8.14×10^{21} molecules/cm^3. Thus the process used to calculate the number density is not necessary. In addition, the absorption of the laser energy by the acetone vapor before the laser reaches the jet needs to be taken into consideration. At the lower temperatures, the vapor concentration is small enough to be neglected. At higher temperature, however, the average vapor concentration is determined from the averaged image and a new averaged laser energy striking the liquid is calculated according to Beer's Law. Also, at high temperatures and long exposure times, any vapor phosphorescence can influence the liquid phosphorescence signal. The vapor's phosphorescence/fluorescence ratio is 9 and the phosphorescence lifetime can be longer than the liquid's (shown later in Chapter 4). Thus the vapor phosphorescence signal can interfere with the liquid's signal for long delays after the laser in regions where the vapor concentration is high, e.g., close to the jet. To correct for this, an average vapor phosphorescence signal is taken for each exposure time, typically from a few millimeters away from the jet, and subtracted from the total signal from the jet.

For the test cases used to demonstrate the technique and to check its range of operation the number density, mass density, and mixture fraction is calculated as follow. The number density is calculated using Eqn 2.1, solving for the number density. This is done through a marching process from one pixel to the next. At each pixel in the column (the axial distance) it is assume that the number density is not varying within the pixel. At the initial pixel, the laser's energy is the initial energy right after it enters the test section. New laser energy is calculated at for each pixel using Beer's law (Eqn 3.4) and that new laser's energy is used for the next pixel. This accounts for the reduction of laser's energy due to absorption by the acetone molecules. It is assumed that the acetone density, after it

passes through the gas-liquid interface, is equal to the density of liquid acetone at room temperature for liquid below 400 K. As mention earlier, the error in this assumption is less than 10% for liquid temperature up to 400 K. Above 400 K, the Peng-Robinson equation of state is used to determine the acetone liquid density at the liquid temperature and pressure at injection. At any location where there is a droplet, the size and the mass of the droplet needs to be determine and the laser energy needs to be recalculated to account for the laser absorption by the droplet. Since the droplet, in most case, will be smaller than the thickness of the laser beam it will only absorb a portion of the laser energy rather than the entirety of it.

The mixture fraction is defined as:

$$f = \frac{m_{fuel}}{m_{mixture}} \Rightarrow \frac{\rho_{fuel}}{\rho_{mixture}} \Rightarrow \frac{\rho_{fuel}}{\frac{P}{\overline{R}/MW_{mix} TZ_{mix}}} \qquad \text{Eqn 3.6}$$

where:

$$MW_{mix} = xMW_{fuel} + (1-x)MW_{air} \qquad \text{Eqn 3.7}$$

$$x = \frac{n_{fuel}}{n_{mix}} \qquad \text{and} \qquad n_{mix} = \frac{P}{RTZ_{mix}} \qquad \text{Eqn 3.8a, b}$$

$$Z_{mix} = xZ_{fuel} + (1-x)Z_{air} \Rightarrow xZ_{fuel} + (1-x) \qquad \text{Eqn 3.9}$$

Here, x is the fuel mole fraction and MW is the molecular weight of the fuel and air, and Z is the compressibility factor for the fluid. At each pixel, the compressibility factor of

acetone is used as the starting point to determine the number density and the mole fraction. A new Z_{mix} is calculated from the new mole fractions and the process is iterated until a solution is reached. The values are then used to calculate the mixture fraction. Using this method Z_{mix} would be close to 1 at a location far from the jet, since there is a higher percentage of air in that region, and close to the acetone value within the vicinity of the jet.

CHAPTER 4

ACETONE PHOTOPHYSICS

This chapter presents results for the determination of the photophysical properties of acetone from subcritical to supercritical conditions. The first section of the chapter describes the experimental results for the vapor fluorescence yield. The experimental results are compared to the values from the two models described in Chapter 2. The second section deals with the photophysics of liquid acetone, both its fluorescence and phosphorescence emission characteristics.

4.1 VAPOR ACETONE PHOTOPHYSICS

As explained in Chapter 2, the primary uncertain issue related to acetone vapor photophysics is the fluorescence yield, especially at higher pressures and temperatures. To that end, relative fluorescence yields were determined by dividing the measured signals by the laser energy, the concentration, and absorption coefficient determined *in situ* (as indicated by Eq. 2.1). Figure 4.1 shows the measured fluorescence yields as a function of temperature, normalized to the fluorescence yield at 295 K, for various pressures ranging from 1 to 60 atm, corresponding to reduced pressures, p/p_c, of 0.02 to 1.25. For a given pressure, the fluorescence yield decreases nearly linearly with increasing temperature. The decrease in ϕ_{fl} with temperature occurs because the molecules are initially in a higher vibrational energy state when the acetone is at a higher temperature. That is to say the molecules have a larger thermal energy, i.e. the energy difference between the bottom-most energy level and the mean energy level at different

temperature is higher for higher temperature. When the molecules are excited by the laser, they reached higher vibrational energy levels in the first excited singlet state. As noted in Chapter 2, the intersystem crossing rate for a given vibrational energy level is directly proportional to its energy; thus higher temperatures lead to faster intersystem crossing and lower fluorescence yields.

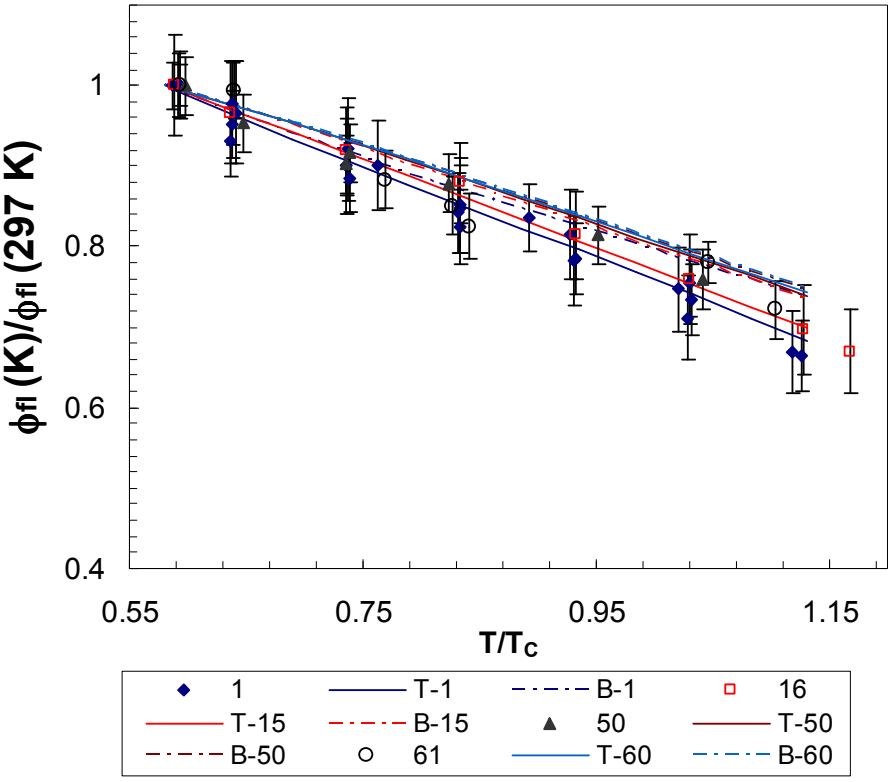

Figure 4.1: Normalized fluorescence yield (ϕ) of vapor acetone at varying pressures and temperatures in nitrogen co-flow. Data normalized to ϕ_{fl} at 295 K for each pressure set. Symbols are experimental data. Solid lines are Thurber's model. Dash lines are Braeuer's model. The legends indicate the pressure in atm.

Figure 4.1 also shows the relative fluorescence yields as given by the models proposed by Thurber and Braeuer. The predictions of the two models differ at lower pressure, but collapse at higher pressures. The experimental data lie closer to the Thurber

model predictions at low pressures. The Thurber model and the experimental data exhibit a higher temperature dependence than the Braeuer model. At higher pressures, the data trend is different from that of both models. The models display a lower temperature dependence at high pressure, while the data continue to show a higher temperature dependence. Also, the data for the different pressures have the same or very similar temperature dependence, with no clear systematic variations for different pressures.

Thus, the results suggest that the effects of temperature and pressure are independent. However, the scatter in the data, due to uncertainties in the laser energy, shot to shot fluctuation and acetone concentration, may be masking a weak trend. The laser is able to provide constant energy with a 5% variation in the laser energy at the energy level chosen, ~ 10mJ/pulse. The shot to shot fluctuation, the variation in the signal from shot to shot, is calculated to be approximately 2% of the total signal. The largest source of uncertainty is from the acetone number density calculation, which is found from the slopes of the least square linear fit of the natural log of the signal with respect to the laser pathlength. The slopes were calculated at different positions within a selected region of the images and this was done for all 100 to 200 instantaneous images and averaged. The variations in the slopes were also calculated. The percent variation of the slopes is typically less than 25%. For cases where there are low acetone concentrations, the variation is higher reaching 40%. Thus, the overall uncertainties are driven by the uncertainty in the slow or $n_{ace}\sigma$. The total percent uncertainty (u) is calculated as:

$$u = \frac{\sqrt{u^2_{laser} + u^2_{shot-to-shot} + u^2_{slope}}}{\sqrt{N}} \qquad \text{Eqn. 4.1a}$$

where N is the number of repetitions at each point. For most of the data shown here, the fluorescence yield or signal is normalized to a reference value. Therefore, the uncertainties from the reference point will also need to be added to the total uncertainty. Thus the uncertainty becomes:

$$u = \frac{\sqrt{u^2_{1.las} + u^2_{1.sts} + u^2_{1.slo} + u^2_{0.las} + u^2_{0.sts} + u^2_{0.slo}}}{\sqrt{N}} \qquad \text{Eqn. 4.1b}$$

The overall uncertainty in the fluorescence yield calculation is no more than 10%. For the temperature range tested, the experimental fluorescence yield decreases by approximately 33%, while the theoretical results range from 28% to 35%, with the lower value at the higher pressure condition. Overall, the difference between the experimental and model results is small, within 7%, depending on the operating pressure and temperature.

The fluorescence yield can be used to determine the fluorescence intensity signal emitted per acetone molecule. Manipulating Eq. 2.1, the fluorescence intensity signal per acetone molecule can be written as shown in Eqn. 4.2. The fluorescence intensity signal per acetone molecule is dependent upon the laser energy fluence, the control volume, and the optical efficiency, which are experimental factors and that are usually constant for an experimental setup. Thus they can be grouped into one constant, *C*, as shown in Eqn 4.3. If the fluorescence is normalized to its value at one condition, the result is simply the product of the fluorescence yield and absorption coefficient.

$$S/n_{ace}(T,P) = \left(\frac{E}{hc/\lambda}\right) dV \cdot \eta_{optic} \cdot \sigma(T) \cdot \phi(T,P) \qquad \text{Eqn. 4.2}$$

$$S/n_{ace}(T,P) = C \cdot \sigma(T) \cdot \phi(T) \qquad \text{Eqn. 4.3}$$

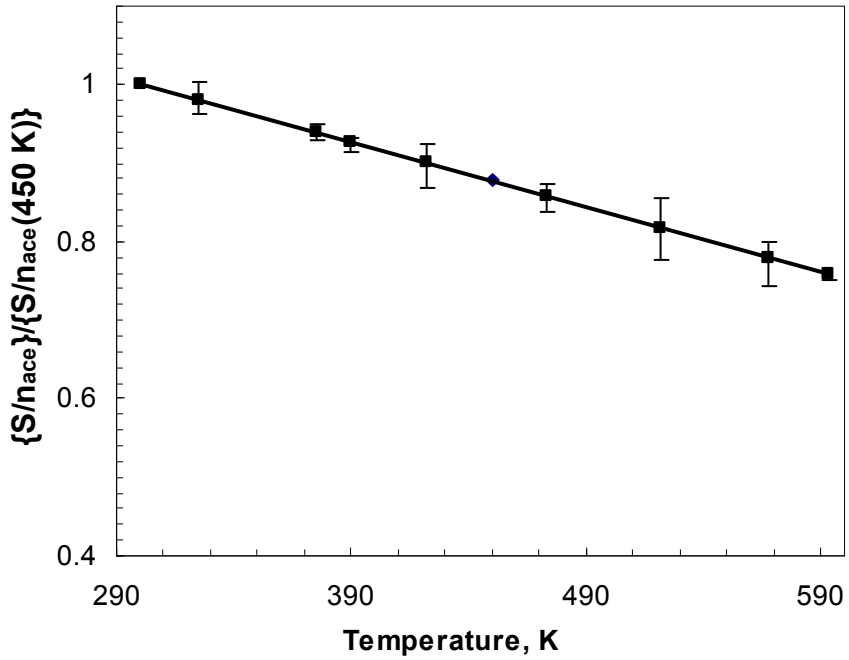

Figure 4.2: Normalized intensity signal per acetone molecule vs. temperature. Data normalized to value at 450 K. The bars are the min and max range for the pressure tested.

Figure 4.2 shows the normalized fluorescence intensity signal per acetone molecule at various temperatures. The signal per molecule is normalized by signal per molecule at 450 K, the median temperature for the temperature range tested. The results include data for pressures from 1 to 60 atm, with the average of the pressure data shown in the figure, and the pressure scatter indicated by the bars. For the ΔT=300 K range tested, the signal per molecule decreases by 24%, a smaller decrease compare to the fluorescence yield. This is due to the offsetting effect of the absorption coefficient, which increases with temperature, reducing the temperature dependence of the fluorescence signal. Thus, for

an experiment with temperatures limited to the ΔT=300 K range, the acetone vapor concentration can be estimated from the fluorescence signal, without correcting for the temperature variations, with an expected error of less that ±12%. As one might expect local fuel mole fractions to vary by at least an order of magnitude in typical mixing flows, the temperature uncertainty can be a small effect.

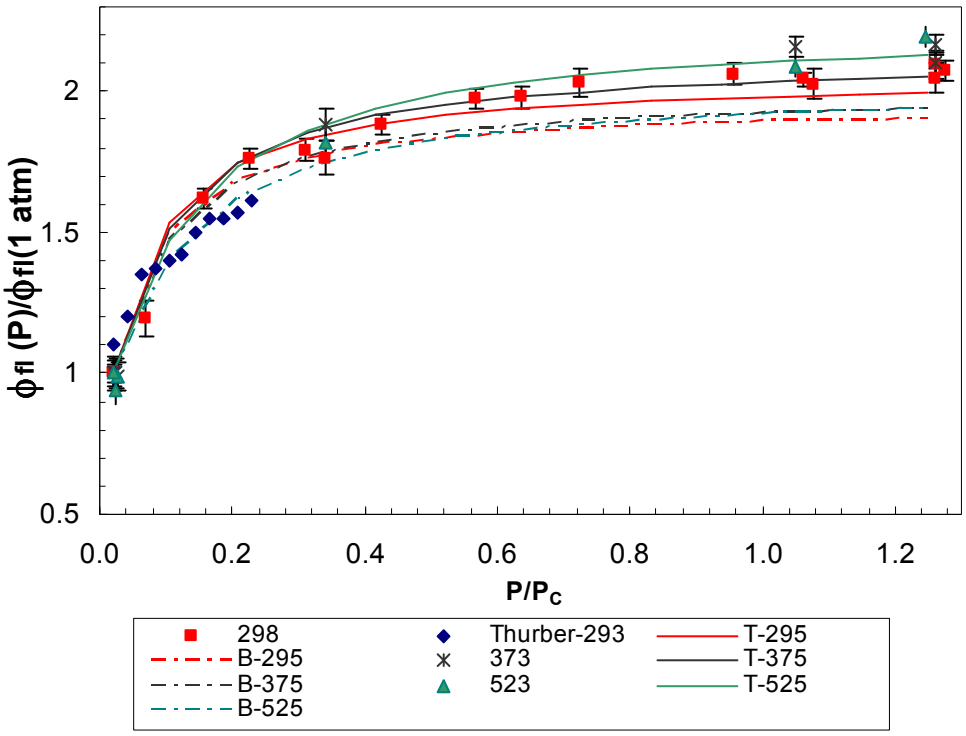

Figure 4.3: Normalized fluorescence yield of vapor acetone at varying pressures and temperatures in nitrogen co-flow. Data normalized to ϕ_{fl} at 1 atm for each temperature set. Symbols-experimental data. Solid lines-Thurber's model. Dash lines-Braeuer's model. Legends indicate the temperature in Kelvin.

The same fluorescence yield data are shown plotted as a function of pressure in Figure 4.3, where the data at a given temperature are normalized to the fluorescence yield value at 1 atm. The fluorescence yield is seen to increase with pressure, though above 30

atm there is little change. The fluorescence yield appears to asymptotically approach a value that is approximately twice the fluorescence yield at 1 atm. The cause of this behavior is the increase in the vibrational (collisional) relaxation rate with pressure. At higher pressures, molecules are more likely to relax to a lower vibrational energy level, with a slower intersystem crossing rate. This increases the probability that the molecule will fluoresce before it has a chance to cross to the triplet state. The increase in fluorescence yield is limited once the pressure is high enough that the vibrational relaxation rate dominates the intersystem crossing rate. Thus, the excited molecules will most likely relax to a thermal vibrational distribution before fluorescing, and the pressure dependence ceases.

The fluorescence yield models are also shown in Figure 4.3. The Thurber model produces a slight increase in the normalized fluorescence yield with increasing temperature, while the Braeuer model suggests that the fluorescence yield's pressure dependence is temperature independent. The experimental results indicate the latter, though again it is possible there is a small trend that is masked by the uncertainties in the experimental conditions. However, the uncertainties from the experiments are smaller than the increase in the fluorescence yield as with increasing temperature. Thus, if the fluorescence yield's pressure dependence is dependent on the temperature, the dependence is smaller than the dependence given from Thurber's model. As indicated in the temperature comparison, the magnitude of the measured pressure effect is closer to that predicted by the Thurber model. The figure also includes the previous room temperature experimental data from Thurber.[23] Those results were obtained in a fixed mass device, as opposed to the flowing system employed here that constantly moves new

fluid to the measurement volume. It is interesting to note that the current data provide a more consistent match to the model.

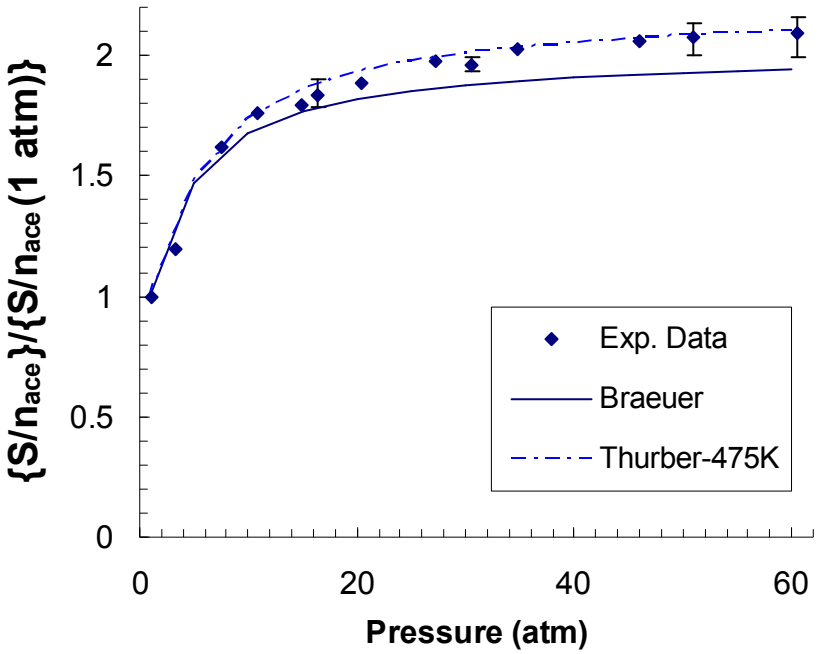

Figure 4.4: Average normalized fluorescence intensity signal per acetone molecule as a function of pressure. Bars show the min and max range for the pressure tested.

To examine the pressure dependence of the fluorescence signal (as opposed to the fluorescence yield) and because the data shows no clear correlation between the temperature and pressure dependence, the results are averaged over all the temperature tested (Figure 4.4). The normalized signal per acetone molecule has the same pressure dependence as the normalized fluorescence yield because the absorption coefficient (per molecule) is not pressure dependent. The figure shows clearly that the Braeuer model has under-predicted the pressure dependence of the fluorescence, though only by approximately 7%. The current experimental data more closely match the magnitude

predicted by the Thurber model, with the model result at 475 K (shown in Figure 4.4) providing the best fit. The maximum difference between the two varies from approximately -5% at 295 K to +5% at 600 K, since the Thurber model has an increasing pressure dependence with increasing temperature (unlike the data or the Braeuer model).

4.2 LIQUID ACETONE PHOTOPHYSICS

Liquid acetone emissions were measured at various temperatures and pressures. The pressure range is the same as that of the vapor experiments. The temperature range is more limited due to the observed increase in instability in the liquid jet as the temperature increased, causing the results to be inconsistent and increasing the systematic errors. In addition as the temperature increased, the concentration of residual acetone vapor in the test cell also increased, making it harder to reduce it using the nitrogen co-flow without having adverse effects on the stability of the liquid jet. However, the trends for fluorescence and phosphorescence intensity can be seen within the temperature and pressure range tested.

In addition to fluorescence and phosphorescence intensities, and thus the relative fluorescence and phosphorescence yields, the fluorescence and phosphorescence emission spectra were also measured to compare with the vapor emission spectra. This experiment was performed at room temperature and pressure. Furthermore, in addition to the 266 nm excitation wavelength, another excitation wavelength, 285 nm, was used to measure the spectra. The purpose was to determine whether the spectral properties change with different excitation wavelengths, especially with respect to the phosphorescence. It was previously shown by Ritchie *et al*. that the phosphorescence

spectrum is slightly red-shifted compare to the fluorescence spectrum when excited at 266 nm.[15] It was speculated that for longer excitation wavelengths, the red-shift would be larger, allowing the fluorescence signal to be separated from the phosphorescence signal spectrally as well as temporally. This would offer a diagnostic detection advantage and increase the measurable phosphorescence. Special attention is focused on the total intensity, since the larger the total phosphorescence intensity, the clearer the signal and thus the location of the subcritical/supercritical interface. 285 nm was chosen because its absorption cross-section is high, close to the absorption cross-section at 266 nm.

4.2.1 Liquid Acetone Fluorescence

The liquid acetone fluorescence yield is determined through essentially the same method as for the vapor. In the liquid case, however, the acetone density is assumed to be constant and is taken as the liquid density at 1 atm and room temperature, since the density of liquid does not deviate significantly with temperature and pressure over the conditions studied. In addition, it is assumed that the laser energy is totally absorbed as it traverses the liquid jet, and thus the same numbers of acetone molecules are excited by the laser. This is valid because liquid acetone is optically thick at the excitation wavelengths used. The laser energy is decreased to 1/e of its initial value within 28 μm of entering the jet, to less than 1% with 130 μm, which is less than the jet diameter. Therefore, the number of photons absorb is equal to the number of photons from the laser, which is proportional to the total acetone number density times the absorption cross-section. Thus, when the normalized fluorescence is calculated, the acetone concentration and absorption cross-section will be cancelled in the process, along with

the experimental parameters (Eqn. 4.4). The normalized fluorescence yield is equal to the to the normalized fluorescence intensity.

$$\frac{\phi(T,P)}{\phi(298K,1atm)} = \left(\frac{S(T,P)}{S(298K,1atm} \right) \qquad \text{Eqn. 4.4}$$

The liquid fluorescence yield results are shown in Figure 4.5. The data are normalized to the fluorescence yield at 298 K and 1 atm. The normalized fluorescence yield is seen to be nearly constant, with small fluctuations with temperature. The fluctuations have no apparent systematic variation with temperature and are larger compare to the uncertainties within the system. Thus, there are other uncertainties that have not being accounted for, i.e. acetone vapors surrounding the jet

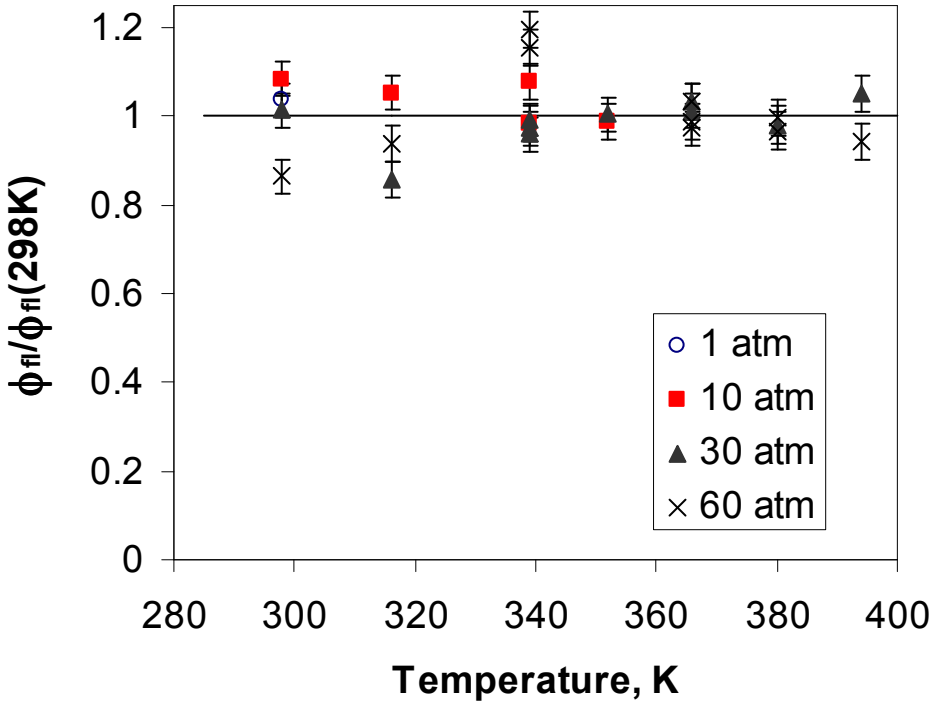

Figure 4.5: Fluorescence signal of acetone at varying pressure and temperature in a nitrogen co-flow

The pressure-averaged fluorescence intensity signals, normalized to the value at 298 K, are shown in Figure 4.6. While the normalized signals are lower than the normalized fluorescence yields (from Figure 4.5) as the temperature increases, the difference is very small since there is little change in the absorption cross-section over the limited temperature range tested here. Thus we can conclude that the liquid fluorescence yield, as well as the fluorescence signal per molecule, is nearly invariant in the pressure and temperature range of the experiments.

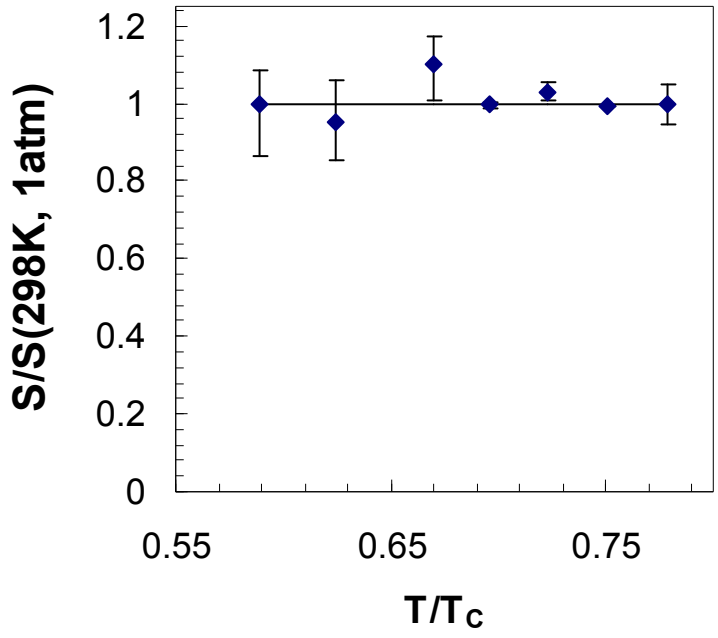

Figure 4.6: Average normalized fluorescence signal as a function of temperature for pressure ranging from 1 atm to 60 atm. Bars are min and max range for pressure tested.

These trends for the liquid acetone can be interpreted in part using the photophysical model presented in Chapter 2. For a liquid, the time between molecular interactions (collisions) is quite short (and nearly independent of pressure, since the liquid density is nearly constant with pressure). Thus the vibrational relaxation rate can be expected to be much faster than the intersystem crossing rate at all pressures. So after excitation, the acetone molecules would likely relax to a thermal distribution before fluorescing. This explains why changes in pressure and temperature would have little influence on the fluorescence yield. As noted in previously for the vapor case, the models (and data) indicate that at high pressure, or high densities, the fluorescence yield is higher. Thus the liquid acetone should also be expected to have a higher fluorescence yield compared to acetone vapor at the same pressure and temperature. Ignoring any other effects, one should expect the high pressure fluorescence yield limit for vapor acetone to be close to the liquid acetone fluorescence yield.

The data presented were for acetone jets in nitrogen ambient environments. Normalized fluorescence signals for an air co-flow at various pressures were also acquired at room temperature, and the results, normalized to the value at 1 atm, are compared to the nitrogen co-flow case in Figure 4.7. The blue and red lines represent the average signal for the nitrogen and air co-flow, respectively. The average for the air co-flow is slightly lower than the nitrogen co-flow. However, the difference is very small, less than 4%, which is within the bound of the uncertainty of the experiments. Thus, it can be concluded that there is no significant variation between the nitrogen and air co-flow for the pressures range from 1-30 atm, in contrast to the behavior of the vapor fluorescence.

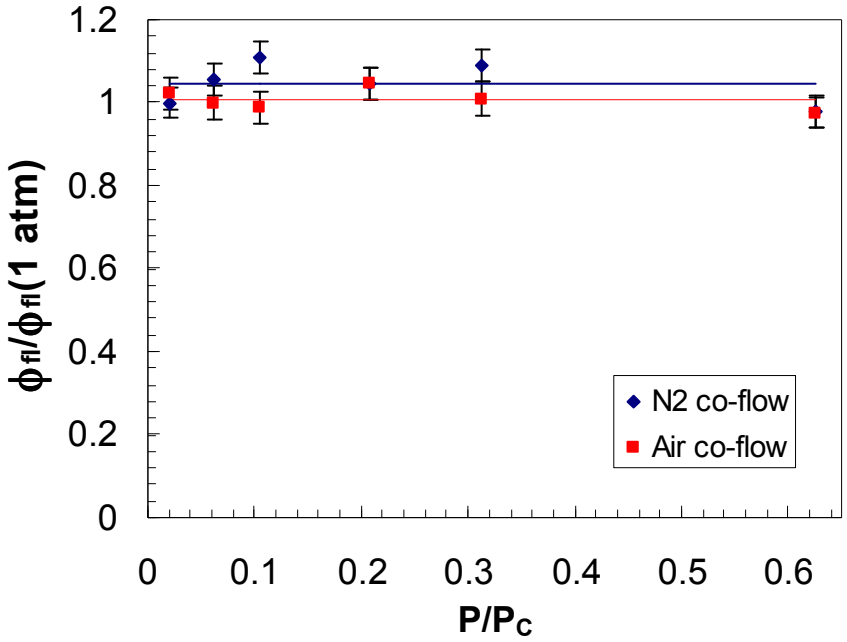

Figure 4.7: Fluorescence signal of liquid acetone at varying pressure and for air and nitrogen co-flows at room temperature.

Vapor fluorescence decreases in the presence of air compared to nitrogen for pressures above 2 atm at room temperature. This is caused by oxygen-assisted intersystem crossing from the singlet state to triplet state.[23] Thus, it is expected that the liquid fluorescence signal could also decrease in the presence of oxygen. A possible explanation for the similar fluorescence signal between the nitrogen and air co-flow for the liquid acetone is that the oxygen penetration into the jet is not fast enough, so the oxygen concentration within the jet is very low. The concentration is high enough to affect the phosphorescence signal, as seen later in this chapter, but insufficiently high to affect the fluorescence signal. The saturated concentration of oxygen inside liquid acetone is approximately 1×10^{-3} M, which is approximately 6×10^{20} molecules/m^3 or the equivalent concentration of gas with an oxygen partial pressure of 0.0244 atm.[29] This is

approximately 12% of the oxygen concentration of air at 1 atm. Since oxygen in air only affects the vapor fluorescence signal starting at an overall pressure of 2 atm (or an oxygen partial pressure of 0.4 atm), it is reasonable to assume that the saturated oxygen concentration inside the liquid acetone is too low to have an effect on the fluorescence intensity.

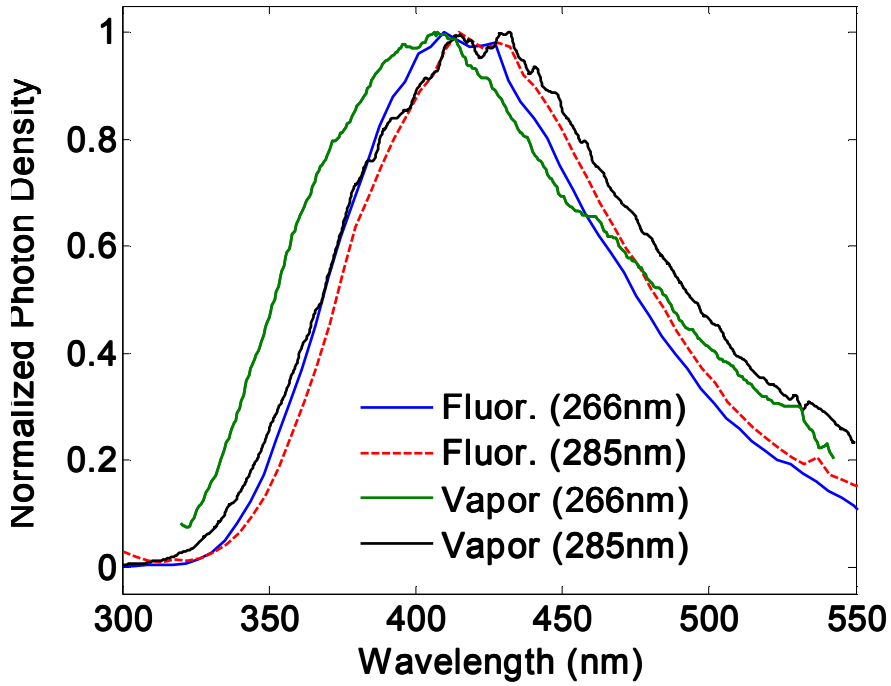

Figure 4.8: Fluorescence emission spectra comparison between liquid and vapor acetone. Liquid acetone spectra from two excitation wavelengths, 266 and 285 nm. 266 nm vapor spectrum from Bryant *et al*.[49]

Spectrally resolved measurements of the liquid acetone fluorescence emission, excited at two wavelengths, 266 nm and 285 nm, were obtained with a gated spectrometer, and the spectra are shown in Figure 4.8. The spectra for both excitation wavelengths are normalized to the highest peak of the individual spectrum to see the

variations in the spectrum. However, the peak intensity of both of the liquid spectra are comparable in intensity; the values differing less than 5% of the total value, with the 266 nm spectrum slightly higher. The fluorescence spectrum for 266 nm excitation extends from 300 nm to ~600 nm, with two slight, but noticeable peaks at 410 nm and 430 nm. The fluorescence spectrum for 285 nm excitation has the same range, although the spectrum is slightly red-shifted compare to the 266 nm case. The two peaks are also red-shifted, by ~5 nm to 415 nm and 435 nm. The red-shift does not seem to increase significantly for longer wavelength excitation.[45,50] In fact, Bortolus *et al.* used 337 nm excitation and found the fluorescence spectrum had a similar shape with the peak at 405 nm. Starting from short wavelengths, the liquid spectra quickly rises to its peak, within ~75 nm, and then slowly decays; the tail is at least twice as wide.

Figure 4.8 also shows the fluorescence spectra of vapor acetone for the two excitation wavelengths to distinguish whether there is a difference in the emission spectrum for the different phases. The 285 nm vapor is seen to be slightly red-shifted compare to the 266 nm vapor, which mirrors the liquid emission spectra. The overall shapes of the vapor and liquid spectra are similar, with peaks at roughly the same emission wavelengths. The vapor spectra are slightly wider than the liquid spectra, with a noticeable difference at shorter wavelengths, suggesting the fluorescence comes from a broader vibrational energy distribution in the vapor case. This is consistent with the rapid vibrational relaxation expected for the liquid.

4.2.2 Liquid Acetone Phosphorescence

Phosphorescence signals from liquid acetone at various conditions with a nitrogen co-flow are shown in Figure 4.9. The liquid phosphorescence signal is seen to be independent of pressure, at least up to 60 atm. The fluctuations are within the experimental uncertainty; the repeatability is ±5% over the data range. The phosphorescence signal for all three cases shown in the figure exhibits an exponential decline with increasing temperature. The data for 30 and 60 atm are fit with single exponential curves, which are also shown in the figure. The 60 atm curve has a slightly smaller slope compared to the 30 atm case. However, the difference between the two curve fits is so small, less than a few percent, that they can be considered the same. In addition, the phosphorescence signal is seen to approach a minimum limit as the temperature increases.

The phosphorescence behavior can be interpreted as follows. From the results shown in Figure 4.6, the liquid fluorescence signal is invariant for both temperature and pressure. This suggests that the fraction of excited molecules crossing from the first excited singlet state to the first excited triplet state is the same for the pressures and temperatures range tested. Therefore, the phosphorescence intensity should only be influence by processes that occur after the intersystem crossing. The data from Figure 4.9 indicate that the temperature reduces the phosphorescence yield. This reduction in the phosphorescence yield and signal was seen previously by Lewis and Kasha[51] for phosphors in a rigid system, i.e., a crystalline structure. They noticed that as the phosphor's temperature increased, and thus its fluidity, the intensity of the phosphorescence decreases.[51] The decrease was attributed to an increase in the

dissipation process, or quenching, as the temperature increased. The quenching represents an increase in collisions of the molecules. When the phosphors are in a crystalline structure, the rigidity of the structure prevents collisions between the molecules. When the phosphors transition to liquid state, the fluidity of the system allows molecules to collide with each other and as the temperature increase, the collision rate also increase, quenching the phosphorescence. Thus, there should be a corresponding decrease in the phosphorescence lifetime.

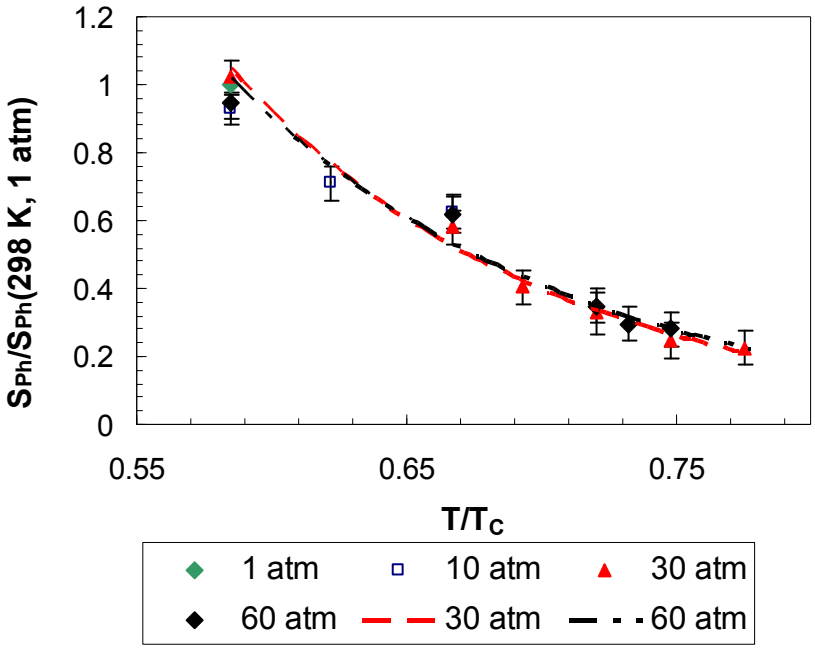

Figure 4.9: Phosphorescence signals of liquid acetone at varying temperatures from subcritical to supercritical pressure. Lines are least-square-error exponential fits.

Liquid acetone phosphorescence spectra at two excitation wavelengths (266 nm and 285 nm) were measured and are presented in Figure 4.10. The spectra were captured 300 ns after the laser pulse with a 10 μs gate time. The maximum wavelength for the

phosphorescence spectrum with 266 nm excitation is 407 nm, which is the same for 285 nm excitation. The peak wavelength found in the work of Pischel and Nau,[50] and Bortolus *et al.*[45] is approximately 440 nm for liquid acetone phosphorescence. However, Pischel and Nau also show the phosphorescence spectrum starting at a longer wavelength, 350 nm, compared to the Bortolus *et al.* and the current results, which start at 325 nm, similar to the fluorescence spectra. Comparing the phosphorescence and fluorescence, there is a reversal in the excitation wavelength effect. For fluorescence, longer excitation wavelengths induced red-shifting in the emission. However, the phosphorescence signal is seen to blue-shift for the longer excitation wavelength.

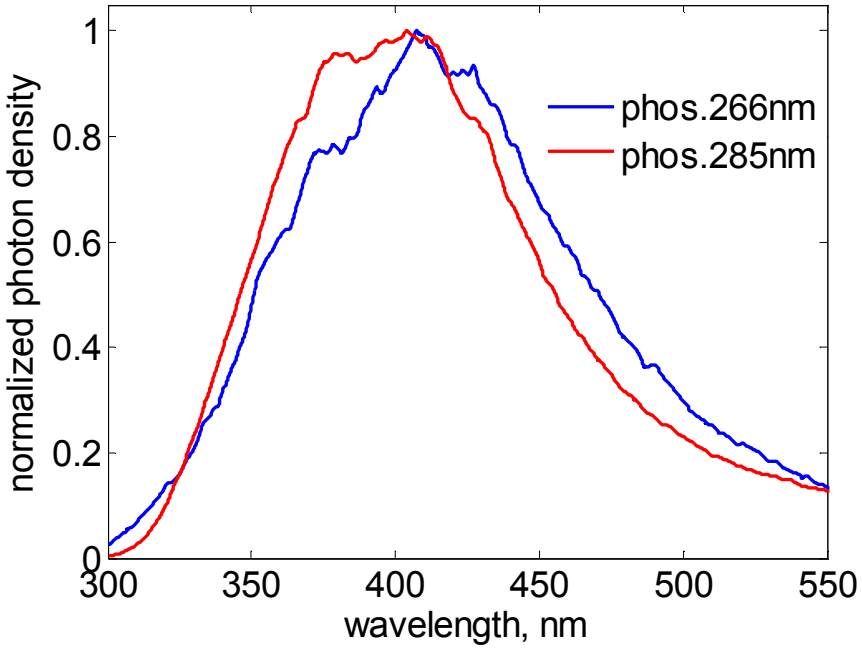

Figure 4.10: Normalized phosphorescence signal for 266 nm and 285 nm excitation. Both spectra normalized to the maximum signal for each individual spectrum.

The variation of the phosphorescence spectrum with respect to time is shown in Figure 4.11 and Figure 4.12. The spectra have been normalized so that the peak of each individual spectrum is unity. The fluorescence spectra are also shown to allow a comparison between the fluorescence and phosphorescence. The phosphorescence spectra show the same range in wavelength as the fluorescence spectra.

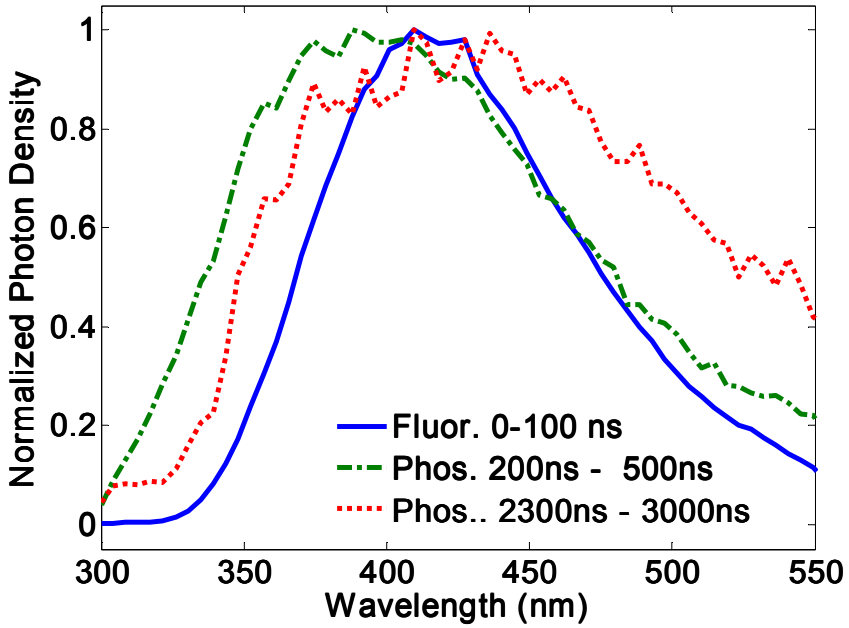

Figure 4.11: Variation of the normalized phosphorescence spectrum at various times for 266 nm excitation. The fluorescence spectrum is also shown for comparison.

Figure 4.11 shows spectra for 266 nm excitation for two different delay times after the laser pulse. For the short delay, the emission is blue-shifted with respect to the fluorescence, with a peak around 385-390 nm. As the delay time increases to ~2 μs, the spectrum is shifted towards longer wavelengths, with the peak now at 430 nm. This suggests that the rate of decay for each individual wavelength (or specific state in the triplet manifold) is not the same. The shorter wavelengths in the spectrum become less

prominent as the delay time increases; the spectrum is skewed more towards long wavelengths. Thus, the shorter wavelengths have a faster decay rate compared to the longer wavelengths.

The initial blue-shift in the phosphorescence spectra is probably from the molecules that are located at high vibrational energy levels when they cross over to the triplet state. This will allow them to be at higher vibrational energy levels compare to the vibrationally relaxed molecules in the singlet state, which would results in a blue shift of the spectra. As the delay time increases, more of the triplet molecules are vibrationally relaxed, thus the spectra become red-shifted.

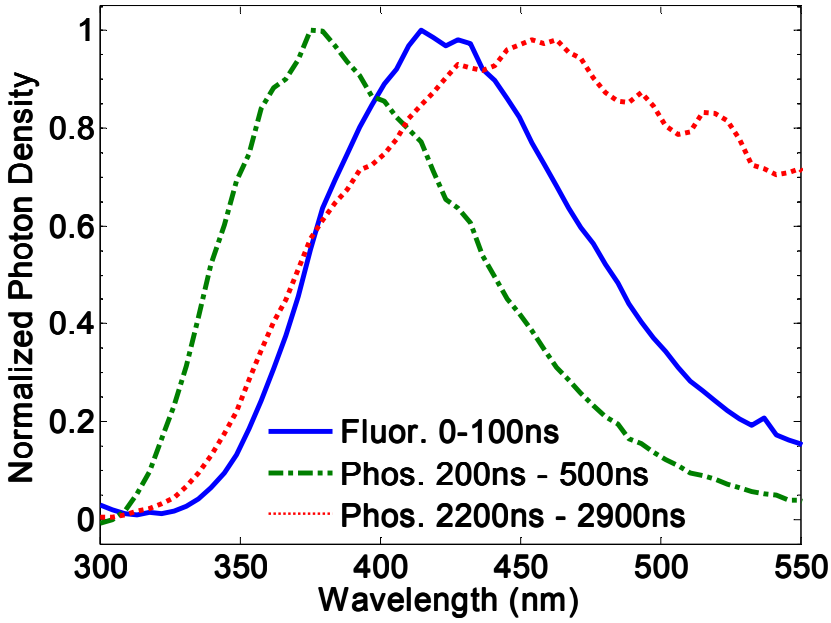

Figure 4.12: Variation of the normalized phosphorescence spectrum at various decay times for 285 nm excitation. Fluorescence spectrum is also shown for comparison.

Figure 4.12 shows the normalized phosphorescence emission spectra for two delay times and 285 nm excitation. The spectrum is similar to that for 266 nm excitation. For

short delays, the 285 nm excitation spectrum is more blue-shifted, with the peak at approximately 375 nm compared to ~390 nm. As the delay time increases, the 285 nm emission spectrum transitions from being more blue-shifted to more red-shifted than the emission for 266 nm excitation. The peak of the phosphorescence after ~ 2 μs delay is around 460 nm. The fact that the phosphorescence develops over time has been previously suggested.[29] Furthermore for the 285 nm spectrum, there is a sharper decline in the signal for the shorter wavelengths. This indicates that the decay rate (or lifetime) of the shorter emission wavelengths with the 285 nm excitation will be faster (or shorter) than with 266 nm excitation. Similarly, the opposite is true for longer wavelengths.

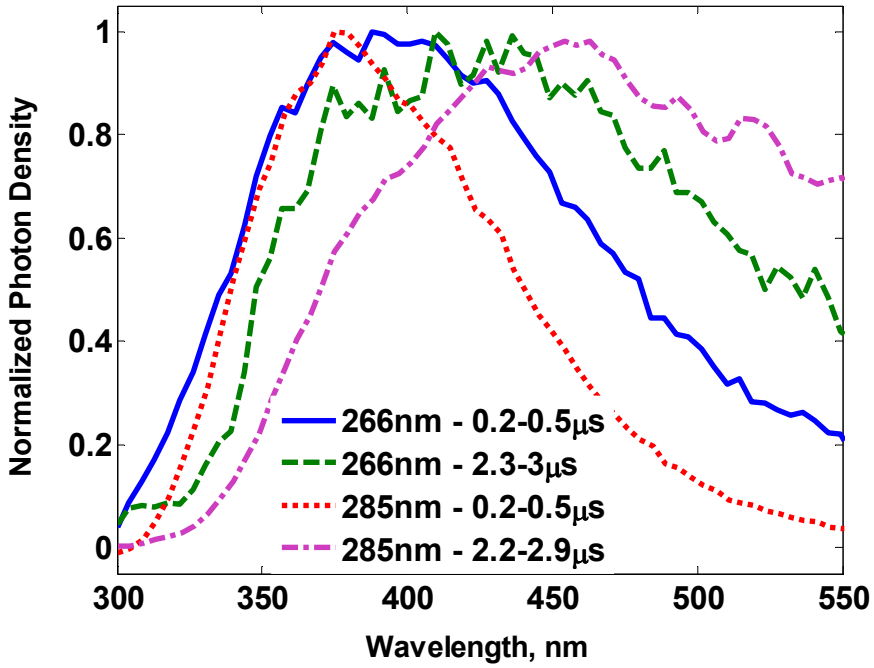

Figure 4.13: Excitation wavelength comparison of phosphorescence spectra after 700 ns and 2.3 μs delayed signal for two excitation wavelengths. Signal normalized to maximum of each individual spectrum.

The effect of excitation wavelength on the short and long delay phosphorescence is more clearly seen in direct comparison between the two spectra as shown in Figure 4.13. There is a more noticeable shift in the phosphorescence towards the longer wavelength for 285 nm excitation. Thus, it is to be expected that the lifetime of the individual wavelengths in the phosphorescence spectrum will be different, as well as the overall lifetime, which will be discuss later in the chapter.

As noted before, the phosphorescence intensity drops exponential with increasing temperature. Therefore, we expect its lifetime would also decrease with temperature. In addition, the phosphorescence spectrum shows different decay rates for different wavelengths. Thus, a time resolved analysis was done on the phosphorescence to determine the lifetime of the overall intensity as well as the individual wavelengths.

An initial attempt to determine the decay of the phosphorescence intensity signal for 266 nm excitation was attempted in a closed cuvette. However, the measured lifetime of 30 μs was due to the phosphorescence of the quartz cuvette. An improved experiment with a flowing jet provided more accurate data. The phosphorescence did not decay in a simple exponential fashion, rather a double exponential was required. The resulting phosphorescence lifetimes are plotted in Figure 4.14. For the temperature (~300-400 K) and pressure (1-60 atm) ranges tested, both lifetimes decrease with increasing temperature. The first lifetime drops by roughly a factor of two from 1.10±0.1 μs to 0.50±0.07 μs. The first lifetime for atmospheric pressure and room temperature, not shown in the figure, was calculated to be ~0.975±0.150 μs. The second, slower decay lifetime decreases by nearly the same ratio, from 7.0±0.5 μs to 4.0±0.5 μs. There is a much larger dependence of the total phosphorescence signal upon the first lifetime, since

approximately 85–90% of the phosphorescence occurs during the decay associated with the first lifetime. The phosphorescence lifetime also approaches a limit as the temperature increases, similar to the trend seen in the phosphorescence signal (Figure 4.9). The double exponential lifetime for the phosphorescence is different compare to other phosphorescence measurements, which typically shows a signal exponential decay. This might be due to the different quenching mechanisms in liquid compare to vapor acetone. However, the process is still unclear and needs to be studied further.

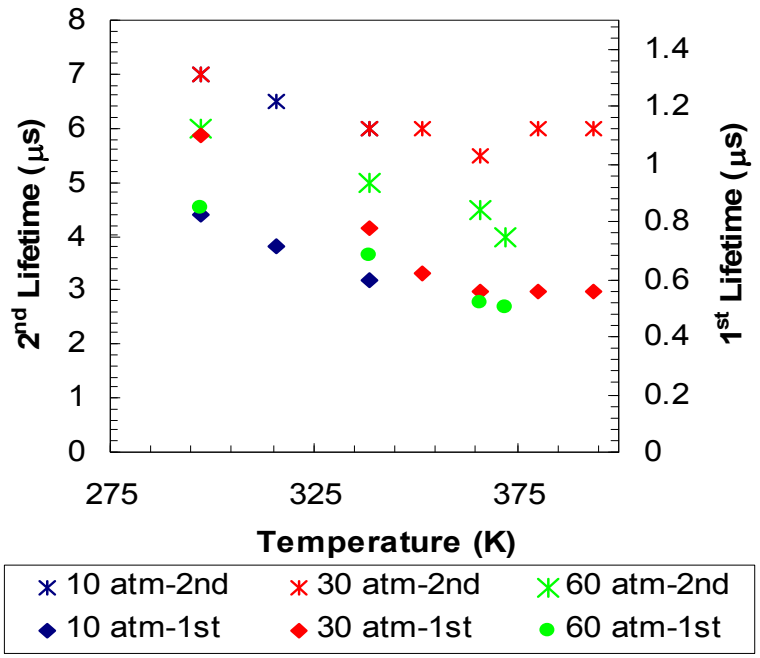

Figure 4.14: Phosphorescence lifetimes of liquid acetone at varying temperatures from subcritical to supercritical pressure.

This decrease in signal as the temperature increases is most likely due to collisional interactions that nonradiatively relax the triplet state, as stated earlier in the chapter. It is reasonable to believe that this collisional process is from acetone-acetone collisional interactions (since we are working with nearly pure acetone) that quench the

phosphorescence. Two candidate processes are self-quenching and triplet-triplet annihilation. In self-quenching, a triplet molecule collides with a ground state molecule to form two vibrationally excited ground state molecules. This self-quenching process is seen in other phosphorescence substances[40,52-54] and an increase in self-quenching with temperature has been noted.[40,52] Lozano estimated a self-quenching rate constant of 1.2×10^7 l/mol·sec for vapor acetone at room temperature.[40] Using this rate constant and the concentration for liquid acetone, the resulting phosphorescence lifetime is approximately 6 ns, which is two order of magnitude lower than the experimental result. Thus the rate constant is likely smaller than the value suggested by Lozano. The second process, triplet-triplet annihilation, is when two triplet acetone molecules collide to form one ground and one triplet acetone. This process is less probable, thus slower compare to self-quenching and could cause the second lifetime seen in the phosphorescence signal.

The phosphorescence lifetimes reported here compare well with the values determined by Bogan and Lee,[55] roughly 1 μs, and Wilkinson and Dubois,[56] ~400 ns. It is quite different than the ~30 μs lifetime proposed by Bortolus *et al*.[45] and Pischel and Nau.[50] The difference between the current lifetime and the latter two studies may be attributable to the conditions under which the data were taken, e.g., acetone preparation, temperature or excitation wavelength. As noted previously, phosphorescence follows after the laser excited acetone undergoes an intersystem crossing from the first singlet state, S1, to the first triplet state, T1. There are many vibrational modes that can be accessed in the T1 state, and each would have a different lifetime.[57,58] The 30 μs phosphorescence lifetime measured by Bortolus *et al*. was with 336 nm excitation. For the much shorter laser wavelengths used here, it is reasonable to assume that the eventual

distribution in the T1 state would be different leading to a change in the lifetime. This is partially substantiated by the difference in the 266 and 285 nm excitation lifetimes, ~0.975 μs and 1.1 μs for 266 nm and 285 nm, respectively, at room temperature and pressure and by the difference in the phosphorescence distributions (Figure 4.11-Figure 4.13) for the two cases. (For comparison, the accepted, oxygen-free phosphorescence lifetime of acetone vapor is ~200 μs,[40] and is attributed to emission from the vibrationally relaxed triplet state.[55,59])

Table 4.1: Phosphorescence lifetimes at selected detection wavelengths for both excitation wavelengths.

Excitation	**Emission Wavelength**		
Wavelength	**350 nm**	**450 nm**	**500 nm**
266 nm	645 ± 70 ns	860 ± 50 ns	1000 ± 70 ns
285 nm	450 ± 70 ns	720 ± 70 ns	1100 ± 70 ns

The variation of the lifetime due to vibrational energy state distribution changes is also evidenced in the spectrally resolved phosphorescence decays. The lifetimes for a few wavelengths are listed in Table 4.1 for both excitations, and plotted for a wide range of detection wavelengths in Figure 4.15. These results clearly show the difference in the lifetime for different wavelengths in the emission spectra. The lifetime steadily increases from ~500-650 ns at 350 nm to ~1-3.5 μs at 520 nm. The values shown for wavelengths higher than 500 nm are less accurate due to its proximity to the edge of the CCD detector causing the lower measured signals. These lifetime values bracket the overall spectral lifetime determine from the intensity decay in the free jet images taken at room

temperature and pressure. The short wavelength lifetimes are less than the integrated result, while long wavelength lifetimes are higher. Note that the 285 nm excitation lifetimes seen in Figure 4.15 are in many cases higher than the spectrally integrated values of Table 4.1. This is because the integrated lifetime is weighted towards the peak region of the phosphorescence spectrum (400-415 nm). Also, the red-shift in the 285 nm excitation spectrum with increasing delay is seen clearly by the increase in the lifetime at the longer wavelengths.

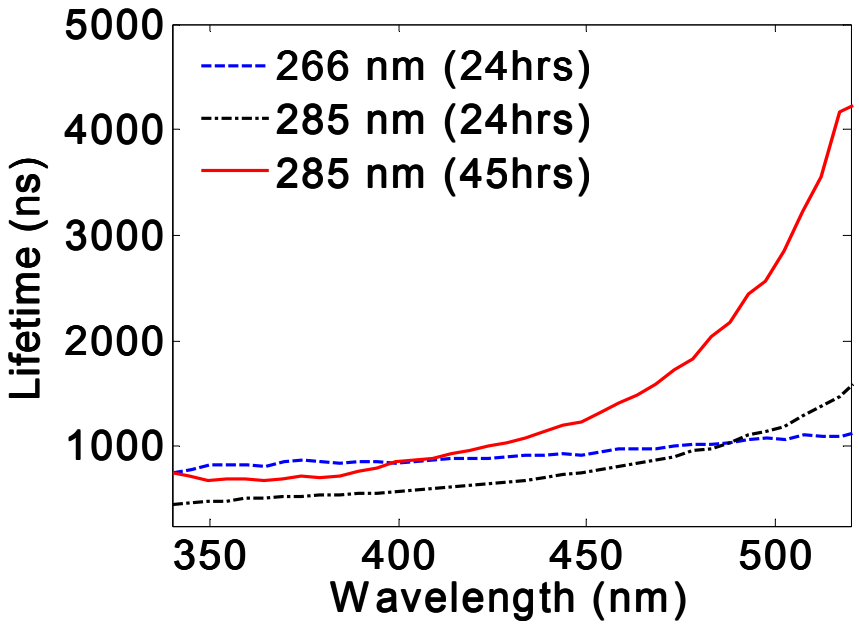

Figure 4.15: Spectrally resolved phosphorescence lifetimes for the two excitation wavelengths.

The lifetimes shown in Figure 4.15 also verify the earlier finding that the phosphorescence lifetime depends on the excitation wavelength. In addition, since the overall lifetime for 285 nm excitation is larger than the 266 nm excitation, seen in both the emission spectrum and the signal from the jet, it can be assumed that the

phosphorescence yield will also be larger. The phosphorescence yield is determined Eqn. 4.5

$$\phi_{ph} = \frac{k_{ph}}{k_{ph} + k_{other}} \qquad \text{Eqn. 4.5}$$

Since the phosphorescence rate is much slower compared to other processes and assuming the phosphorescence rate is a constant, the lifetime would depend on the rate of other processes. So for shorter lifetimes, the rates of other processes have to increase, thus decreasing the phosphorescence yield and vice versa. In addition to the phosphorescence yield increasing with longer excitation wavelength, the phosphorescence signal would also increase with longer wavelength.

The total intensity of the liquid acetone phosphorescence was also compared to the total fluorescence intensity for 266 nm and 285 nm excitation. The phosphorescence data were acquired with a 200 ns delay after the laser pulse to reject the fluorescence signal. The prompt signal was measured with a 300 ns intensifier gate width starting 100 ns before the laser pulse, effectively producing a 200 ns long gate. Thus the prompt signal contains both fluorescence and some fraction of the phosphorescence. Figure 4.16 shows the prompt and integrated phosphorescence spectra, with the phosphorescence accurately scaled with respect to the prompt signal. The fluorescence signal is clearly much larger. Integrating the two spectra results in a phosphorescence to fluorescence ratio of 0.035 for 266 nm excitation. For 285 nm excitation, the ratio is 0.08, which is more than twice the 266 nm value.

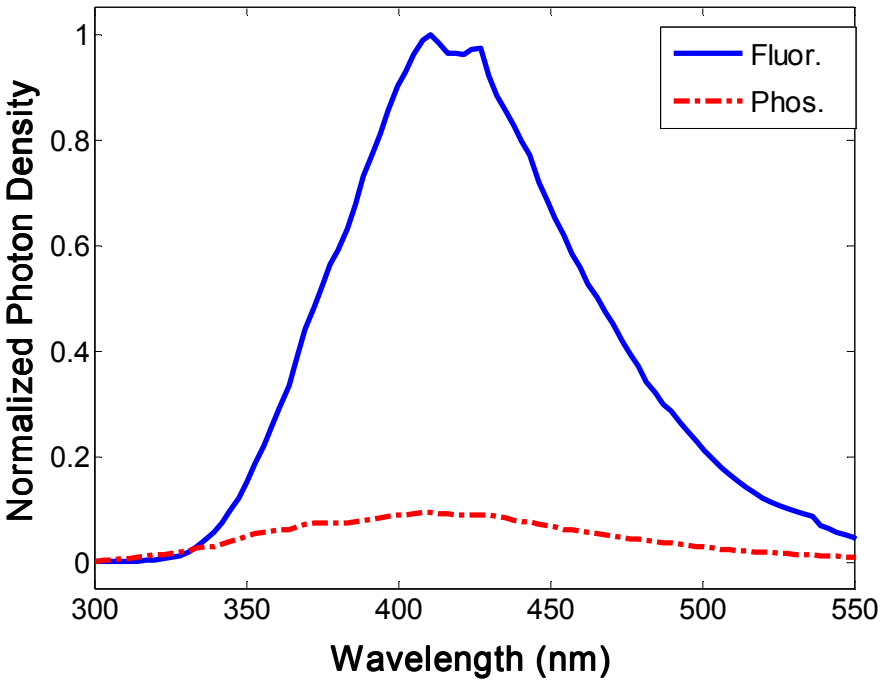

Figure 4.16: Fluorescence and phosphorescence total intensity comparison for 266 nm excitation: Fluorescence spectrum taken at 100 ns before laser pulse, 300 ns gate. Phosphorescence spectrum taken at 200 ns after pulse, 30 μs gate.

The relatively lower signal from the integrated phosphorescence would suggest that there is little phosphorescence contamination in the prompt signal and vice versa. Assuming that the fluorescence lifetime is close to the reported value (<5 ns), the delayed signal (phosphorescence) is too strong to be attributed as a remnant of the fluorescence (the integrated fluorescence would be at least 7 orders of magnitude below the measured phosphorescence intensity over the delayed integration period). The increase in phosphorescence/fluorescence ratio with excitation wavelength was also seen by Copeland and Crosley.[60] They reported that the vibrationally excited triplet emission has maximum signal intensity when acetone is excited at ~313 nm, which is well above the peak of the absorption spectra (~280-290 nm). Bortolus *et al.*[45] measured the phosphorescence and fluorescence intensity with 336 nm excitation, and their reported

P/F ratio was 1.1. This confirms that the P/F ratio will increase for longer excitation wavelength. It was also found that for longer excitation wavelength, in this case from 266-285 nm, there was no noticeable change in the fluorescence intensity, this suggest that the phosphorescence intensity increases with longer excitation wavelength. Thus, if a higher phosphorescence signal is needed, a longer wavelength should be used for an excitation source.

To summarize, the vapor and liquid photophysical properties were measured at elevated temperatures and pressures (T/T_c~0.6-1.2 and p/p_c~0.02-1.3). The results for the vapor fluorescence yields are similar to the model predictions. The liquid fluorescence yield is constant for the temperature and pressure range measured (T/T_c=0.6-0.8, p/p_c=0.02-1.3), and therefore the fluorescence signal would also be constant. The liquid phosphorescence signal shows an exponential decline with increasing pressure but is invariant with pressure. From these results the acetone PLIFP can now be used to determine the mixing characteristics, e.g., mixture fraction, within a flowfield from subcritical to supercritical conditions.

In addition, emission spectra for vapor and liquid acetone were measured. The fluorescence signals for vapor and liquid are similar with small variations of the spectral distributions and peak emission locations. The liquid phosphorescence emission spectra shows slight red-shifting in the peaks compared to the fluorescence spectra when the excitation wavelength changed from 266 nm to 285 nm. However, the overall range of the fluorescence and phosphorescence spectra is the same. Thus the conclusion is made that the phosphorescence signal can not be separated from the fluorescence through spectral filtering. Therefore, the only method to discriminate between the two sources of

emission is through a time delay in the image acquisition. Moreover, using a longer excitation wavelength increases the overall phosphorescence signal. This would increase the signal-to-noise ratio, and the interface location will be more accurate.

CHAPTER 5

SUBCRITICAL TO SUPERCRITICAL MIXING MEASUREMENTS

This chapter presents demonstrations of the PLIFP technique for jet mixing measurements. The first section describes the quantification process for liquid acetone droplets, which are important in the breakup of subcritical liquid jets. The next two sections present results for the measurement for the mixing of a liquid acetone jet when injected into a subcritical to supercritical environment. The image data are quantified using the photophysical properties determined in the previous chapter. Also included is a discussion of the effectiveness of the PLIFP technique for determining the "transition" interface based on diffusivity.

5.1 QUANTITATIVE LIQUID ACETONE FOR DROPLETS

For liquid droplets below some diameter, the emission intensity of the droplets is nearly proportional to the total mass of the droplets. Ritchie *et al*. created a model to determine the size of a liquid droplet from the intensity emitted by it.[15] It was assumed that the fluorescence intensity from a liquid droplet of a certain mass is equal to the fluorescence intensity of the acetone vapor of the equivalent mass; the fluorescence yield of the liquid and vapor were assumed to be the same. The fluorescence yield for liquid is reported to be 0.0014, and the vapor fluorescence yield is reported at 0.0012 at room temperature and atmospheric pressure.[61] The vapor value was calculated from the fluorescence and ISC rates measured. The difference between the two is 17%, thus the assumption is reasonable (at least at atmospheric pressure). From the result in Chapter 4

it one could expected that the liquid, being a high density version of a vapor, could have a fluorescence yield double that for vapor, assuming the rates of the energy transfer processes are the same for both. Halpern and Ware, however, showed that the effective rates are different between the phases.[61] The ISC rate is faster in the liquid phase, thus the fluorescence yield is reduced. However, laser extinction effects in the highly absorbing liquid (for large enough droplets) and interference from the acetone vapor fluorescence do not allow for a simple proportionality to exist between acetone mass and the measured fluorescence.

Thus Ritchie suggested another approach that employs phosphorescence to determine the size of the droplets.[62] The liquid phosphorescence is more advantageous to use to determine the droplet size since it does not requires correction for the vapor phosphorescence intensity as that signal is efficiently quenched by oxygen. Thus the signal from the liquid phosphorescence is only from the liquid. The liquid phosphorescence to vapor fluorescence ratio can be determined from Eqn 5.1

$$\frac{S_{P.L.}}{S_{F.V}} = \frac{S_{F.L.}}{S_{F.V.}(T,P)} \frac{S_{P.L.}(T)}{S_{F.L.}} \qquad \text{Eqn 5.1}$$

Since the fluorescence yield of the vapor and liquid at different temperature and pressure is determined from the results presented in Chapter 4, the ratio between the two fluorescence intensities is also known. Also as variations in the liquid phosphorescence intensity with temperature and pressure are known, the ratio between the liquid fluorescence and phosphorescence can be determined as well. Thus, this allows for the calculation of the mass of a droplet from PLIFP signals.

$$dV_d n_d = m_d = S_{P.L.} \frac{S_{F.V.}}{S_{P.L.}} \frac{1}{IC_V \phi_v \mid_{298K,1atm}} \qquad \text{Eqn 5.2}$$

The technique should work well at low temperature but will become less accurate as the temperature increases. There are two reasons for this problem. One, the phosphorescence intensity decreases as the temperature increases. This will increase the minimum distinguishable droplet size, and the uncertainty will increase as the signal-to-noise ratio decreases. Two, any diffusion of oxygen into the droplet will also reduce the phosphorescence signal, thus further reducing the effectiveness of the technique. Since single images do not provide details on the time since a droplet has broken off from the jet, it is difficult to estimate the amount oxygen diffusion, which would be required for any correction procedure. Therefore, rather than using the phosphorescence signal to determine the mass of the droplet, the liquid fluorescence intensity should be used instead. From the data in Chapter 4, it is now clear that the fluorescence intensity (per acetone molecule) is essentially independent of temperature, pressure, and oxygen concentration. Thus, fluorescence provides a superior signal for the liquid mass calculation.

The total mass of the droplet can be calculated as follows. The fluorescence signal from the pixels in which the droplet is located is a combination of the liquid and vapor within those pixels.

$$S_{tot} = I\, C_d\, dV_d\, n_d\, \phi_d + I\, C_V\, dV_V\, n_V\, \phi_V \qquad \text{Eqn 5.3}$$

Here, C_V *and* C_d are constants that encompass the optic efficiency, photon energy, and the absorption coefficient for the vapor and droplet, respectively; dV_d and dV_v are the volume of the droplet and vapor within each pixel and I is the laser intensity. Assuming that the vapor density within those pixels is similar to the vapor density of the adjacent pixels, the vapor signal can be subtracted from the total signal to give the signal from the droplet. Since the fluorescence yield is the same for vapor and droplet at room temperature and pressure, a droplet of a given size with mass, m, will provide the same intensity as the vapor with the same mass.

$$S_d\,|_{298K,1atm,m} = S_V\,|_{298K,1atm,m} = I\,C_V\,dV_V\,n_V\,\phi_V \qquad \text{Eqn 5.4}$$

At different conditions (T, p), the liquid fluorescence yield remains the same; thus the droplet mass is:

$$dV_d n_d = m_d = \frac{S_{tot} - IC_V dV_V n_V \phi_V\,|_{T,P}}{IC_V \phi_v\,|_{298K,1atm}} \qquad \text{Eqn 5.5}$$

To determine the minimum droplet size that can be determined with this technique, a set of experiments were performed at room temperature and pressure to measure the droplet phosphorescence for various droplet sizes. From this the minimum droplet size at room temperature and pressure can be calculated and the respective minimum droplet size at different temperatures and pressure can be estimated from the P/F ratio at that temperature and pressure. Figure 5.1 provides an example of the fluorescence image, the phosphorescence image and line plots of the intensities for two droplets.

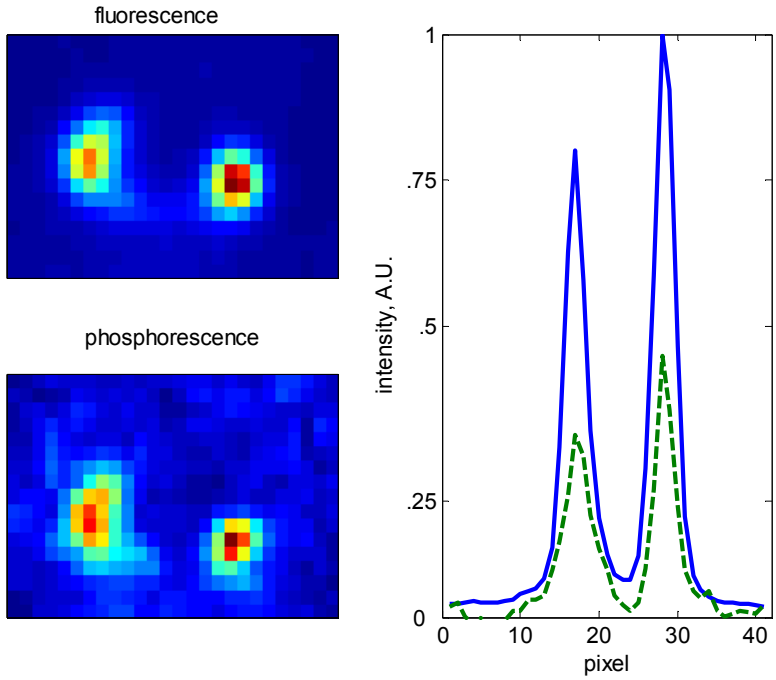

Figure 5.1: Fluorescence image, phosphorescence image and intensity plot for two droplets at room temperature and pressure. Solid line - fluorescence. Dash line – phosphorescence.

The magnification of the system is approximately 30 μm per pixel. Given that the images of the droplets are about 7 and 6.5 pixels across, respectively, the two droplets size are 210 and 195 μm, respectively. However, the camera system is not able to resolve objects down to one pixel. The optics tends to blur small objects; typically this is characterized by the lens' point spread function (the response to an object of infinitesimal size). So the actual droplet size would be smaller than the value given simply by the image size. The blurring of the camera optics was estimated by imaging a 100 μm object, and the number of pixels in the image was measured. At 30% of the maximum intensity, the object covered 8 pixels, which corresponds to a 240 μm in the object plane. Thus, the camera's blur is approximately 140 μm for a 100 μm object. The amount of blur would

decrease somewhat for smaller objects, since the resulting object size is a convolution of the actual object with the response of the optics. Therefore the actual sizes of the two droplets shown in Figure 5.1 are more likely to be 80-90 μm and 65-75 μm respectively. For these two droplets, the calculated masses based on the fluorescence signal are 2.56×10^{-10} kg and 1.93×10^{-10} kg, which correspond to densities of ranging from 700 to 925 kg/m^3 for the first droplet and from 830 to 1050 kg/m^3 for the second droplet. The percent error from the known liquid density is approximately −12% and +32%. Thus, this method is a reasonably accurate way to determine the mass of the droplets, especially if the point spread function of the optics is improved.

The method is limited by the optical resolution as well as the phosphorescence signal from the droplets. As mention above, the phosphorescence signal will decrease with increasing temperature and oxygen diffusion. Thus the minimum measurable droplet size will also tend rise with increasing temperature. At region where the phosphorescence signal is fully quenched (e.g. for very small droplets), the droplets mass and size can still be calculated using the difference in intensity between the background, or vapor, fluorescence and the droplet fluorescence, which oftentimes is very high. If the corresponding density of the liquid at a temperature and pressure is known, the droplet size can also be inferred from this. This calculation will allow smaller size droplets to be calculated.

Thus for the acetone PLIFP technique, the vapor fluorescence signal should be used to determine the acetone number density, and thus the mixture fraction of the system. The liquid phosphorescence signal is used to delineate the subcritical/supercritical and liquid/vapor interface. In addition to the interface, the phosphorescence signal could also

used to calculate the size of the larger droplets within the system. For smaller droplets, where there is little to no phosphorescence signal, the liquid fluorescence signal is used to determine the size of the droplets.

5.2 SUBCRITICAL MIXING

Simultaneous fluorescence and phosphorescence images of acetone jet in air environment at sub to supercritical conditions were taken to calculate the mixing of a liquid jet being injected into a subcritical to supercritical environment. In addition, the images are used to determine whether the phosphorescence signal can delineate the location of the highly diffusive/less diffusive interface of the jet or not. The results shown in this section are for room temperature acetone liquid jets injected into subcritical environments.

The images for the case of room temperature acetone jet entering the test chamber at pressure of 15 atm and temperature of 540 K are shown in Figure 5.2. The images are the fluorescence intensity, the phosphorescence intensity, the superimposed phosphorescence image upon the fluorescence image with the calculated acetone density, and the mixture fraction. The intensity of the fluorescence signal is converted into acetone density (kg/m^3) within the chamber, as seen in the third image. The fuel density and the air density are used to calculate the mixture fraction of the test chamber and are shown in the fourth image. The superimposed image shows the phosphorescence signal following the gas-liquid interface well, and it was able to capture the disturbances on the surface of the acetone jet. The fluorescence and phosphorescence signal seen within the liquid jet is because of an optical effect that is caused by the curvature of the liquid jet. The

curvatures of the jet acts as optical lenses with various focal lengths, thus the fluorescence and phosphorescence signal is seen at a different location of the jet. The more instabilities and curvatures in the jet, the more distance the signal will be seen from the original site. The lensing effect seen is a characteristic of liquid jet, due to the difference in the index of refraction of the acetone liquid and the surrounding vapor. This effect will cease when the liquid transitions to supercritical or vapor fluid, where the index of refraction gradient is reduced between the jet and the surrounding fluid.

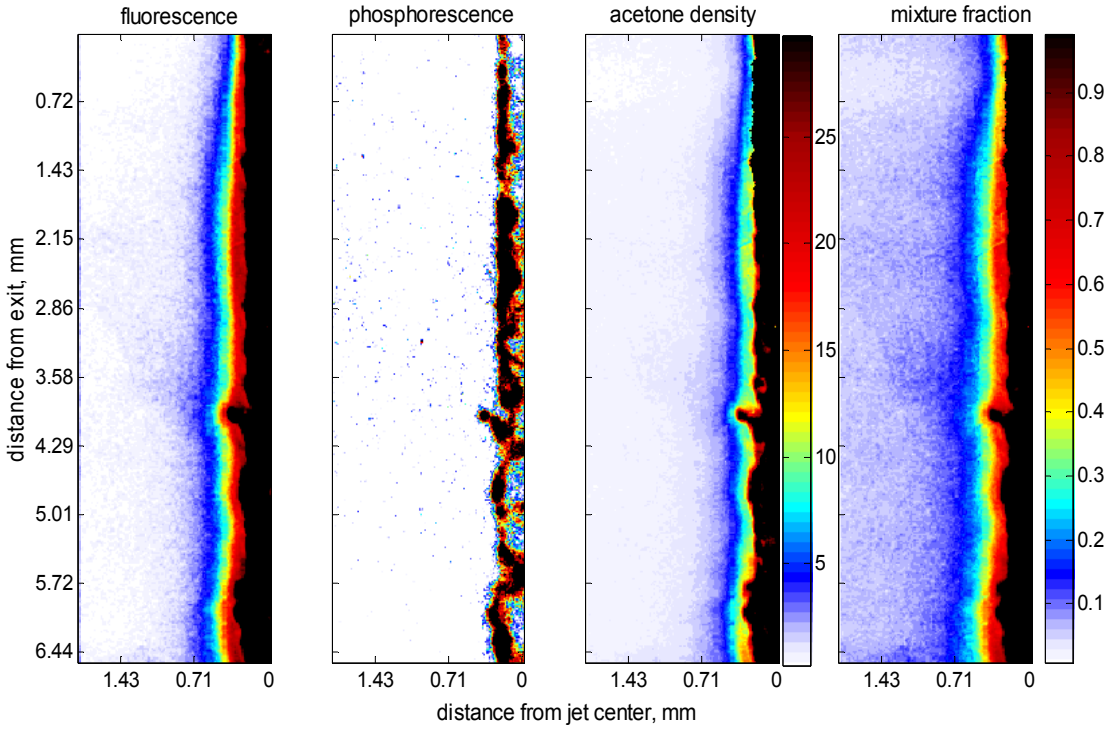

Figure 5.2: Simultaneous fluorescence, phosphorescence, and superimpose image of both of a room temperature liquid acetone jet at 15 atm injected into 540 K air. 0 mm is at jet center. Mass flow rate – 6.32 g/s. V_{jet} - 10.2 m/s. $V_{gas} \sim 0$ m/s.

The density map from the figure shows that the majority of the fuel is still in liquid form and only a small portion of the liquid had evaporated. A shear/mixing layer, or the

vapor layer, can be seen right next to the liquid jet and it is barely spreading as it goes downstream. The mixing layer thickness grew from approximately 200 μm to 500 μm, or about 0.5d, in one diameter length and it remain almost constant at that thickness. However, due to the optics blurring effect the actual thickness will be smaller, from 75 μm to 375 μm. The vapor spreading angle is measured to be 10° for the first millimeter, or y/d = 1, where y is the distance from the jet exit. Further downstream, the spreading angle is reduced to less than 2°. The liquid jet is seen to be of constant size for the range measured; the dark-core angle, i.e., the spreading angle of the liquid jet, is less than 1°. The mixture fraction image shows the fuel mixture fraction to be, on average, 0.1 away from the jet. This is due to the low air velocity causing the acetone vapor to remain within the test chamber for a longer length of time. Within the mixing layer, the mixture fraction is substantial, as high as 0.7.

The images for a room temperature liquid jet injected into a 36 atm, 540 K test chamber are shown in Figure 5.3. The jet looks similar to the 15 atm case. There is no expansion, change in width, of the liquid jet, and the acetone mixing layer thickness remains almost constant after an initial increase in the first diameter length. However, there is not a large agglomeration of vapor around the jet as was seen at 15 atm. In addition, there is a higher concentration of acetone vapor in the test chamber, and there is a noticeable increase of the vapor spreading angle compared to 15 atm. The averaged vapor spreading angle is approximately 15° compared to the 2° seen at 15 atm. There are also more disturbances on the surface suggesting higher turbulence within the system. Thus, it is possible the acetone that has evaporated from the liquid jet is being convected into the rest of the chamber due to the high turbulence. At the bottom of the fluorescence

image, a small droplet can be seen close to the center. However, the phosphorescence image shows no signal within the area. It is possible that the droplet was small enough that oxygen was able to diffuse into the liquid fully, thus quenching the phosphorescence signal or the phosphorescence signal from this small a droplet is below the detection limit of the camera system. Using the method mentioned earlier for droplet measurements, the mass and the size of the droplet can be found. The mass is 2.64×10^{-11} kg, corresponding to a droplet size of 40 μm.

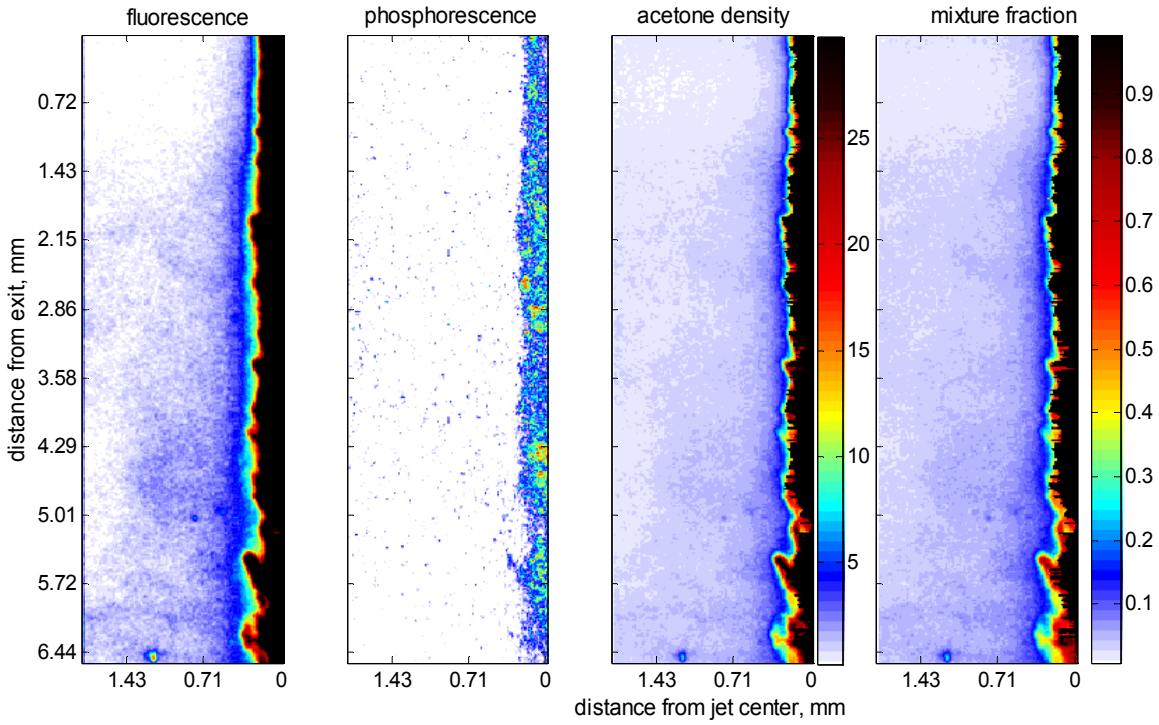

Figure 5.3: Simultaneous fluorescence, phosphorescence, and superimpose image of both of a room temperature acetone liquid jet at 36 atm injected into 540 K air. 0 mm is at jet center. Mass flow rate – 4.35 g/s. V_{jet} – 7.6 m/s. V_{gas} ~ 0 m/s.

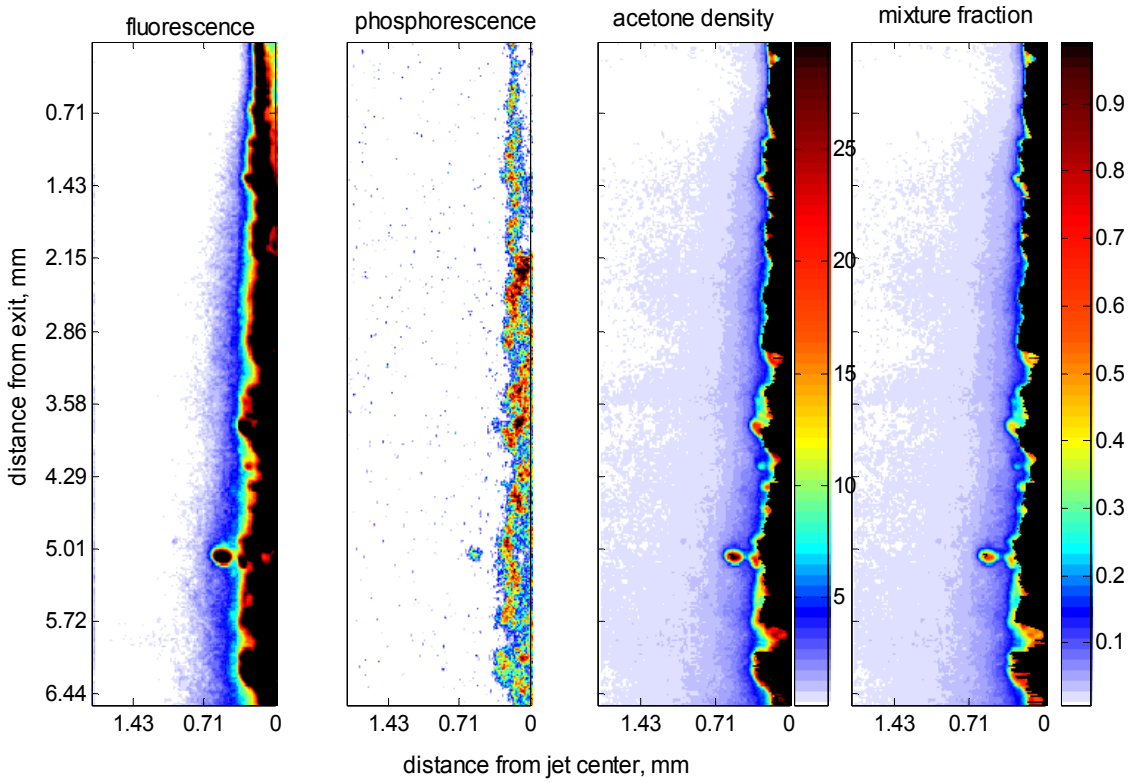

Figure 5.4: Simultaneous fluorescence, phosphorescence, and superimposed image of a room temperature liquid acetone jet at 45 atm injected into 540 K air. 0 mm is at jet center. Mass flow rate – 4.75 g/s. V_{jet} – 7.6 m/s. V_{gas} ~ 1 m/s

Figure 5.4 shows the images of acetone liquid jet injected into the test chamber at 45 atm and 540 K, which is close to the critical point of acetone. Comparing the mixing layer spreading angle between the 15 atm case and this case, the initial spreading is slower than the 15 atm case. However, the mixing layer is seen to continue to thicken further downstream, similar to the 37 atm case instead of remaining constant like the 15 atm case. The shear layer spreading rate is approximately 5° for y/d > 1. The jet shows more disturbances and instabilities on its surface compared to the 15 and 37 atm cases. This might be due to the lower jet velocity in addition to the increase in the air velocity, creating higher shear on the jet surface, thus more surface instabilities. Less acetone

vapor is seen throughout the test chamber and also close to the jet and the vapor spreading angle is smaller compare to 37 atm. This is possibly caused by the increase in the air velocity, thus more air is pushing the vapor downstream, reducing the shear layer thickness and vapor within the chamber. The mixture fraction is smaller throughout the test chamber, compared to the 15 atm test. This is due to the increase in density at higher pressure, thus the mixture fraction is less, even at locations where the vapor concentration is the same for the three cases.

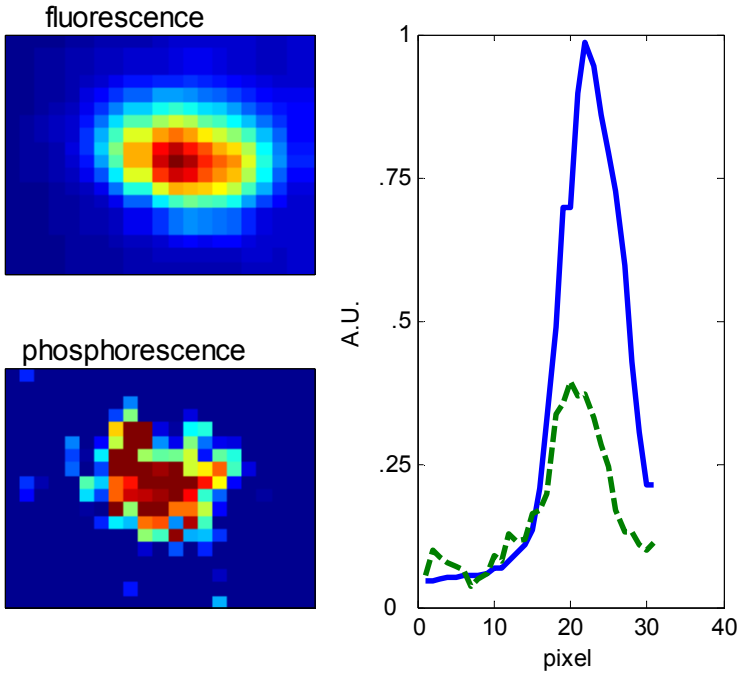

Figure 5.5: Fluorescence and phosphorescence image of droplet seen in Figure 5.4 and the actual intensity of both. Droplet size – 10 pixels ~100 μm. Solid – fluorescence. Dash – phosphorescence.

A point of interest from the figure is that the phosphorescence signal was able to identify the liquid droplet next to the jet. Figure 5.5 shows a close-up image of the droplet. The phosphorescence signal shows the droplet to be ~10 pixels across and based

on the optical magnification this corresponding to a 100 μm droplet. Since this is a large droplet, the oxygen is unable to penetrate into the droplet fully. Also, there is still fluorescence to the right of the droplet, suggesting that not all of the laser's energy was absorbed by the droplet. This is possible if the droplet is smaller than the laser sheet's thickness, thus a portion of the laser's energy will not be absorbed by the droplet.

Overall, the subcritical jets shown above behave like liquid jets entering into a heated environment. The vapor spreading angles are similar to the values seen by other researchers for the same types of conditions.[3,8] In the last case shown above, the chamber pressure and temperature was close to the acetone critical point. However, the jet still behaves similar to a liquid jet; the jet breakup through droplets and ligaments are seen in the images. The energy required to increase the liquid temperature close to the critical temperature is likely higher than the energy provided by the air flow (as the liquid heats up, the nearby air cools off). Thus the jet does not undergo a critical transition. The temperature of the liquid jet has to be increased or it needs to be injected into a more heated environment to allow the jet to reach near critical conditions.

The phosphorescence signal is seen only for liquid acetone as the phosphorescence signal from the vapor is fully quenched by oxygen as expected. The oxygen is able to penetrate through the vapor mixing region. It has also been demonstrated that the phosphorescence signal can follow the liquid/vapor interface very well (as seen in Figure 5.6). In addition, the intensity of the phosphorescence signal is not decreasing as the jet move downstream. This suggests that the oxygen is not able to penetrate into the jet, within the residence time of the imaged region, at least in part due to the low diffusivity within the liquid.

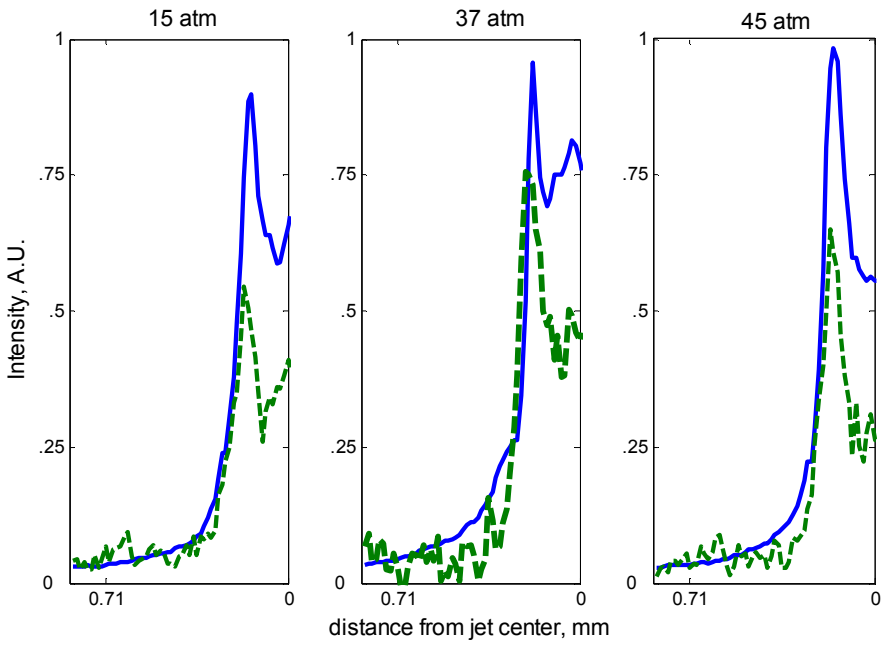

Figure 5.6: Relative fluorescence and phosphorescence for the three cases shown above. The phosphorescence intensity shows a sharp gradient in the signal and follows the fluorescence intensity very well. Location of sharp rise is the vapor/liquid interface in these subcritical jets. Solid line – Fluor. Dash line –Phos.

A test was done to determine how far the oxygen has penetrated into the jet and the minimum concentration of oxygen that will decrease the phosphorescence intensity until it is no longer detectable. Room temperature de-oxygenated liquid acetone was injected into the test chamber at room temperature pressurized with nitrogen first and air second to 4 atm. The jet diameter was approximately 300 μm, and the jet velocity was low, approximately 1 m/s, to increase the residence time of the jet within the test chamber. The phosphorescence signal for the two tests conditions are shown in Figure 5.7.

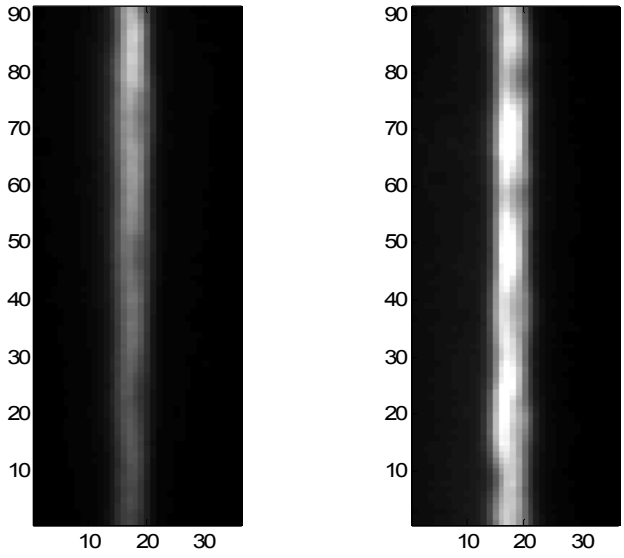

Figure 5.7: Phosphorescence intensity variation for air and nitrogen co-flow. Images of acetone phosphorescence for nitrogen (right) and air (left) co-flow taken with a 10 μs gate and 300 ns after the laser pulse at 4 atm at 2 mm downstream of the jet exit. The size of the image is 4.5 mm × 1.5 mm.

The figure shows phosphorescence images taken with a 10 μs gate 300 ns after the laser pulse. As seen in the two images, the signal from the nitrogen co-flow is higher and almost constant along the length of the stream, whereas the signal from the air co-flow is dimmer and diminishing as the stream moves downward. A point to note, the signal for both the nitrogen and air co-flow is the same at the beginning of the jet. As the temperature and pressure is the same for both case, the reduction in the intensity of the air co-flow downstream is due to the presence of oxygen in the test chamber.

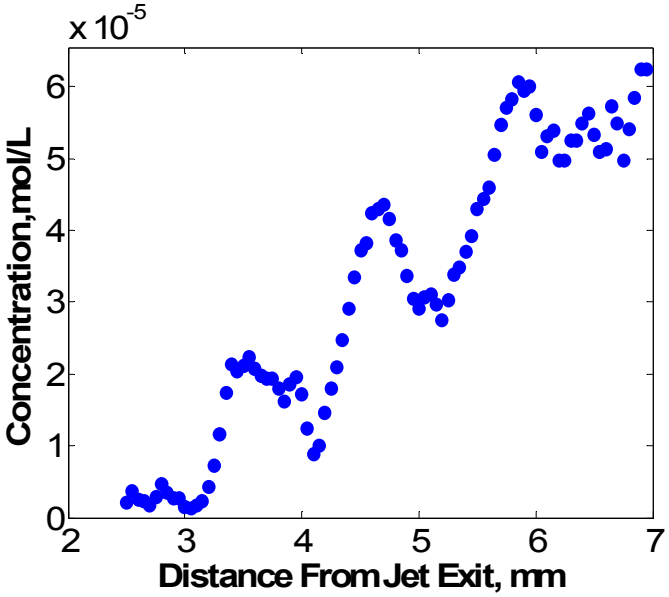

Figure 5.8: Concentration of oxygen as a function of distance downstream of the jet exit. Intensity is calculated from images taken with 10 μs gate at 4 atm pressurization.

Figure 5.8 provides the estimated concentration of oxygen as a function of the distance downstream of the jet exit. The highest concentration of oxygen seen by the acetone jet at the bottom of the jet, on average, is 6.2×10^{-5} M. At that location the approximate residence time of the jet within the test chamber is 7 ms, calculated from the velocity of the jet. This oxygen concentration will reduce the phosphorescence intensity to a third of the initial intensity. The threshold for the phosphorescence intensity signal is approximately 0.1 of the maximum phosphorescence signal seen in the image. Using the Stern-Volmer equation,[46,47] the equivalent oxygen concentration to reduce the phosphorescence intensity to 0.1 of the initial intensity is 1.05×10^{-4} M. For this test case, the laser is able to penetrate 56 μm into the jet before the laser energy is reduced by 87%, thus the oxygen will also have to penetrate the same distance. For that distance and

minimum concentration required, it will need approximately 55 ms for the phosphorescence signal to decrease to 10% of the initial intensity.

Comparing the three subcritical cases and this test case, the decrease in the phosphorescence intensity in the subcritical cases is not as noticeable, even though the distance from the jet exit is the same. This is due to the higher jet velocity, almost an order of magnitude higher than the test case, which reduces the jet's residence time therefore less time is available for the oxygen to penetrate into the jet. In the critical region, the oxygen diffusion rate into acetone is also much higher compared to the subcritical conditions. This will allow more oxygen to penetrate the jet to reach the subcritical/supercritical interface.

5.3 TRANSCRITICAL TO SUPERCRITICAL MIXING

Heated liquid acetone jets were injected into supercritical environments in order to measure the fuel/air mixing at near critical conditions. Figure 5.9 shows the fluorescence, phosphorescence, acetone density, and mixture fraction in the test chamber. The acetone jet is preheated to 475 K and pressurized to 53 atm before injecting into 550 K air at 53 atm. The phosphorescence signal intensity is high at the jet exit, but starts to decrease as the jet move downstream, until it become negligible at the bottom of the image. The fluorescence image also shows a reduction in intensity further downstream, suggesting a lower density within the area. This is due to the liquid acetone being heated further by the air as the jet moves downstream, thus decreasing the density of the jet.

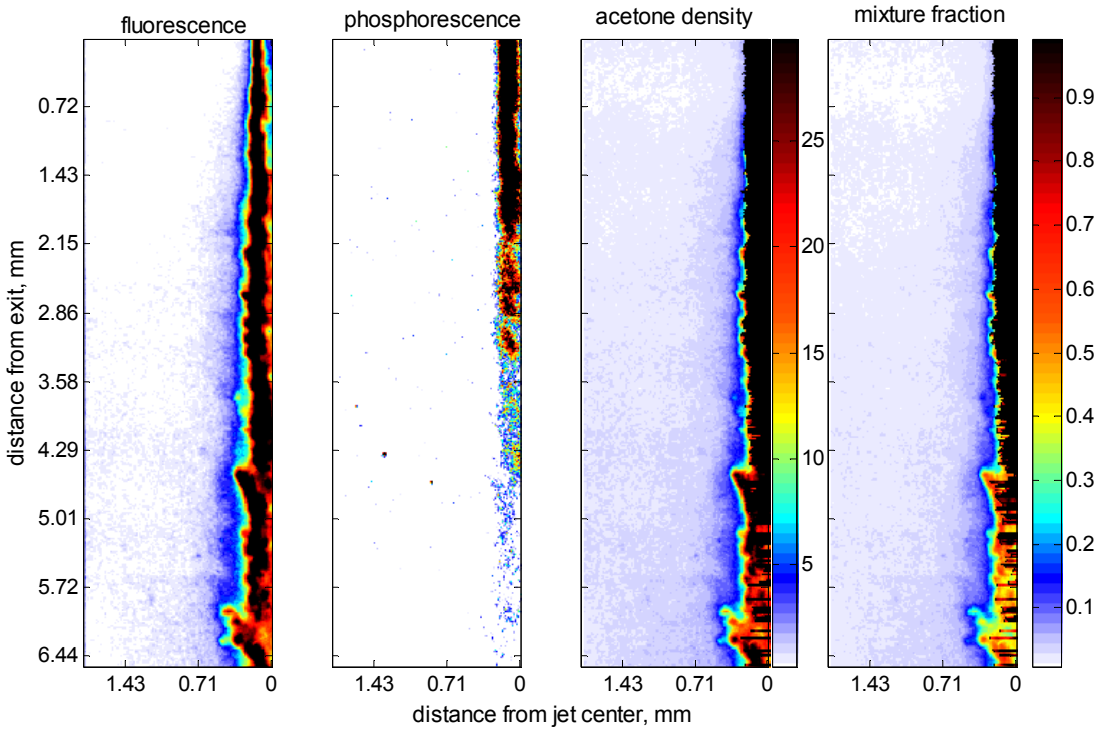

Figure 5.9: Simultaneous fluorescence, phosphorescence, and superimpose image of both of liquid acetone jet at 475 K and 53 atm injecting into 550 K air. 0 mm is at jet center. Mass flow rate – 4.98 g/s. Vjet – 8.02 m/s. Vgas ~ 1.0 m/s.

As the acetone jet is being heated, its surface tension is decreasing. This allows the oxygen to penetrate into the jet, as seen by the larger decrease in phosphorescence intensity in Figure 5.9. Since the acetone has already been preheated to 475 K before injecting, a greater fraction of the liquid jet is able to reach critical conditions. That is seen at the bottom of the image where the fluorescence and phosphorescence intensity have decreased. Another reason is due to the increase in the oxygen diffusion rate into the liquid jet at higher temperature and pressure within the system. There is also a slight increase in the jet's thickness at the region with no phosphorescence signal. From the fluorescence image at y/d=6, we see a portion the jet breaking off from the main jet in ligaments, finger-like objects, which has been described in the literatures for jets at

transcritical and supercritical conditions.[3,5] Images from the test conditions show the jet exhibiting less liquid-like properties near the bottom of the images. The jet breakup visibly looks vapor-like further downstream of the jet exit. The lensing effect was visible at the beginning of the jet, where the instabilities of the jet can be seen at the center and to the other edge of the jet. However, the instabilities are less visible from the jet center further downstream and become only visible at the edge close to the bottom.

Images for a 450 K acetone jet entering the test chamber at 59 atm, 560K is shown in Figure 5.10. There are clearly more vapor-like fluids coming off the main jet compared to the 53 am test. The liquid jet core is seen to decrease in width until it become minimal at the bottom of the image, as seen from the intensity of both the fluorescence and phosphorescence images. The phosphorescence and fluorescence intensity is not steadily decreasing in this figure, as compared to Figure 5.9. At y/d=5–6, the phosphorescence signal is negligible and the fluorescence signal low, which results from the lower transcritical density. This result in an expansion of the fluid, causing an increase of the jet waist downstream of the exit along with an increase in the spreading angle of the acetone fluid, measured to be 9.5°. Since the fluid has reached critical conditions by y/d=5, it is expected that the jet remains transcritical or reaches supercritical conditions further downstream. However, at y/d > 6, some phosphorescence signal can be seen, thus it is possible that region still retain some liquid acetone within the surrounding critical acetone.

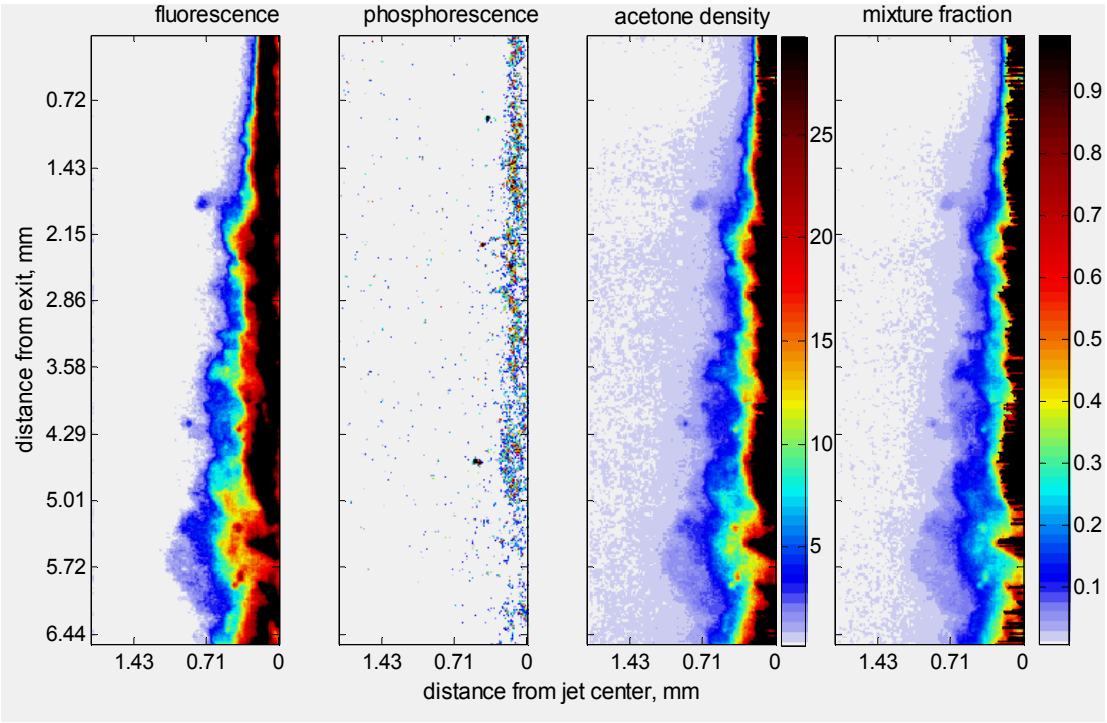

Figure 5.10: Simultaneous fluorescence, phosphorescence, and superimpose image of both of a liquid acetone jet at 440 K and 59 atm in 560 K air. 0 mm is at jet center. Mass flow rate – 4.98 g/s. Vjet – 8.02 m/s. Vgas ~ 1.0 m/s.

The next images show the acetone liquid jet preheated by another 10 K, to 450K, and injected into the test chamber, where the temperature also increased by 15 K to 575 K, as seen in Figure 5.11. The jet features are different from all the other test cases shown earlier. The jet width shows a slight increase in the first diameter length, less than 1% of the total jet width. After the first diameter length, there was a large increase in the width. The vapor spreading angle, measured from the density and mixture fraction images, is approximately 10°. The dark core spreading angle, measured from the phosphorescence image, is approximately 5.5°. These spreading angle values are comparable to the values measured by others.[3,8,63] The overall look of the jet is similar to those imaged by others at supercritical conditions.[3,4,64] The acetone density and mixture fraction images show a very high density concentration and mixture fraction within the mixing layer. The dark

core length is intact for the whole jet length seen here. However, the waist of the core is seen to decrease at y/d=5, which says that more oxygen has penetrated into the jet and more of the acetone jet is transitioning to supercritical fluid. Within one to two diameter lengths, the whole jet will likely be supercritical.

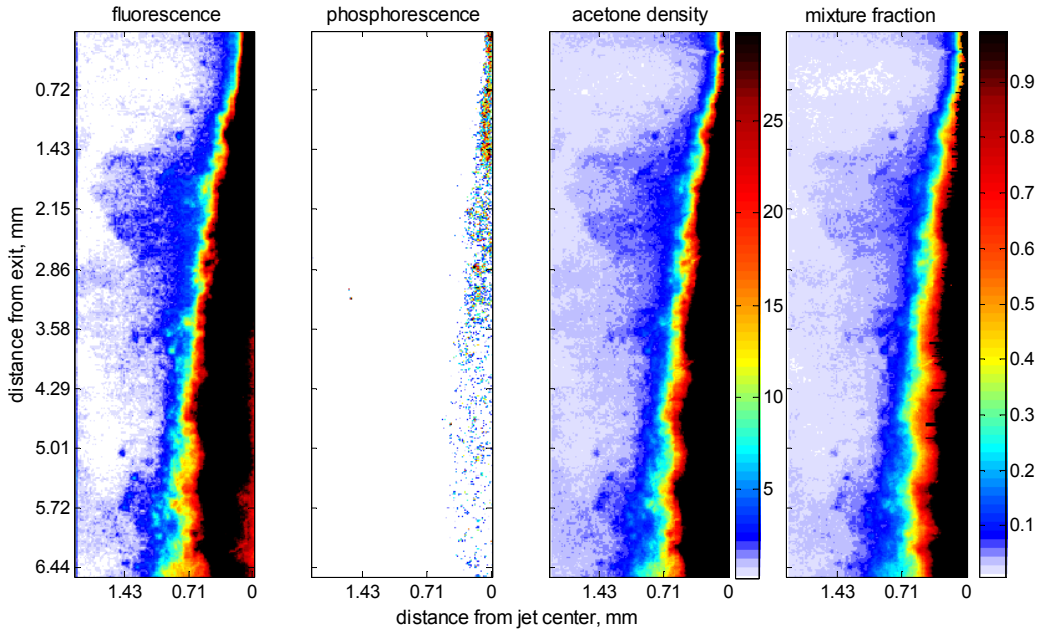

Figure 5.11: Simultaneous fluorescence, phosphorescence, and superimpose image of both of a liquid acetone jet at 450 K and 59 atm in 575 K air. 0 mm is at jet center. Mass flow rate – 8.34 g/s. Vjet – 13.45 m/s. Vgas ~ 1.0 m/s.

Another set of images from the same test case is shown in Figure 5.12. This image set is taken 330 ms after the previous image set to show the variation of the jet over time. The spreading angle and the dark core length angle are the same as the previous image set. The features of the jet are the same in the first diameter downstream of the jet exit. However, further downstream of the jet, the features are different. One, there is less phosphorescence signal at the end of the image, thus the dark core length of the jet is smaller compare to the first images set. Also, the fluorescence signal is much lower at

the bottom of the image compare to the top, which is shown be the reduction in acetone density and mixture fraction. In this image set, the acetone jet appears to have fully transitioned to a supercritical fluid, seen by the reduction in the dark core length, as compare to the previous image set, which still retain its liquid core at the bottom of the image.

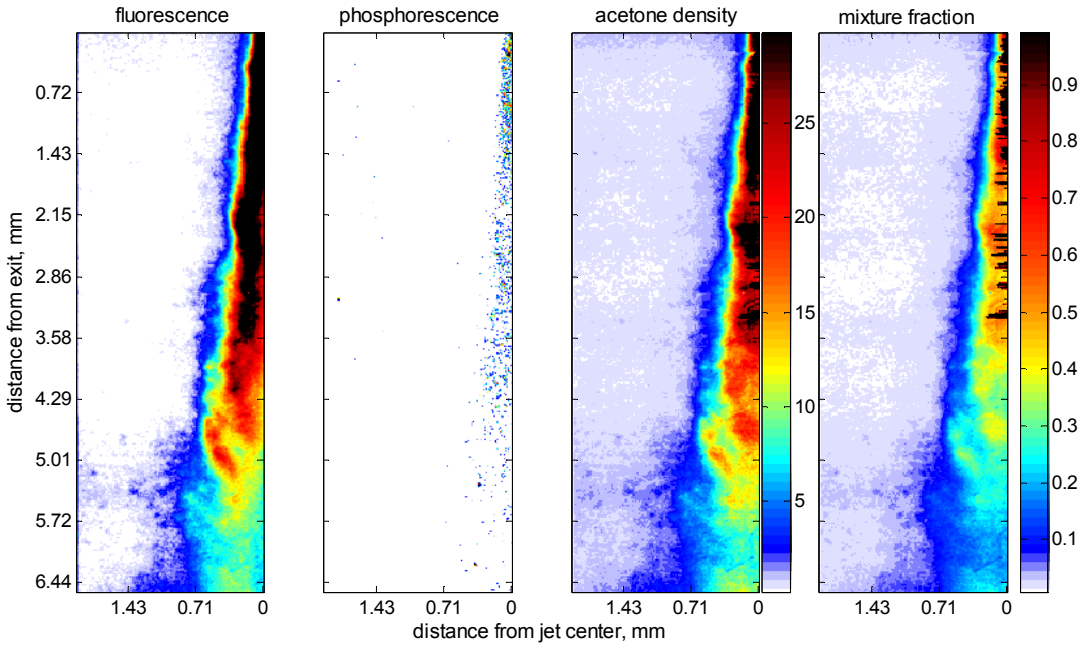

Figure 5.12: Simultaneous fluorescence, phosphorescence, and superimpose image of both of a liquid acetone jet at 450 K and 59 atm in 575 K air. 0 mm is at jet center. Mass flow rate – 8.34 g/s. Vjet – 13.45 m/s. Vgas ~ 1.0 m/s.

The uncertainty sources in these demonstrations of the PLIFP technique are mainly the fluctuations of the laser energy, the density of the mixture, and the average fluorescence yield used. The uncertainty due to the fluctuation from the laser energy is similar to the previous experiments (Chapter 4), ~5%. The uncertainty from the density of the mixture is from the calculated compressibility factor from the equation of state. The compressibility factor provide a good estimate of the density of the mixture,

however, the Peng-Robinson equation of state used does not give the most exact value, thus there is an intrinsic error associated with the compressibility factor value. In calculating the number density, an average fluorescence yield is used, and it is the value at the pressure and temperature of the test section. Depending on the temperature difference between the jet and the test section, the uncertainties would be different. The maximum temperature difference is approximately 250 K for the subcritical case. However, when the acetone vaporizes or transition to supercritical fluid, the temperature difference will be smaller. This would reduce the error in the fluorescence yield value. The approximate uncertainty in the fluorescence yield is 5-10% depending on the temperature difference. This corresponds to an overall uncertainty of 7-11%, not including the uncertainty in the density of the mixture.

Overall, the transcritical/supercritical jets have different behaviors from the subcritical jet. At and above critical, the jet behavior is similar to that of a highly dense vapor injected into a less dense vapor as described in the literature. The mixing efficiency of the critical jets are higher than the subcritical jets, as seen from the increase spread of the acetone (concentration or mixture fraction) in the test chamber instead of remaining close to the jet itself. Thus the PLIFP technique was able to capture the changes between the subcritical and supercritical jets.

Figure 5.13 shows the relative fluorescence and phosphorescence intensity for the last three cases shown above. The fourth image is from the last case but at a distance further downstream from the third image. Here the start of the phosphorescence intensity is not located on top to the fluorescence intensity, but a few pixels further in, which shows that the oxygen is diffusing into the jet. Also, the phosphorescence intensity gradient is not as

sharp as the subcritical intensity gradient. Instead of a sharp difference in oxygen concentration within the jet and the surrounding, there is a gradual decrease of oxygen concentration from the surrounding to the jet, which was predicted in Chapter 2.

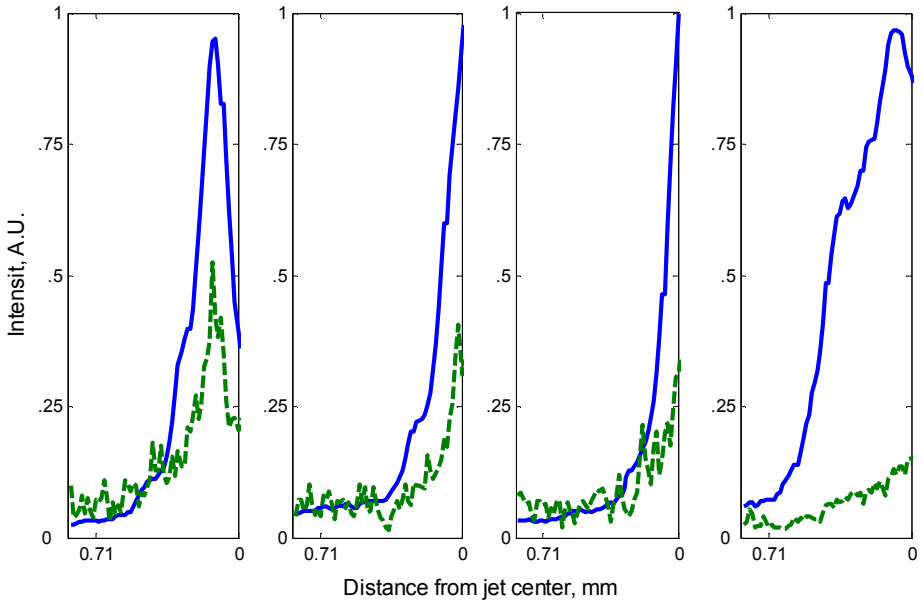

Figure 5.13: Relative fluorescence and phosphorescence for the last three images set shown. 1st image - Figure 5.10. 2nd image - Figure 5.11. 3rd and 4th image - Figure 5.12 at different distance downstream. Solid line –Fluor. Dash line – Phos.

The question now is has the oxygen penetrate far enough into the jet to reach the subcritical/supercritical interface? From Figure 2.4 the self-diffusivities of acetone can be determined at supercritical conditions. The p^+ and T^+ values are 0.076 and 1.1 for the supercritical test conditions here. This corresponds to self-diffusivities that are one order of magnitude smaller than the gas and two orders of magnitude above the liquid's. The diffusion coefficient of oxygen into acetone will be slightly higher compare to the self-diffusion coefficient since oxygen is a smaller molecule than acetone. In addition, the

acetone density is lower at supercritical conditions, thus there is a smaller density barrier that would further increase the diffusion process. Since the diffusion coefficient is closer to the vapor value than the liquid, it will have a higher probability of penetrating the jet.

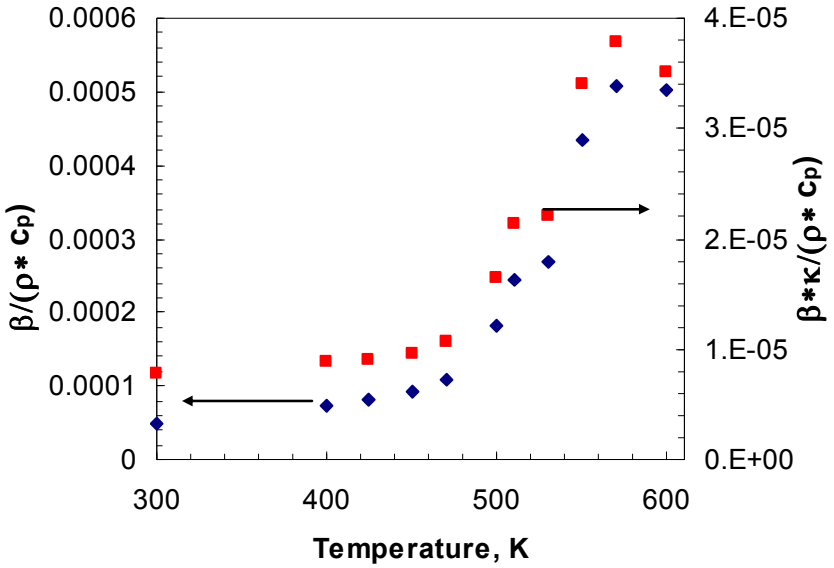

Figure 5.14: Thermal expansion rate factor for acetone at 60 atm at varying temperature.

However, the diffusion of oxygen into the jet is opposed by the motion due to thermal expansion of the acetone fluid away from the jet as the density of the jet decrease; this will push the oxygen away from the jet as well. Comparing the two rates enables us to determine which will be faster and thus whether the oxygen can reach the interface or not. The thermal expansion coefficient can be calculated from Eqn. 2.4 in an isobaric test cell at different temperatures. Using the properties of acetone at 60 atm and different temperatures, the $\frac{\beta}{\rho c_p}$ and $\frac{\beta\kappa}{\rho c_p}$ terms are calculated and shown in Figure 5.14. The increase in the thermal expansion coefficient is less than an order of magnitude from

subcritical to supercritical, thus the thermal expansion rate will also increased by less than one order of magnitude. Comparing the order of magnitude difference between the diffusion rate at subcritical to supercritical and the thermal expansion rate at subcritical to supercritical, it can be seen that the mass diffusion of oxygen into the jet vicinity will be quicker than the rate of oxygen leaving the jet vicinity due to thermal expansion. Therefore, the oxygen will be able to penetrate the acetone jet to reach the high diffusivity/low diffusivity interface.

CHAPTER 6

CONCLUSION AND RECOMMENDATION FOR FUTURE WORKS

6.1 SUMMARY AND CONCLUSION

The primary goal of this work was development of a quantitative technique for studying mixing of propellant or fuel-air mixing from subcritical to supercritical conditions. The first objective required to meet this goal was determining the photophysics of liquid and vapor acetone at various temperatures and pressures in order to extend the operating regime of acetone PLIF into the transcritical and supercritical region. Extending the technique required the measurement of certain properties of acetone, with special attention to fluorescence yield, at elevated temperatures and pressures. A series of controlled experiments were designed, and the experimental data were used to validate existing fluorescence yield models.

In addition to extending acetone fluorescence, this work also explored acetone phosphorescence as part of a procedure for delineating the interfacial region between low diffusivity and high diffusivity fluid. At subcritical conditions, this separates liquid and vapor. At elevated temperature and pressure, it can help identify the transition from subcritical to supercritical temperatures. Instead of using the difference in fluorescence intensity (due to the density change) between the two phases to discern where the interface is located, the phosphorescence signal from the "liquid" phase is used instead. The phosphorescence signal is dependent upon the concentration of oxygen within the acetone. For a liquid, the diffusion rate of oxygen into acetone is extremely low, thus the concentration will be low, increasing the phosphorescence signal. However, in the

transcritical to supercritical regime, the diffusion rate is fast, two orders of magnitude faster than in the liquid, thereby allowing more oxygen to diffuse into the liquid and at a faster rate, thus reducing the phosphorescence signal. Therefore, the location of where the phosphorescence signal starts is the location for the interface.

The vapor acetone fluorescence yield from ~300-600 K (T/T_c~0.6-1.2) and 1-60 atm (p/p_c~0.02-1.3) was measured and compared to the values predicted by the models proposed by Thurber *et al*. and Braeuer *et al*. The measured vapor fluorescence yields generally follow the predicted trends for pressures and temperatures from subcritical to supercritical values. The fluorescence yield decreases as the temperature is raised, while it increases with pressure. For a given pressure, the fluorescence yield drops nearly linearly with increasing temperature. Over the range 300-575 K, the fluorescence yield decreases by approximately 33%. The normalized fluorescence yield plateaus at 30 atm to about twice its value at 1 atm, and this behavior is essentially the same for any temperature. Thus, the temperature and pressure effect on the vapor fluorescence yield are seen to be essentially independent of each other.

This trend agrees with the model proposed by Braeuer *et al*., however the values obtained from the experiments differ from the predicted fluorescence yields. The pressure and temperature dependence calculated from the model is lower than the experimental results. On the other hand, the fluorescence yield calculated is comparable to predicted results from the Thurber model at low pressure and temperature. However, the Thurber model predicts that the temperature and pressure effects are interdependent; for a given pressure, the normalized fluorescence yield decreases with temperature, and the rate of decrease is lower as the system's pressure increases. Also, for a given temperature, the

normalized fluorescence yield increases with increasing pressure, but the dependence increases with increasing temperature. However, the differences for the temperature and pressure range considered are minimal, within a few percent. The differences between the experimental results and the two models are within 7%, depending on the temperature and pressure of the system.

Often time, the pressure within a system is known and is a constant value. Thus, the only variable that would affect the fluorescence signal is the change in temperature within the system. If the fluorescence signal per acetone molecule is considered instead of the fluorescence yield, the decrease in the signal is found to be only ±12% for a temperature range of ΔT=300 K, thus the error in the density value will be within that value. Since the change in acetone concentration can be quite large in a mixing flow, the systematic error incurred by neglecting the temperature dependence could be small compared to concentration range.

For liquid acetone, the fluorescence and phosphorescence signal were measured at various temperatures and pressures (T/T_c=0.6-0.8, p/p_c=0.02-0.6). Fluorescence and phosphorescence spectra were also measured at room temperature and pressure for two laser excitation wavelengths. The fluorescence signal was shown to be nearly invariant with pressure and temperature, at least over the range of conditions tested. The fluorescence spectrum for both excitation wavelengths was similar in range and shape with only a small variation in the peak emission wavelengths. Comparing the liquid and vapor fluorescence spectrum, the liquid spectrum is more compact while the vapor fluorescence is more evenly distributed across the spectrum.

The liquid phosphorescence yield was found to be independent of pressures but decreases exponentially with increasing temperature. The phosphorescence lifetimes were also measured and were shown to have a double exponential decay. For increasing temperature the first lifetime ranges from 1-0.5 μs and the second lifetime ranges from 7-4.5 μs for the temperature range measured, which is in agreement with the lifetime measurements. Since the phosphorescence yield, and thus the phosphorescence signal, is exponentially decaying, the decay of the signal will be lower at the higher temperature, thus the signal will be low, but still visible to the camera. The phosphorescence spectra for liquid acetone are slightly red-shifted compare to the fluorescence spectra for both excitation wavelengths. Also, the lifetime of the individual emission wavelengths were measured and it was found that the lifetimes vary with wavelengths. The lifetime was seen to increase with increasing wavelengths for both the excitation wavelengths. Thus, the spectrum will red-shift over time. However the shift between the fluorescence and phosphorescence emission spectra is not far enough to delineate the two emissions spectrally and they can only be differentiated temporally.

The total fluorescence signal and phosphorescence signal were compared to determine the phosphorescence to fluorescence ratio. For 266 nm excitation the ratio was approximately 0.035 while for 285 nm excitation the ratio was 0.08. This follows the trends seen from other investigations. In general, the existing photophysic models for acetone vapor can be used, at least qualitatively, to explain the behavior of the liquid acetone fluorescence. However to provide quantitative liquid fluorescence values, the model need to be modified to address the temperature independence of the fluorescence yield in liquid. To address the phosphorescence yield, an issue not addressed in the

current models, requires modifications to the models. Still, the current models appear to be sufficiently accurate to be useful for interpreting acetone PLIF measurements in transcritical and supercritical jet breakup and mixing studies.

The technique was then applied to mixing of an acetone (subcritical temperature) jet in both subcritical and supercritical environmental (air) conditions to demonstrate its capability to determine acetone concentration and mixture fraction within the flowfield, as well as to determine the transition or phase interface. Overall, the technique qualitatively met the expected variations in jet fluid concentration or mixture fraction as the system transitioned from subcritical to supercritical conditions. In the subcritical regime, the phosphorescence signal was able to delineate the vapor/liquid interface very well, within the blur resolution of the optics. For the transcritical and supercritical regime, the phosphorescence signal decreased significantly or was not present within the transcritical/supercritical region. This suggested that the oxygen was able to diffuse into the jet much faster compare to the subcritical regime. The possibility exists that the expansion of the supercritical fluids due to the decrease in the density will prevent the oxygen from diffusing far enough to reach the subcritical/transcritical interface A basic analysis was used to show that the diffusion of oxygen should be fast compared to the expansion of the fluid, thus the oxygen should be able to reach the interface.

The fluorescence signal from liquid acetone droplets was used to determine the mass/ size of the droplets at subcritical conditions. Though for large droplets, the phosphorescence signal can be used instead. The methods work well; however, due to the spatial resolution of the system and the increase in vapor density at higher pressure and

temperature, there is a minimum droplet size the method can discern. At lower pressure, where the saturated vapor pressure is lower, the minimum size limit will be smaller.

The acetone PLIFP technique developed here should be applicable for a wide range of conditions from sub-atmospheric pressure and below room temperature to supercritical pressure and temperatures. At room temperature, the vapor pressure of acetone is 0.2 atm, and the approximate signal-to-noise ratio (SNR) for that vapor pressure is twelve or above. However, the saturated vapor pressure decreases with decreasing temperature, which will reduce the overall concentration within the flow, thus reducing the SNR. Since the fluorescence signal is extremely short-lived, only nanoseconds long, the temporal resolution is very sharp; the flow can go at very fast rate without producing any noticeable blur in the images. Phosphorescence generally produces a lower signal than fluorescence, and will thus have a lower SNR. With the current optics, the SNR ranges from six for low temperature systems to less than two at close to critical temperature. In addition, the phosphorescence signal is longer-lived, microseconds long. Thus phosphorescence can lead to spatial blurring; for a 2 μs exposure in flow with velocities of ~100 m/s, the spatial resolution would be limited to about 200 μm. As the laser energy at the wavelength used here (266 nm) can only penetrate a small portion of a liquid jet, this technique is currently limited to flows with low overall liquid concentration and to small liquid droplets. The optimal applications for this technique are therefore sprays, the interfaces of liquid jets and vapor-vapor mixing. If the technique can be further developed so that the laser has a longer optical path length through liquid, it can then be used for applications that involve phase-changes or transitions within the jet core. In

addition, this technique has limited application to reacting flows, as the acetone will oxidize in the reaction zone of a flame.

6.2 RECOMMENDATION FOR FUTURE WORK

The technique presented in this work allows for the quantitative measurements of multiphase mixing flows at subcritical to supercritical conditions. However, there are still some issues that can be improved upon and thus require further investigation. The first, and probably most important, factor is the laser's ability to penetrate fully into the liquid rather than only a small distance into the jet. This would allow us the complete mapping of the flowfield instead of a small portion of the jet. It would provide further insight in to the transition process from liquid to supercritical and the structures of the jet at that condition. The increase in laser path length will also allow the technique to provide mass and size calculation for large droplets (e.g., diameter greater than 100 μm). This would greatly increase the versatility of the technique. The method to increase the penetration length is to go to longer excitation wavelength, $\lambda > 300$ nm, which has lower absorption cross-sections, thus less absorption of the laser energy. Before this technique can be used at longer wavelength, the photophysics of acetone at that wavelength need to be investigated, especially the liquid phase. Similarly, appropriate laser sources (with sufficient pulse energy) need to be identified.

In addition, the longer excitation wavelength has been proposed to increase the phosphorescence/fluorescence ratio, thus the phosphorescence intensity. This will increase the signal-to-noise ratio of the phosphorescence signal, thus providing a more resolved interface location. Thus a study should be done to determine the optimum

wavelength that would provide the best overall phosphorescence/fluorescence ratio and the signal-to-noise ratio for both the fluorescence and phosphorescence signal.

Also, the photophysics of liquid acetone should be studied in further detail, and possibly a model should be created to definitively determine the source of its unique photophysical characteristics. Specifically, it is interesting to determine the cause of the double exponential lifetime and the initial blue shift in the emission spectra for the phosphorescence signal. Typically, the triplet energy manifold is slightly lower in energy compared to the singlet energy manifold; thus it is expected that the triplet state will have an emission spectra that is slightly red-shifted compared to the singlet state fluorescence. However, this is based on emission from the lowest levels in the vibrational manifold. Since the initial intersystem crossing may be from excited states, the initial emission may be blue-shifted rather than red-shifted. Another interesting question is whether the fluorescence yield is in fact independent of temperature. For the temperature range considered in the current study, the results suggest that the liquid fluorescence yield is independent of temperature. For vapor acetone fluorescence, the yield decreases by 10% for the same temperature range. It is possible that the liquid change is similar, but too small to be discerned with the existing systematic experimental errors. If it is constant, the question is why - how is the fluorescence process different between liquid and vapor.

Another concern that needs to be investigated is the oxygen diffusion rate into the jet versus the mass expansion of the jet due to the decrease in density. The images from the test cases show the phosphorescence signal still present within the jet, even at high temperature. Thus the temperature is not a major contributor to the decrease in the phosphorescence signal and so the main contributor will be from the oxygen

concentration. The order of magnitude analysis done showed the oxygen diffusion rate to be faster than the mass expansion rate. However, to provide a better interface location a more detail analysis of the two rates should be done to determine how far oxygen can penetrate into the jet.

APPENDIX A

AUTOIGNITION OF ACETONE

This section examines the autoignition of acetone with a focus on determining the safety of using acetone for liquid-gas jet mixing at high pressures and temperatures. The autoignition temperature is the temperature at which a substance will ignite without an outside energy source. In addition to the autoignition temperature, there is an associated autoignition delay time, which is how long it will take for the substance to ignite at that temperature. So there is really not one autoignition temperature for a substance; whether ignition occurs depends on a time scale of importance. At high pressure, the autoignition temperature of a substance decreases for a given delay from its atmospheric value, or the autoignition delay time decreases for a given temperature. Thus one needs to be careful when operating at high pressure and temperature. This appendix deals with how acetone autoignition depends upon temperature, pressure and O_2 mole fraction of the test conditions.

The autoignition temperature of acetone in air is reported to be 738 K at atmospheric pressure in air (MSDS, Carolina Biological Supply Co.). However, others have reported an autoignition temperature of 773 K, which was found through experiments at atmospheric pressure in air for equivalence ratios from 0.95 to 8.[65] Heling *et al*. also measured the autoignition delay time of acetone for temperatures ranging from 737 K to 835 K at atmospheric pressure (see Figure A.1). Thus at high pressure, the autoignition temperature could be reduced to a value close to the test conditions of the current experiments.

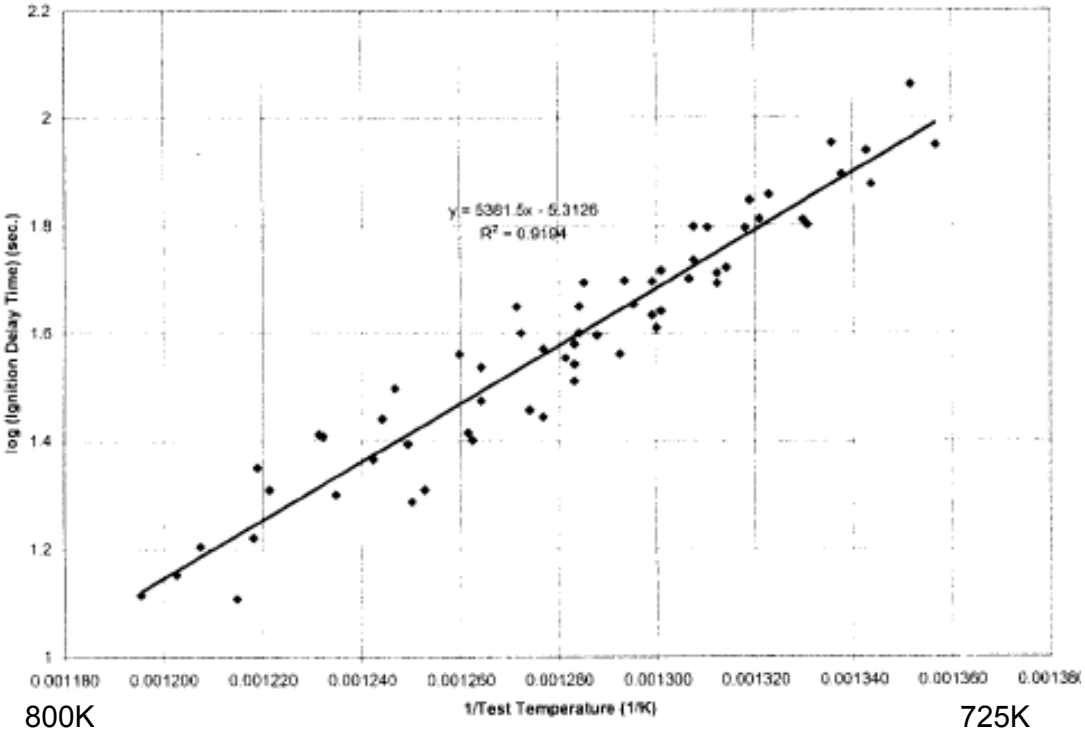

Figure A.1: Acetone (technical grade) autoignition delay time (ADT) versus inverse temperature (T^{-1}). Vertical axis is $\log_{10}$ of the ADT.[65]

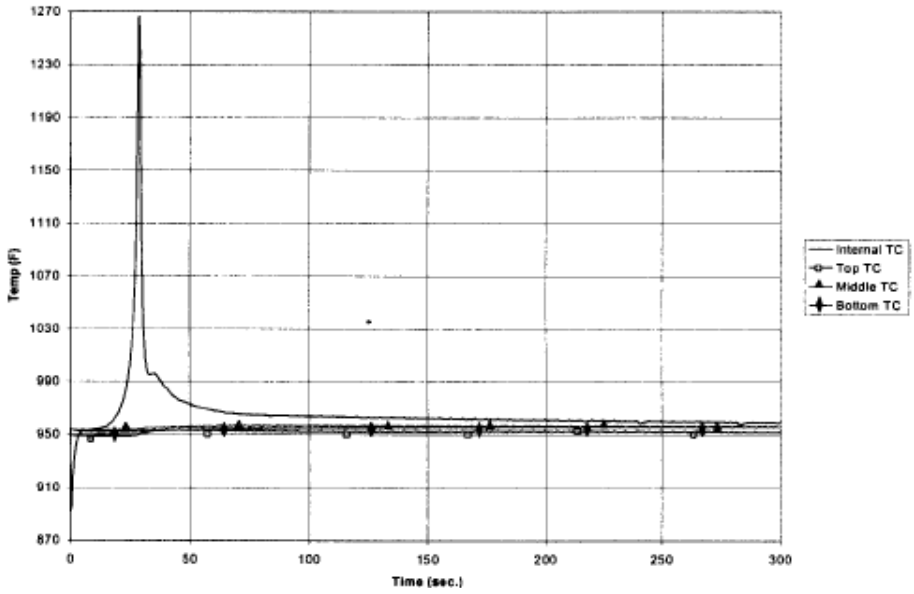

Figure A.2: Temperature profiles of an acetone test run at 785 K. Internal TC located at the center of the test apparatus. A 100 microliters of liquid acetone was injected into the test apparatus. Reheating time ~5 secs. ADT ~25 sec. [65]

In the experiments of Heling *et al.*, there was an initial drop in temperature when the room temperature acetone was injected into the system. However, the time taken for the system to return to the original temperature was approximately 5 seconds, which is negligible as it takes longer for the system to chemically react. An example of one of the test runs can be seen in Figure A.2.

A best fit line is shown on the plot and the equation for the line is given as:

$$\log_{10} ADT(\text{sec}) = 5318.5/T(K) - 5.3126 \qquad \text{Eqn. A.1}$$

Thus we can see that the autoignition delay time increases exponentially with temperature. For acetone at atmospheric pressure, the ADT is extremely long for the temperature range in this work. However, as the pressure increases from atmospheric to a much higher number, the ADT will dramatically decrease. This is due to the increase in collision rates of molecules as the pressure increases, thus increasing the chemical reaction rates as well.

The autoignition delay time dependence of acetone for varying conditions other than temperature was not found in the literature. Correlations for other ketones and alcohols were also not found. However, correlations have been determined for other molecules, and these correlations can be used to obtain an approximate ADT for the pressure and oxygen mole fractions of interest. Correlations found for temperatures at or above 1000 K were not used since the chemical kinetics in this (high) temperature range is generally different than the chemical kinetics at lower temperatures, e.g., 500-800 K. General correlations are given in the form shown in Eqn. 2,[66,67]

$$t_{ign}(\mu\sec) = A * p(atm)^m \phi^n \chi_{O_2}{}^p \exp\left(\frac{E(kJ/mol)}{RT}\right) \quad \text{Eqn. A.2}$$

where A is a constant, p is pressure in atmosphere, ϕ is equivalence ratio, χ_{O2} is mole fraction of oxygen, E is activation energy, R is the universal gas constant, and T is temperature of the system.

Therefore, for a given temperature and equivalence ratio, we can scale the ignition times for two conditions as:

$$\frac{\tau_{ign2}}{\tau_{ign1}} = \left(\frac{p_2}{p_1}\right)^m \left(\frac{x_{O_2 2}}{x_{O_2 1}}\right)^p \quad \text{Eqn. A.3}$$

In correlations for various kerosene-based fuels, the pressure dependence (exponent) ranges from m = -1.05 to -1.77.[67] The oxygen exponent has a wider range of reported values, from p = -1.0 to -2.0, depending on the temperature and composition of the fuel.[66-68] These correlations were obtained for pressures from 6.8 to 23 atm and oxygen mole fractions from 0.06-0.2. It can be seen that increasing the pressure or increasing the oxygen mole fraction would reduce the ADT.

$$\frac{\tau_{ign2}}{\tau_{ign1}} = \left(\frac{p_2}{p_1}\right)^{-1.77} \left(\frac{x_{O_2 2}}{x_{O_2 1}}\right)^{-1.0} \quad \text{Eq. 4}$$

Using the range of pressures and temperatures relevant to this work, an approximate ADT can be calculated. For one test case with a cell temperature of 560 K, liquid jet temperature of 450 K, pressure of 59 atm and 21% oxygen, a worse case scenario, (m=-1.77,) the estimated ADT is 46 seconds. If we were to run at a higher temperature of

575 K, the ADT would drop to 20 seconds, which is shorter than the run time for the experiments. Thus to prevent the autoignition of acetone within the test chamber, and still be able to work at transcritical/supercritical condition, the oxygen mole fraction would have to be reduced. The correlation can also be used to determine the maximum oxygen mole fraction that could be used in the experiment and still prevent autoignition. Using the worse case scenario (m= -1.77 and p= -1.0), and for an ADT no less than 75 seconds (3 times the test time duration) at a pressure of 59 atm, the maximum oxygen mole fraction is 0.055 for 575 K and 0.13 for 560 K. Thus, experiments operating with any oxygen mole fraction smaller than those values should be safe for test duration of 25 seconds or less. Since the worst case ranges of the exponents were used, this is a conservative estimate; we would expect a higher ADT for these test conditions.

In the case where a coaxial jet is used instead of a single jet injected into a heated test chamber, the ADT would be longer. Using a heated vapor coaxial jet surrounding the liquid jet would allow the liquid jet to be heated to supercritical conditions without heating the whole chamber. Since the heated fluids are concentrated in a small region of the test cell, the majority of the test cell volume would still cold compare to the jets. Thus close to the jet the temperature would be at critical to supercritical conditions while further away from the jet the temperature would be lower. If reactions occur, it would be limited to the local area, since it does not have the energy to sustain those reactions, and would not affect the overall test cell.

REFERENCES

[1] Oschwald, M., Smith, J., Branam, R, Hussong, J., Schik, A., Chehroudi, B., Talley, D., "Injection of Fluids into Supercritical Environments," Combustion Science and Technology, Vol. 178, No. 1-3, 2006, pp.49-100.

[2] University of Leeds, Rayner Chemistry Group/Leeds Cleaners Synthetic Group, URL:

http://www.chem.leeds.ac.uk/People/CMR/nav.html [cited 2 April 2008]

[3] Cheroudi, B., Talley, D., Coy, E., "Visual Characteristic and Initial Growth Rates of Round Cryogenic Jets at Subcritical and Supercritical Pressures," Physics of Fluids, Vol. 14, No. 2, February 2002, pp. 850-861.

[4] Mayer, W., Ivancic, B., Schik, A., Hornung, U., "Propellant Atomization and Ignition Phenomena in Liquid Oxygen-Gaseous Hydrogen Rocket Combustors," Journal of Propulsion and Power, Vol. 17, No. 4, 2001, pp. 794-799.

[5] Mayer, W., Schik, A., Schäffler, M., and Tamura, H., "Injection and Mixing Processes in High-Pressure Liquid Oxygen/Gaseous Hydrogen Rocket Combustors," Journal of Propulsion and Power, Vol. 16, No.5, 2000, pp. 823-828.

[6] Wu, P.K., Chen, T.H., Nejad, A.S., Carter, C.D., "Injection of Supercritical Ethylene in Nitrogen," Journal of Propulsion and Power, Vol. 12, No. 4, 1996, pp. 770-777.

[7] Star, A.M., Edwards, J.R., Lin, K.C., Cox-Stouffer, S., Jackson, T.A., "Numerical Simulations of Injection of Supercritical Ethylene into Nitrogen," Journal of Propulsion and Power, Vol. 22, No. 4, 2006, pp. 809-819.

[8] Chehroudi, B., Cohn, R., Talley, D., "Cryogenic Shear Layers: Experiments and Phenomenological Modeling of the Initial growth Rate under Subcritical and Supercritical Conditions," International Journal of Heat and Fluids Flow, Vol. 23, 2002, pp. 554-563.

[9] Mayer, W., Branam, R., "Characterization of Cryogenic Injection at Supercritical Pressure," Journal of Propulsion and Power, Vol 18, No. 3, May-June 2003, pp. 342-355.

[10] Zong, N., & Yang, V., "Cryogenic Fluid Injection and Mixing at Supercritical Condition," AIAA 2003-480, 41st Aerospace Science Meeting and Exhibit, Reno, NV, 6-9 January 2003

[11] Oefelein, J.C., Yang, V., "Modeling High-Pressure Mixing and Combustion Process in Liquid Rocket Engines," Journal of Propulsion and Power, Vol. 14, No. 5, 1998.

[12] Cheroudi, B., Talley, D., Coy, E., "Initial Growth Rate and Visual Characteristic of a Round Jet into Sub- to Supercritical Environment of Relevance to Rocket, Gas Turbine and Diesel Engines," AIAA 99-0206, 37th Aerospace Science Meeting, Reno, NV, 1999.

[13] Pal, S., Moser, M., Ryan, H., Foust, M., Santoro, R., "Shear Coaxial Injector Atomization Phenomena for Combustion and Non-Combusting Conditions," Atomization and Sprays, Vol. 6, 1996, pp. 227-244.

[14] Candel, S., Herding, G., Synder, R., Scouflaire, P., Rolon, C.,Vingert, L., Habiballah, M., Grisch, F., Pealat, M., Bouchardy, P., Stepowski, D., Cessou, A., Colin, P., "Experimental Investigation of Shear Coaxial Cryogenic Jet Flames," Journal of Propulsion and Power, Vol. 14, No. 5, 1998, 826-834.

[15] Ritchie, B., Seitzman, J., "Simultaneous imaging of vapor and liquid spray concentration using combined acetone fluorescence and phosphorescence," paper AIAA-2004-0384 at the 42nd AIAA Aerospace Science Meeting, Reno, NV, January 5-8, 2004.

[16] Eckbreth, A., *Laser Diagnostics for Combustion, Temperature and Species,* 2nd ed. Combustion Science and Technology Book series. Vol. 3, Gordon and Breach, NY, 1996.

[17] Polikhov, S., Segal, C., "Two Phase Flow Supercritical Mixing," paper AIAA-2006-756 at the 44th AIAA Aerospace Science Meeting, Reno, NV, January 2006.

[18] Menon, S., Seitzman, J., Shani, S., Genin, F., Tran, T., Miki, K., Segal, C., Thakur, A., "Experimental and Numerical Studies of Mixing and Combustion in Scramjet Combustors," paper AIAA 2004- 3826 at the 40th AIAA/ASME/SAE/ ASEE Joint Propulsion Conference and Exhibit, Fort Lauderdale, FL , 11-14 July 2004.

[19] McDonell, V., Samuelsen, G., "Measurement of Fuel Mixing and Transport Processes in Gas Turbine Combustion," Measurement Science and Technology, Vol. 11, 2000, pp. 870-886.

[20] Thomsen, D., Ravikrishna, R., Cooper, C., Jiang, Y., Laurendeau, N., "Concentration Measurements in a Mixing Module for Lean, Premixed, Gas-Turbine Combustors," Journal of Propulsion Power, Vol 17, No. 1, 2000, pp. 218-222.

[21] Kearney, S., Reyes, F., "Quantitative Temperature Imaging in Gas-Phase Turbulent Thermal Convection by Laser-Induced Fluorescence of Acetone," Experiments in Fluids, Vol. 34, 2003, pp. 87-97.

[22] Thurber, M., Hanson, R., "Simultaneous Imaging of Temperature and Mole Fraction Using Acetone Planar Laser-Induced Fluorescence," Experiments in Fluids, Vol. 30, 2001, pp. 93-101.

[23] Thurber, M. C. & Hanson, R. K., "Pressure and Composition Dependences of Acetone Laser-Induced Fluorescence with Excitation at 248, 266, and 308 nm," Applied Physics B: Laser and Optics, Vol 69, 1999, 229-240.

[24] Braeuer, A., Beyrau, F., Leipertz, A., " Laser-Induced Fluorescence of Ketones at Elevated Temperatures for Pressure up to 20 bars by Using a 248 nm Excitation Laser Wavelength: Experiments and Model Improvements," Applied Optics, Vol 45, No. 20, July 20, 2006, pp. 4982-4989.

[25] Clifford, T., *Fundamental of Supercritical Fluids,* Oxford University Press, Inc, New York, 1999, Chaps, 1, 2, 4.

[26] NIST, "Thermophysical Properties of Fluid Systems," URL:

http://webbook.nist.gov/chemistry/fluid/ [cited 2 April 2008].

[27] McHugh, M.A., Krukonis, V.J., *Supercritical Fluid Extraction: Principles and Practice*, 2nd Ed., Butterworth-Heinemann, Boston, MA, 1994, Chaps. 1, 2.

[28] Wilke, C.R. & Chang, P., "Correlation of Diffusion Coefficients in Dilute Solutions," Journal of the American Institute of Chemical Engineers, Vol. 1, No. 2, 1955, pp. 264-270.

[29] Borkman, R. F., Kearns, D. R., "Triplet-State Energy Transfer in Liquid Solutions, Acetone-Photosensitized *cis-trans* Isomerization of Pentene-2," Journal of the American Chemical Society, Vol. 88, No. 15, Aug. 1966, pp. 3467- 3475.

[30] McHugh, M.A., Krukonis, V.J., *Supercritical Fluid Extraction: Principles and Practice*, 2nd Ed., Butterworth-Heinemann, Boston, MA, 1994, Chaps. 1, 2.

[31] Palmer, D.A., Fernandez-Prini, R., Harvey, A.H., *Aqueous Systems at Elevated Temperatures and Pressures*, Elsevier Academic Press, London, 2004, Chaps. 1, 10.

[32] Zabaloy, M.S., Vasquez, V.R., Macedo, E.A., "Description of self-diffusion coefficients of gases, liquid and fluids at high pressure based on molecular simulation data," Fluid Phase Equilibria, Vol 242, 2006, pp. 43-56.

[33] Arias-Zugasti, M., Castillo, J.L., Garcia-Ybarra, P.L., Supercritical Vaporization: Distinguishable Fluid Regions, Physical Review E, Vol. 68, 2003, pp. 026306.1 – 026306.5

[34] Seitzman, J.M. and Hanson, R.K,, "Planar Fluorescence Imaging of Gases," *Instrumentation for Flows with Combustion*, A.M.K.P. Taylor, editor, Academic Press, London, 1993, chap 6.

[35] Lutch, R.P., "Applications of Laser-Induced Fluorescence Spectroscopy for Combustion and Plasma Diagnostics," *Laser Spectroscopy and its Application*

Radziemski, L.J., Solarz, R.W., Paisner, J.A., editors, Marcel Dekker, New York, 1987, chap 9, pp. 623-676.

[36] Seitzman, J.M., "Quantitiative Applications of Fluorescence Imaging in Combustion," PhD Dissertation, Department of Mechanical Engineering, Stanford University, Stanford, CA, 1991.

[37] Weigand, P., Meier, W., Duan, X.R., Stricker, W., Aigner, M., "Investigations of Swirl Flames in a Gas Turbine Model Combustor I. Flow field, Structures, Temperature, and Species Distributions," Combustion and Flame, Vol. 144, 2006, pp. 205-224.

[38] Lozano, A., Yip, B., Hanson, R., "Acetone: a Tracer for Concentration Measurements in Gaseous Flows by Planar Laser-Induced Fluorescence," Experiments in Fluids, Vol. 13, 1992, pp. 369-376.

[39] Koch, J., "Fuel Tracer Photophysics for Quantitative Planar Laser-Induced Fluorescence," HTGL report no. TSD-159, Stanford University, Stanford, CA, May 2005.

[40] Lozano, A., "Laser-Excited Luminescence Tracers for Planar Concentration Measurements in Gaseous Jets," HGTL report no. T-284, Stanford University, Stanford, CA, August 1992.

[41] Thurber, M.C., "Acetone Laser-Induced Fluorescence for Temperature and Multiparameter Imaging for Gaseous Flows," HTGL Topical Report TSD-120, Stanford Unviersity, Stanford, CA, March 1999.

[42] Thurber, M., Grisch, F., Kirby, B., Votsmeier, M., Hanson, R., "Measurements and Modeling of Acetone Laser-Induced Fluorescence with Implications for Temperature-Imaging Diagnostics, " Applied Optics, July 20, 1998, Vol 37, No 21, pp. 4963-4978.

[43] Schulz, C. & Sick, V., "Tracer-LIF Diagnostics: Quantitative Measurement of Fuel Concentration, Temperature and Fuel/Air Ratio in Practical Combustion Systems," *Progress in Energy and Combustion Science*, Vol 31, 2005, 75-121.

[44] Barltrop, J.A. & Coyle, J.D., "Principles of Photochemistry," John Wiley and Sons, 1978, Chichester

[45] Bortolus, P., Dellonte, S., Faucitano, A., Gratani, F., "Photostabilizing Mechanisms of Hindered-Amine Light Stabilizers: Interaction with Electronically Excited Aliphatic Carbonyls," *Macromolecules,* Vol. 19, 1986, pp. 2916-2922

[46] Donkerbroek, J. J., Elzas, J. J., Goolier, C., Frei, R. W., Velthorst, N. H., "Some Aspect of Room Temperature Phosphorescence in Liquid Solutions", *Talanta*, Vol. 28, 1981, pp. 717-723.

[47] Kuijt, J., Ariese, F., Brinkman, U. A. Th., Gooijer, C., "Room Temperature Phosphorescence in the Liquid State as a Tool in Analytical Chemistry," *Analytica Chimica Acta*, Vol. 488, 2003, pp. 135-171.

[48] Polikhov, S., Segal, C., "Two Phase Flow Supercritical Mixing," paper AIAA-2006-756 at the 44th AIAA Aerospace Science Meeting, Reno, NV, January 2006.

[49] Bryant, R.A., Donbar, J.M., Driscoll, J.F., "Acetone Laser Induced Fluorescence for Low Pressure/Low Temperature Flow Visualization," *Experiments in Fluids*, Vol. 28**,** 2000, pp. 471-476.

[50] Pischel, U. and Nau, W.M., "Switch-Over in Photochemical Reaction Mechanism from Hydrogen Abstraction to Exciplex-Induced Quenching: Interaction of Triplet-Excited versus Singlet-Excited Acetone versus Cumyloxyl Radicals with Amines," *Journal of the America Chemical Society,* Vol. 123, No. 40, October 2001, pp. 9728-9737.

[51] Lewis, R.N. and Kasha, M., "Phosphorescence and the Triplet State," *Journal of the American Chemical Society,* Vol. 66, Dec. 1944, pp. 2100-2116.

[52] Weisman, B.R., Ausman, K.D., Benedetoo, A.F., Samuels, D.A., "Kinetics and Spectra of Fullerene Triplet State," *Proceeding of the SPIE Fullerenes and Photonics IV*, edited by Kafafi, Z.H., Vol 3142, 1997, pp. 26-35.

[53] Palit, D.K., "Photophysics and Excited State Relaxation Dynamics of p-hydroxy and p-amino-substituted Benzophenones: a review," *Research on Chemical Intermediates*, Vol. 31, No. 1-3, 2005, pp. 205-225.

[54] Milewski, M., Baksalary, J., Antkowiak, P., Augustyniak, W., Binowski, M., Karolczak, J., Komar, D., Maciejewski, A., Szymanski, M., Urjasz, W., "Deactivation of the S_2 and Two Lowest Triplet States of 4H-1-Benzopyran-4-thione and its Alkyl Derivatics in Methanol Solution," *Journal of Fluorescence,* Vol. 10, No. 2, 2000, pp. 89-97.

[55] Bogan, D. J. and Lee, D.H., "Triplet-State Chemiluminescence: Acetone T1 from the Decomposition of Chemically Activated 3,3-Dimethy-4-(N,N-Dimethylamino)-1,2-Diopxetane," *The Journal of Physical Chemistry,* Vol. 95, No. 4, 1991, pp. 1533-1535.

[56] Wilkinson, F. and Dubois, J.T., "Energy-Transfer Studies by Spectrophotofluorometric Method," *The Journal of Chemical Physics,* Vol. 39, No. 2, 1963, pp. 377-383.

[57] Copeland, G.D., Ruhman, S., and Haas, Y., "Fluorescence Decay Kinetics of Acetone Vapour at Low Pressures," *Letters*, Vol. 115, No. 4,5, 1985, p. 362-368.

[58] Costela, A., Crespo, M.T., and Figuera, J.M., "Laser Photolysis of Acetone at 308 nm, " *Journal of Photochemistry,* Vol. 34, 1986, pp. 165-173.

[59] Emrich, M. and Warneck, P., "Photodissociation of Acetone in Air: Dependence on Pressure and Wavelength. Behavior of the Excited Singlet State," *Journal of Physical Chemistry A,* Vol. 104, No. 42, 2000, pp. 9436-9442.

[60] Copeland, R.A. and Crosley, D. R., "Radiative, Collisional and Dissociative Process in Triplet Acetone," *Chemical Physics Letters,* Vol. 115, No. 4,5, 1985, p. 362-268.

[61] Halpern, A.M., Ware, W.R., "Excited Singlet State Radiative and Nonradiative Transition Probabilities for Acetone, Acetone-d_6, and Hexafluoroacetone in the Gas Phase, in Solution, and in the Neat Liquid," The Journal of Chemical Physics, Vol. 54, No. 3, 1971, pp. 1271-1276.

[62] Ritchie, B.D., "Quantitative Acetone PLIF Measurements of Jet Mixing with Synthetic Jet Actuators," PhD Dissertation, Department of Aerospace Engineering, Georgia Institute of Technology, Atlanta, GA, 2006.

[63] Bellan, J., "Supercritical (and Subcritical) Fluid Behavior and Modeling: Drops, Stream, Shear and Mixing Layers, Jets and Sprays," Progress in Energy and Combustion Science, Vol. 26, 2000, pp. 329-366.

[64] Mayer, W.O.H., Schik, A.H.A., Vielle, B., Chauveau, C., Gokalp, I., Talley, D.G., Woodward, R.D., "Atomization and Breakup of Cryogenic Propellants Under High-Pressures Subcritical and Supercritical Conditions," Journal of Propulsion and Power, Vol. 14, No. 5, `998.

[65] Heling, S., Crowl, D.A., "Experimental Characterization and Prediction of Autoignition Temperature," Symposium of the Annual Loss Prevention Symposium, Vol. 36, 2002, pp 33-71.

[66] He, X., Donovan, M.T., Zigler, B.T, Palmer, T.R., Walton, S.M., Wooldridge, M.S., Atreya, A., "An experimental and modeling study of iso-octane ignition delay times under homogeneous charge compression ignition conditions," Combustion and Flame vol. 142, 2005, pp 266-275

[67] Spadaccini, L. J., "Autoignition characteristic of hydrocarbon fuels at elevated temperature and pressures," Transaction of the ASME, Journal of Engineering for Power, Jan 1977, pp 83-87

[68] Colket, M.B. III, Spadaccini, L.J., "Scramjet Fuels Autoignition Study," Journal of Propulsion and Power, Vol. 17, No. 2, 2001, pp. 315-323.